

Experimental demonstration of the fractal nature of unstable-resonator modes

PROEFSCHRIFT

ter verkrijging van
de graad van Doctor aan de Universiteit Leiden,
op gezag van de Rector Magnificus Dr. D. D. Breimer,
hoogleraar in de faculteit der Wiskunde en
Natuurwetenschappen en die der Geneeskunde,
volgens besluit van het College voor Promoties
te verdedigen op 23 November 2005,
klokke 14.15 uur

door

Javier Augusto Loaiza

geboren te Zarzal, Valle, Colombia
op 15 Oktober 1973

Promotiecommissie:

| | | |
|-------------|--------------------------|---|
| Promotor: | Prof. Dr. J. P. Woerdman | |
| Copromotor: | Dr. E. R. Eliel | |
| Referent: | Dr. S. F. Pereira | (TUDelft) |
| Leden: | Prof. Dr. G. H. C. New | (Imperial College, London) |
| | Prof. Dr. G. W. 't Hooft | (Philips Research Laboratories/Universiteit Leiden) |
| | Prof. Dr. G. Nienhuis | |
| | Prof. Dr. P. H. Kes | |

The work reported in this thesis was funded by the ‘Stichting voor Fundamenteel Onderzoek der Materie’ (FOM).

"If I had more time, I would have written you a shorter letter"

Pascal (1623-1662)

To my four mothers.

Contents

| | |
|---|-----------|
| 1. Introduction | 1 |
| 1.1. Fractals | 2 |
| 1.1.1. Scaling, self-similarity and self-affinity | 2 |
| 1.1.2. Fractal dimension | 4 |
| 1.1.3. Building blocks | 5 |
| 1.1.4. The Fourier dimension | 6 |
| 1.1.5. Physical fractals | 6 |
| 1.2. Fractals and unstable resonators | 7 |
| 1.3. Outline of the thesis | 8 |
| 2. Theoretical framework | 11 |
| 2.1. Introduction | 11 |
| 2.2. Two-mirror resonators | 12 |
| 2.2.1. What is special about an unstable resonator? | 13 |
| 2.3. The eigenmodes according to geometrical optics | 14 |
| 2.3.1. Point-source approach to the eigenmodes of unstable resonators. | 14 |
| 2.3.2. Ray-optics approach | 17 |
| 2.4. The eigenmodes according to wave optics | 21 |
| 2.5. Finding the eigenmodes: Asymptotic expansion | 25 |
| 2.5.1. Stationary phase contribution | 26 |
| 2.6. Eigenfunctions of an unstable resonator: the Virtual Source Theory | 28 |
| 2.6.1. Expansion in Virtual Sources | 29 |
| 2.6.2. Eigenmodes of unstable resonators: Fractality | 32 |
| 2.7. Conclusion | 33 |
| 3. Behold the darkness! | 35 |
| 3.1. Introduction | 35 |
| 3.2. How to isolate the fundamental mode of a cavity | 35 |
| 3.3. Estimating the parameters of the experiment | 36 |
| 3.4. In search of the ideal light source: fast modulation of a CW laser | 39 |
| 3.4.1. Electro-optical modulators as light switches | 39 |
| 3.4.2. Acousto-optical modulators as light switches | 40 |
| 3.5. Afterglow of pulsed lasers | 43 |

| | | |
|-----------|--|-----------|
| 3.5.1. | Afterglow of a sub-nanosecond passively Q-switched microchip laser | 43 |
| 3.5.2. | Afterglow of a regeneratively amplified mode-locked laser | 44 |
| 3.6. | Could a semiconductor laser diode be the solution to our problem? | 46 |
| 3.7. | Afterglow of a pulse-driven semiconductor diode laser | 48 |
| 3.7.1. | Detection by means of time-correlated single-photon counting | 49 |
| 3.7.2. | Using an ICCD camera | 50 |
| 3.8. | Conclusion | 56 |
| 4. | Towards a fractal pattern | 57 |
| 4.1. | Introduction | 57 |
| 4.2. | Experimental method | 57 |
| 4.2.1. | Experimental setup | 58 |
| 4.2.2. | Aligning the cavity | 59 |
| 4.2.3. | Evolution of the intracavity intensity profile | 60 |
| 4.3. | Formation of an asymptotic intracavity pattern | 63 |
| 4.3.1. | Influence of the blocking factor of the ICCD camera | 63 |
| 4.3.2. | Is the asymptotic state unique? | 67 |
| 4.4. | Is it a Fractal? | 70 |
| 4.4.1. | Characterizing the fractal | 70 |
| 4.4.2. | Fractal analysis of an intracavity intensity profile | 71 |
| 4.4.3. | Evolution of the fractal dimension during the last stages of the decay | 73 |
| 4.5. | Fractal dimension and the aperture's geometry: Triangular apertures | 75 |
| 4.5.1. | Improving the experiment by better mode matching: a pinhole as spatial selector | 76 |
| 4.6. | Conclusions | 78 |
| 5. | Characterization of apertured fractal images carrying noise | 79 |
| 5.1. | Introduction | 79 |
| 5.2. | The intensity profile of our model resonator | 80 |
| 5.3. | Image noise and fractal dimension | 83 |
| 5.3.1. | Shot noise and fractals | 85 |
| 5.4. | Apertured images | 88 |
| 5.5. | Conclusions | 93 |
| 6. | The fractal dimension of the fundamental mode of a plano-convex unstable resonator | 95 |
| 6.1. | Introduction | 95 |
| 6.2. | Experimental setup | 96 |
| 6.3. | 2D analysis of the intracavity intensity patterns | 97 |
| 6.4. | Experimental results | 99 |
| 6.5. | Data analysis | 100 |
| 6.5.1. | The full 2D data | 100 |
| 6.5.2. | Regional average of intensity over 1D cuts | 101 |
| 6.5.3. | Fractal dimension of individual cuts; statistics | 101 |
| 6.6. | Stability of the fractal dimension | 102 |

| | |
|---|------------|
| 6.6.1. Varying the number of exposures | 103 |
| 6.6.2. Varying the injection conditions | 104 |
| 6.6.3. Does the value of the fractal dimension converge? | 105 |
| 6.7. Conclusions | 106 |
| A. Asymptotic expansion of an unstable resonator | 109 |
| B. Approximating the eigenvalue of the fundamental mode of a wave-optics unstable-resonator. | 115 |
| C. Algorithm to determine the relative intensity of a sequence of images | 119 |
| Bibliography | 123 |
| Samenvatting | 129 |
| Curriculum vitæ | 137 |
| Nawoord | 139 |

0 Contents

Chapter 1

Introduction

If an optical engineer takes two spherical mirrors of arbitrary radius of curvature and aligns them face-to-face, the resulting optical cavity will most probably be an unstable one. An optical beam injected in such a cavity will bounce back and forth between the mirrors and, after a few such bounces, be ejected out of the cavity. Such a cavity is therefore inherently lossy, even when the mirrors have unit reflectivity. It is the lossy nature of unstable cavities that makes these resonators stand out from their stable counterparts, whose characteristics, such as mode orthogonality, a complete basis, etc. are much more widely known.

Basically all concepts associated with resonators have originally been derived for the stable case; this is hardly surprising in view of the fact that optical resonators were developed as a feedback mechanism for lasers and it seemed to be absolute imperative for the cavity to have little loss. Unstable cavities became interesting as a feedback mechanism when it was realized that they allow one to extract much more energy from an inverted medium than their stable counterparts, in essence because the optical beam completely fills the volume of the unstable cavity.

While stable resonators can be described as essentially conservative systems, unstable resonators are inherently dissipative. This causes unstable resonators to behave quite differently as compared to stable ones. For instance, while stable resonators support a complete set of orthogonal modes, the eigenmodes of unstable resonators are non-orthogonal and a complete description of an intracavity field requires the use of a set of eigenmodes and its adjoint. These sets are biorthogonal. An important consequence of this mode non-orthogonality is that the fundamental linewidth of a laser [1] built with an unstable resonator is always bigger than the equivalent laser with a stable cavity [2]. The ratio of linewidths is known as the excess-noise factor which, can be very large [3, 4].

A stable cavity's fundamental transverse mode has a Gaussian dependence [5, 6] on the transverse coordinates everywhere along the cavity's optical axis and comes nowhere close to the edges of the cavity mirrors, if the mirrors are sufficiently large. Contrarily, the fundamental mode of an unstable cavity has a very complex dependence on the transverse coordinates, with varying complexity along the cavity axis, and always spills over the edges of at least one of the cavity mirrors, no matter how large these are. Over the years various theoretical methods have been developed to describe this complex transverse field and, nowadays, a

commercial package [7] is available to calculate this field for a confocal unstable resonator. An important step was made by Karman and Woerdman [8] when they proposed, using intuitive arguments from both geometrical and wave optics, that the eigenmodes of an unstable cavity are fractals. Before elaborating on their arguments we will first introduce fractals as they are used in this thesis.

1.1. Fractals

What is a fractal? In his *magnum opus* Mandelbrot [9] proposed to define fractals as sets whose Hausdorff (fractal) dimension (D) exceeds its topological dimension¹. This is a rather abstract definition and therefore impractical and limiting when applied to the analysis of most fractal objects [9–11], including fractals that appear in nature.

In this thesis we will take a heuristic view of what a fractal is. They are objects that have, at least in part, the following characteristics (see Ref. [10]):

- A fractal has fine structure, i.e., detail on arbitrarily small scales.
- A fractal is too irregular to be described in traditional geometric language, both locally and globally.
- Fractals have some form of *self-similarity*, maybe in an approximate or statistical sense.
- Fractals have a "fractal dimension", *somehow defined*, which is greater than their topological dimension.
- In most cases a fractal can be defined in a simple way, possibly *recursively*.

The material below is intended to help the reader with some of the terminology. Many more details can be found in any of references [9, 10, 12–16], where the topic is treated in great detail, at various levels of sophistication.

1.1.1. Scaling, self-similarity and self-affinity

Self-similar fractal sets are used as the starting point of most discussions on fractality and most of the criteria used to classify an object as fractal are derived from studying their characteristics. The artwork of M.C. Escher contains some beautiful examples of self-similar fractals [17].

The concept of self-similarity is intimately connected with that of *scaling*. A scaling function $f(t)$ is a function that satisfies the *homogeneity* relation [9, 12, 18]:

$$f(\lambda t) = \lambda^\alpha f(t). \quad (1.1)$$

If $\alpha = 1$, a multiplication of the coordinate t by a factor λ results in a scaling of the coordinate f by the same factor. Functions that fulfill this condition are called *self-similar*.

¹The exact definition of the Hausdorff dimension can be found in references [9, 10]. The topological dimension is a simple concept; for a line it is 1, for a surface it is 2, for a volume it is 3.

This condition can be generalized to N -dimensional functions by requiring that all points $\mathbf{x} = (x_1, \dots, x_N)$ in the set are mapped into the same set by a relation of the form $\mathbf{x}' = (rx_1, \dots, rx_N)$, with a single scaling ratio r along *all* the coordinates¹.

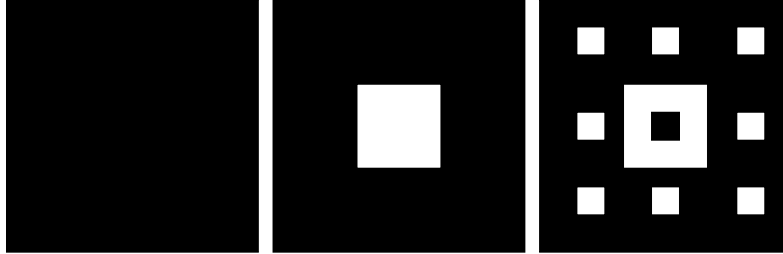


Figure 1.1: Three stages in the formation of a variant of the Sierpinski carpet.

A *deterministic self-similar fractal set* is a collage of identical copies of itself, each copy being scaled by the same factor r , ($0 < r < 1$), along all the coordinates involved. Deterministic self-similar fractals can be generated by recursively applying a simple transformation rule to an initiator, frequently a featureless pattern. Figure 1.1 shows the initial stages of this generation process, the black square at the left being the initiator and the pattern at the right the result of the first transformation. The complete transformation rule consists of twice applying the following procedure: divide each square in nine equal parts, and change the color of the small square in the center. The scaling factor is $1/9$.

A *statistically self-similar fractal set* is a collage of identical (in a statistical sense) copies of itself, each scaled by the same factor r along all directions. Figure 1.2 shows a comparison

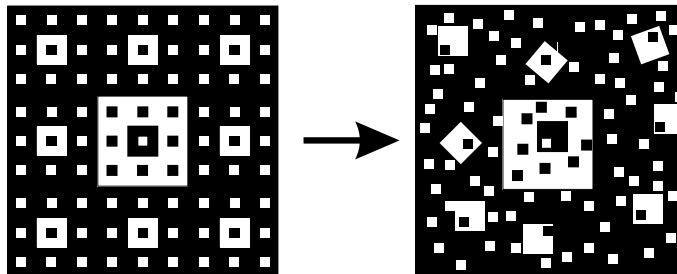


Figure 1.2: A comparison between a deterministic self-similar (at the left) and a statistically self-similar (at the right) fractal, based on the same generator.

son between deterministic and statistical self-similar fractals. The two fractals use identical building blocks, but their position and orientation are randomized in the statistical variant. Statistically self-similar sets abound in nature; typical examples are coastlines [9], porous media [12], and hydrocarbon reservoirs [19]. Self-similar fractal sets are a subset of the much broader family of *self-affine* fractals.

¹Observe that a function can be self-similar without being fractal; typical examples are the linear functions: $f(x) = mx$. They full the condition of self-similarity, but they are evidently not fractals.

When $\alpha \neq 1$ (see Eq. 1.1), the x and f coordinates scale differently. Such functions are called *self-affine*¹. In an N -dimensional space, an *affine* transformation maps a point $\mathbf{x} = (x_1, \dots, x_N)$ into a point $\mathbf{x}' = (r_1 x_1, \dots, r_N x_N)$, with r_1, \dots, r_N , being different. Accordingly, we define a *deterministic self-affine fractal set* as a collage of identical copies of itself, each copy scaled by a set of scaling factors r_1, \dots, r_N in each of the relevant directions. One can define a *statistically self-affine fractal set* in an analogous fashion.

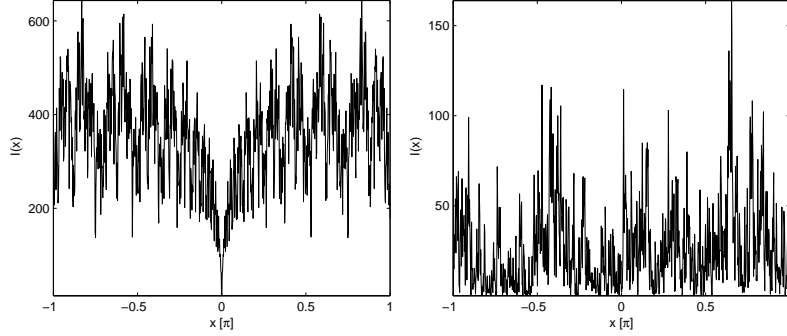


Figure 1.3: An example of a deterministic and a statistical self-affine fractal, calculated from the Mandelbrot-Weierstrass function for $\gamma = \sqrt{2}, D = 2$. At left, $\phi_n = 0$ for all n ; at right ϕ_n is a uniform random variable.

One well-known example of a self-affine fractal is the Mandelbrot-Weierstrass function [9, 10, 12, 20]:

$$W(x) = \sum_{n=-\infty}^{\infty} \frac{[1 - e^{i\gamma^n x}] e^{i\phi_n}}{\gamma^{(2-D)n}}, \quad (1.2)$$

with $1 < D < 2$ and $\gamma > 1$. The choice of the phase ϕ_n determines whether the ensuing fractal is deterministic or statistical. Figure 1.3 shows two realizations of the Mandelbrot-Weierstrass function; for the function at the left the values of ϕ_n are constant, resulting in a deterministic self-affine fractal. In contrast, the random character of the phases of the figure on the right-hand side yields a statistical self-affine fractal. Examples of "natural" deterministic self-affine fractal can be found in music², while statistical self-affine fractals can be associated with noise [21, 22].

1.1.2. Fractal dimension

A fundamental concept that will appear again and again in this thesis is the *fractal dimension*. This is just a number that quantifies how irregular a fractal F is. Its value is obtained after measuring the size of the set F at different scales δ . For each scale, we find an appropriate building block $b(\delta)$ and determine the "size" of the set F by counting the number $M_\delta^b(F)$ of building blocks that are necessary to completely cover F . For a fractal this number

¹The power functions, $f(x) = ax^n, n \neq 1$ are examples of self-affine functions.

²Fugue No. 16, G Minor, Well-Tempered Clavier Book 1. Johann Sebastian Bach. See also <http://jan.ucc.nau.edu/~tas3/wtc/i16s.pdf>

will rapidly increase when the size of the building block is reduced. If F is a fractal, $M_\delta^b(F)$ follows a power law:

$$M_\delta^b(F) \approx c\delta^{-s}, \quad (1.3)$$

and the dimension s_b of the fractal set F is given by [9, 10, 12]:

$$s_b = \lim_{\delta \rightarrow 0} \frac{\log M_\delta^b(F)}{-\log \delta}. \quad (1.4)$$

The dimension of the fractal object F can thus be determined by evaluating the slope, in a log-log plot, of the curve describing the size of the data set as a function of the scale at which the data are measured.

When we know the generation rule and the initiator of a deterministic self-similar fractal we can follow a simple procedure to obtain the fractal dimension. For instance, we note that for the fractal set of Fig. 1.1, only 65 squares are black after zooming in by a factor of 9, onto a square that appears entirely black at the original scale. Therefore, the dimension of this fractal is:

$$D_{\text{similarity}} = \frac{\log 65}{-\log 1/9} = 1.899. \quad (1.5)$$

One of the advantages of this similarity dimension ($D_{\text{similarity}}$), is that its value does not depend on the specific shape of the figures used to build the fractal; instead it follows from the scaling properties of the generation rule. However, most of the fractals do not have a simple generation rule, or at least not one that we know. Therefore the similarity dimension is used only in the context of pure mathematics.

When we do not know the generation rule of the fractal under study, our only option is to measure the set F , using building blocks of a specific shape. This has as a drawback that the value of the fractal dimension obtained in this way may depend on the nature of the building block b to cover the set F [9, 10]. This may sound strange but is an essential characteristic of most fractal objects, as we will see. This property lies at the heart of some of the difficulties encountered when characterizing a physical fractal.

1.1.3. Building blocks

The type of building block to be used depends on the object under study. For instance, for a geometric object we will intuitively choose the elementary geometric figures as building blocks: we use line segments to measure perimeters, squares to measure areas, cubes to measure volumes. The fractal dimension that results of measuring a fractal by covering it with such figures is called the box-dimension D_{box} . The associated measuring method is known as the box-counting method. A box-counting estimation of the dimension of both fractals shown in Fig. 1.2 yields $D_{\text{box}} \approx 1.9$.

Note that the specific value of the fractal dimension obtained by the box-counting method may depend on the way that the boxes are arranged to cover the fractal F . Usually, when authors say that they use the box-counting method to estimate the dimension of a fractal set, they mean that the boxes were arranged on a uniform grid. By allowing different arrangement of the boxes, i.e., not on a uniform grid, alternative fractal dimensions based on the box-counting method can be found [9], such as the *lower entropy dimension* and the *upper entropy*

dimension. As the reader may note, in the world of fractals there are many ways to do nominally the same thing.

From a mathematical perspective, self-affine fractals are more challenging than their self-similar counterparts because it is not possible to define a general, i.e. building-block independent, fractal dimension for self-affine fractals [10]. For instance, it has not been proven that the parameter D in the definition of the Mandelbrot-Weierstrass function (Eq. (1.2)) is equal to the Hausdorff dimension of that fractal, although this has been suspected for a long time. However, it has been established that D equals the box-dimension of that function [10].

For a mathematician this is not truly satisfying but we, as physicists, can live with that. Our task, in fact, is to find a good building block to enable us to calculate the fractal dimension of the self-affine function that we will study and to be consistent in its use. In this thesis we will make use of a particular property of self-affine functions:

1.1.4. The Fourier dimension

We refer here to the fact that the power spectrum of a self-affine fractal always follows a power law [10]:

$$P(k) \propto \frac{c}{k^\beta}. \quad (1.6)$$

This allows to introduce the so called Fourier fractal dimension (D_F) which is directly related to the parameter β by the relation [10, 16, 20],

$$\beta = 5 - 2D_F. \quad (1.7)$$

It is known that the Fourier fractal dimension of a data set provides an upper bound to the box dimension of the same set [10, 16].

An important property of the Fourier dimension is that it can be very easily evaluated. We simply construct a log-log graph of the power spectrum of the data set, which immediately yields the value of β , and thus of D_F . Important is also that the Fourier method is known to be quite robust against the influence of noise [16, 23, 24].

In practice, all kinds of difficulties arise and these will be extensively discussed in this thesis.

1.1.5. Physical fractals

So far we have given examples of fractals that come from the world of mathematics. Before embarking on a discussion about the fractal nature of unstable resonator modes, it is useful to acquaint the reader with what may be a physical fractal.

Figure 1.4 shows a self-similar geometric pattern derived from a physical model worked out in detail in chapter 2. At the largest scale we see a complex mosaic whose basic motif consists of squares inside squares. The basic characteristics of this mosaic appear again and again, independently of the magnification at which we look and therefore it is a self-similar fractal. This is, however, not an endless process; at the smallest spatial scale shown the motif starts to break down and signs of pixellation appear. This is a key characteristic of a physical fractal; they exist within a limited range.

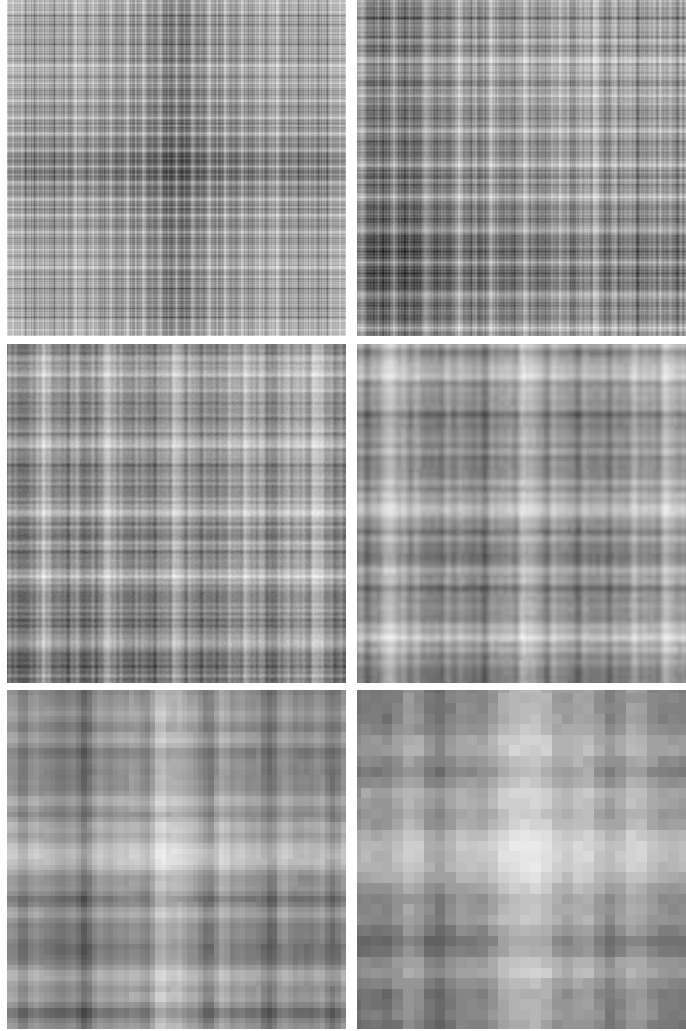


Figure 1.4: *A physical fractal seen at different magnifications. In the directions that you read: the complete pattern, a $2\times$ view, a $4\times$ view, a $8\times$ view, a $16\times$ view, and a $32\times$ view.*

1.2. Fractals and unstable resonators

Now we come back to our main point: the eigenmodes of unstable resonators are fractal. Karman and Woerdman [8, 25] argued as follows: on the one hand, a mode of a resonator is, by definition, a field configuration that is invariant under round-trip propagation, except for a factor corresponding to the round-trip effect upon overall amplitude and phase. On the other hand, unstable resonators are basically folded telescopes, and are therefore magnifying

(see Ch.2, Fig2.3). In each round trip, the magnification linearly maps the field configuration at a particular intracavity resonator plane into a bigger/smaller copy of itself. The only way in which the modes can reconcile the requirements of invariance under round-trip propagation and invariance under magnification, is by being fractals, more precisely, deterministic self-similar fractals. This argument is beautiful and compelling in its simplicity, and was immediately accepted. However by itself it is not sufficient to predict the value of the fractal dimension of the mode.

Starting from Virtual Source Theory [26,27] (see chapter 2 for details) Karman *et al* [25] numerically calculated low-order mode profiles for a one-dimensional resonator configuration (i.e. strip-like resonators). These profiles, if fractal, are self-affine. Using the box-counting method, they showed that these intensity distributions are indeed fractal, and have a box-dimension around 1.6. This numerical work was extended to include the Fourier dimension [28].

This work was put on a firm theoretical basis by Berry and collaborators [29]. Using hitherto unnoticed features of Virtual Source Theory they were able to predict that the Fourier dimension of the fundamental mode of a one-dimensional confocal resonators has a value of 2, the maximum allowed value. Moreover, Berry [30] extended this theory to bi-dimensional confocal resonators containing polygonal and circular apertures, obtaining $D_F = 3$, and $D_F = 2.5$, respectively. Berry [30] also showed that Virtual Source Theory has an underlying connection with the Mandelbrot-Weierstrass function. Therefore all eigenmodes of an unstable resonator must be fractal, as first noticed by Yates and New [31]. The latter authors showed also that there exist a simple relation between the eigenvalues of these modes, and their Fourier fractal dimension.

1.3. Outline of the thesis

The aim of this thesis is to experimentally demonstrate the fractal nature of the modes of an unstable resonator and to extract the Fourier fractal dimension of the fundamental mode.

Chapter 2 provides a summary of the necessary ingredients of unstable-resonator theory. It covers that theory from the very foundations of the geometric-optics description to the predictions based on Virtual Source Theory. The version of Virtual Source Theory presented here is based on the formulations by Southwell [26,27] and Horwitz [32]. We preferred to re-develop that theory from scratch, in order to perform calculations for *non*-confocal resonators as used in our experiments. We show that the eigenmodes of an unstable resonator are fractal both in the geometric-optics limit and as a wave-optics phenomenon.

Chapter 3 describes our search for a convenient experimental technique: cavity ring-down in combination with near-field imaging. We will estimate the main parameters that determine the experimental limitations of our approach, given the current technology. According to these estimates, the most critical component of the setup is the light source. It must be capable of an almost perfect switch-off within very few nanoseconds. The chapter describes our search for such a light source. Our solution is a negatively-biased pulse-driven diode laser.

Chapter 4 describes in detail what happens during a typical run of the experiment, using an unstable resonator containing an intracavity polygonal aperture. The ring down of the in-

tracavity intensity distribution is followed in detail, and we demonstrate that, within certain limits, the asymptotic intensity distribution can be considered stable and independent of the initial conditions. We also discuss the appearance of an unexpected blob-like feature, and conclude that it originates from the imperfect shuttering of our camera. The feature appears because we typically accumulate hundreds of thousands of images on the camera. This structure will remain with us in all the experiments, but we will learn how to deal with it. In the latter part of chapter 4 we describe our technique, based on the Fourier method, to characterize the fractal nature of the experimental intensity pattern. At this stage we will use 1D techniques to analyze 2D patterns that certainly look self-similar. Our analysis in this chapter suggests that the Fourier fractal dimension of the 2D intensity distribution has a value of order 3, in agreement with theory, but the quality of the data and/or the analysis is insufficient, to say so with confidence.

In order to improve upon this situation we have performed numerical studies of the influence of two important experimental issues on the value of the Fourier fractal dimension; this is reported in Ch.5. We conclude that it is completely wrong to include an edge, and the area beyond that edge, when using the Fourier method. This, therefore, invalidates the results of chapter 4. In chapter 5 we also evaluate, using simulations, the degree to which shot noise affects the results of a typical, ideal experiment. We obtain encouraging results by finding that a signal-to-noise ratio of 12 is sufficient to obtain a reliable estimate of the fractal dimension.

In chapter 6, finally, all that we have learned is applied to a new experiment. The results show very good agreement with theory, independence with respect to the initial conditions and of the noise level. The Fourier fractal dimension of the fundamental modes of an unstable resonator with a square aperture is found to be 2.95 ± 0.1 .

1 Introduction

Chapter 2

Theoretical framework

2.1. Introduction

In the present chapter we will describe the main features of the theory of eigenmodes of a two-mirror unstable resonator. In 1965 the development of this theory was initiated by Siegman with an *ad-hoc* geometric-optics approach, summarized in Section 2.3.1. Subsequently, Kahn developed a ray-optical treatment, using the *ABCD*-matrix formalism, which, in a modern framework, appears in Section 2.3.2. Around the same time, various attempts were made to develop a wave-optical theory for the modes of such a cavity but these proved unsuccessful. A breakthrough was reached by Horwitz [32] when he developed the asymptotic theory of unstable resonator modes, applicable in the limit of large Fresnel number. Horwitz's work put the spotlight on the complexity of these modes; his work has inspired most of the wave-optical content of this chapter. The next major step in the understanding of unstable-resonator modes was the development of virtual-source theory by Southwell [26, 27], reviewed in section 2.6.1. This theory made it possible to calculate the eigenmodes of an unstable resonator in a rather straightforward manner. In 1998 Karman and Woerdman [8] postulated that these eigenmodes should have a fractal structure; this was corroborated by applying fractal analysis to the eigenmodes of such a resonator as calculated by the virtual-source theory. Karman and Woerdman's postulate was put on a firm theoretical basis by Berry and colleagues [29, 30]; the latter also came up with a value for the fractal dimension for various cavity configurations.

In the present chapter we will expand on the work by Horwitz, making use of some parts of Virtual Source Theory, to show that the works by Horwitz and Southwell naturally leads to the conclusion that the eigenmodes of an unstable resonator are fractal. This path was chosen not only because the work by Berry relies heavily on relations that are valid exclusively on an specific family of unstable resonators, but also because the treatment by Horwitz/Southwell provides directly the eigenmode structure of *all* the modes of the resonator under study, whereas the work by Berry is restricted to the fundamental one.

2.2. Two-mirror resonators

The experiments that will be described in this thesis have been performed on two-mirror unstable cavities; in our theoretical description we will therefore concentrate on this configuration. In two-mirror cavities it is common practice to quantify the geometrical characteristic of the mirrors by means of their normalized curvatures g_i [5, 6]:

$$g_i \equiv 1 - \frac{L}{R_i}, \quad (2.1)$$

where R_i is the radius of curvature of mirror i , and L is the length of the cavity. We follow the convention of Siegman [5], namely, that the radii of curvature are positive for concave mirrors and negative for convex ones.

A standard textbook analysis [5, 6] shows that a two-mirror resonator can support ray families that never leave its volume; this requires that the product of the normalized curvatures,

$$|g_1 g_2| = G, \quad (2.2)$$

is smaller than one. Resonators that satisfy this condition are *stable*; they lie inside the gray area in the mode chart (Fig. 2.1). The mode chart also shows three types of stable resonator: The hemispheric (concentric) resonator, the confocal resonator, and the planar resonator.

When G is larger than one the resonator is *unstable* [5, 33], and is not able to support confined trajectories; eventually, all rays escape from the cavity. The unstable resonators lie in the white area of the mode chart shown in Fig. 2.1. In that figure we also show sketches of some important unstable resonator configurations. They are:

- Symmetric bi-concave resonators, indicated by A. These resonators are obtained when identical concave mirrors are separated by a distance L that is larger than the sum of the focal lengths of the mirrors. When the distance between the mirrors is reduced the losses of these resonators become smaller, until the region of stability is reached. The limiting stable configuration is the concentric (spherical) resonator configuration, a symmetric resonator where the centers of curvature of both mirrors coincide.
- Symmetric bi-convex resonators, labeled as B. In such a resonator two identical convex mirrors face each other. For a given resonator length L , the losses of the resonator are reduced as the radii of curvature of the mirrors increase. The region of stability is reached when the mirrors become flat.
- Plano-convex resonators, with label C. This configuration is obtained by replacing one of the mirrors of the bi-convex configuration by a flat mirror. The losses of a plano-convex resonator of length L are equal to those of a symmetric bi-convex cavity of length $2L$.
- Confocal negative branch resonators, indicated by D. In this family two concave mirrors of different focal length are separated by a distance L equal to the sum of their focal lengths. These resonators have the property of producing a collimated output beam when they are used in lasers, just as the related confocal positive branch resonators.

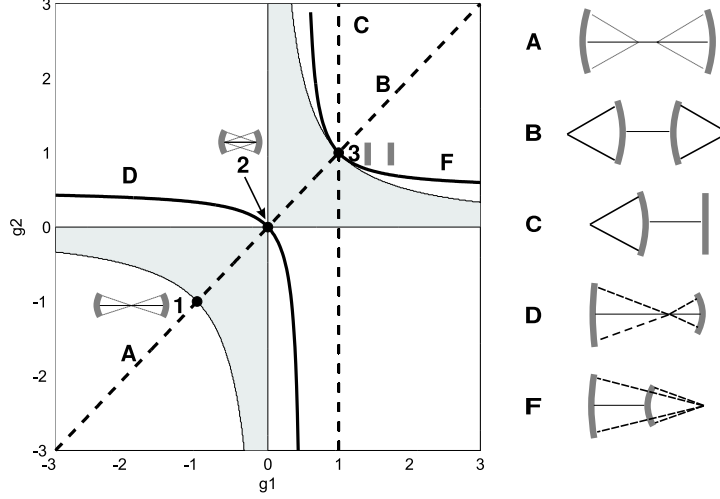


Figure 2.1: The mode chart that is used to classify the stability of two-mirror resonators. All stable resonators lie inside the gray area, Some symmetric configurations are labeled by numbers: **1**- hemispherical resonator, **2**- confocal resonator, **3**- plane resonator. All configurations inside the white area are unstable. The line segments show some special families of the latter: segment **A** (from $(-\infty, -\infty)$ to point **1**), symmetric bi-concave resonator; segment **B** (from point **3** to (∞, ∞)) symmetric bi-convex resonator; segment **C** (from point **3** to $(1, \infty)$) plano-convex resonator; curve **D** Confocal negative branch resonator; curve **F** confocal positive branch resonators.

- Confocal positive branch resonators (configuration F). This important family corresponds to a configuration where a concave and a convex mirror are separated by a distance L equal to the difference of their focal lengths. Most of the unstable-resonator literature refers to this family. The interest in this type of resonator arises because it gives rise to a collimated output beam, but the resonators do not have an internal focal point, in contrast to their negative-branch counterparts; consequently they are specially suited for high-power laser applications.

Clearly, there are many ways to put an unstable resonator together. In the following sections I will describe methods for finding the eigenmodes of these resonators, using various approximations.

2.2.1. What is special about an unstable resonator?

An unstable resonator is a cavity that supports *divergent* eigenmodes. Every round trip a significant fraction of the energy stored in the cavity leaves it; hence an unstable resonator dissipates most of its energy in just a few round trips. This has deep implications for the physics of the resonator because it implies that the evolution of a beam, or wavefront, through an unstable resonator, is not reversible [34]. Consequently, the evolution operator of the system

is no longer Hermitean [35–37]. In other words, the round-trip operator $\hat{\mathbb{T}}$ that describes the transformation of a wavefront as it travels through the unstable resonator is not equal to its adjoint $\hat{\mathbb{T}}^\dagger$ [38, 39]. This implies that the set $f_n(\mathbf{x})$ of eigenfunctions of the evolution operator $\hat{\mathbb{T}}$ differs from the set $b_n(\mathbf{x})$ associated with the adjoint operator $\hat{\mathbb{T}}^\dagger$. Their eigenvalues are, however, complex conjugated:

$$\begin{aligned}\hat{\mathbb{T}}f_n(\mathbf{x}) &= \gamma_n f_n(\mathbf{x}), \\ \hat{\mathbb{T}}^\dagger b_n(\mathbf{x}) &= \gamma_n^* b_n(\mathbf{x}),\end{aligned}\tag{2.3}$$

where \mathbf{x} represents all the relevant coordinates.

As a consequence of the non-Hermiticity of the evolution operator, the eigenfunctions $f_n(\mathbf{x})$ are not mutually orthogonal as for Hermitean systems [35–37, 40]. Hence, the coupling matrix \mathbf{M} , defined by:

$$M_{nm} = \int f_n^*(\mathbf{x}) f_m(\mathbf{x}) d\mathbf{x},\tag{2.4}$$

is not exclusively composed of diagonal elements [39]. The same kind of result is obtained with the matrix \mathbf{K} of inner products between eigenfunctions of the adjoint operator:

$$K_{nm} = \int_d b_n^*(\mathbf{x}) b_m(\mathbf{x}) d\mathbf{x}.\tag{2.5}$$

Non-hermiticity implies that the eigenmodes and the adjoint modes of such a system are *bi-orthogonal* to each-other [5, 38]; the set of modes $f_n(\mathbf{x})$ is orthogonal to the set $b_n(\mathbf{x})$:

$$\int_d b_n^*(\mathbf{x}) f_m(\mathbf{x}) d\mathbf{x} = \delta_{nm}.\tag{2.6}$$

2.3. The eigenmodes according to geometrical optics

Geometric optics provides a useful starting point for the analysis of the modes of any optical resonator because it yields valuable insight into their zeroth-order behavior. The reason is that geometric optics offers an excellent description of the propagation of light in the limit of very small wavelengths [41, 42]. Moreover, the wave-optics description of resonator theory borrows heavily from the methods developed in the geometrical-optics approach [5]. It is worth mentioning that, while diffraction by the mirror edges plays a minor role in the wave-optical description of stable resonators and therefore often can be treated like a perturbation [5], this is not true in the case of unstable resonators. In that case, the divergent nature of the eigenmodes implies that interaction with any intracavity aperture or edge, for instance that of a mirror, is not only non-negligible, but in fact fundamental for the formation of the eigenmode.

2.3.1. Point-source approach to the eigenmodes of unstable resonators.

We start by discussing the construction introduced *ad-hoc* by Siegman [33] in the article that got the field of unstable resonators started. Figure 2.2 shows a bi-convex unstable resonator and a geometric-optics representation of its fundamental mode, consisting of two

spherical wavefronts, indicated by long and short dashes, traveling in opposite directions. Each wavefront has a center of curvature P_i , whose position depends on the radius of curvature of both mirrors (Eq. (2.8)). The positions of the points P_i define the "mode" and it is our task to find them. We require a self-consistent solution, i.e., the virtual radii of curvature of the wavefronts are such that the point P_1 is the image of P_2 , and vice versa.

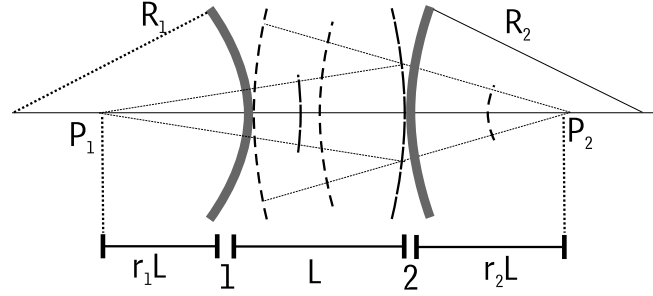


Figure 2.2: In the geometric-optics description of the eigenmodes of an unstable resonator the two point sources P_1 and P_2 are virtual images of each other upon reflection on the mirrors 1 and 2. The long-dashed and short-dashed curved lines indicate the wavefronts associated with the rays pointing to the right and left, respectively.

The locations of the points P_1 and P_2 can be derived from basic geometrical optics by writing (see Fig. 2.2):

$$\begin{aligned} \frac{1}{r_1} - \frac{1}{r_2 + 1} &= -\frac{2L}{R_1} = 2(g_1 - 1) \\ \frac{1}{r_2} - \frac{1}{r_1 + 1} &= -\frac{2L}{R_2} = 2(g_2 - 1), \end{aligned} \quad (2.7)$$

where R_i is negative for convex mirrors. The solution of the pair of equations is given by:

$$\begin{aligned} r_1 &= \frac{\sqrt{1 - (g_1 g_2)^{-1}} - 1 + g_1^{-1}}{2 - g_1^{-1} - g_2^{-1}}, \\ r_2 &= \frac{\sqrt{1 - (g_1 g_2)^{-1}} - 1 + g_2^{-1}}{2 - g_1^{-1} - g_2^{-1}}. \end{aligned} \quad (2.8)$$

Since there are no assumptions about the radii of curvature of the two mirrors this result applies to all unstable resonators, i.e., also to negative branch resonators with concave mirrors. Now that we know the essential character of the geometric-optics eigenmode, it is our task to calculate its loss per round-trip.

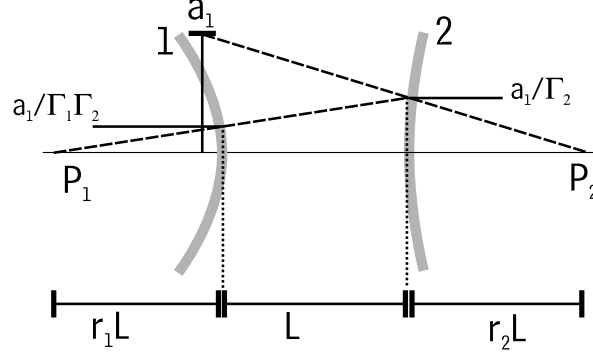


Figure 2.3: Transverse scaling of the fundamental mode of an unstable resonator during a round trip.

Figure 2.3 shows that the lateral mode size on mirror 1 is larger than that on mirror 2 by a factor

$$\Gamma_2 = \frac{r_2 + 1}{r_2}. \quad (2.9)$$

Similarly, the transverse mode size on mirror 2 is larger than that on mirror 1 by a factor $\Gamma_1 = (r_1 + 1)/r_1$. Consequently, after a single round trip the lateral mode size has increased by a factor [33]:

$$\Gamma = \Gamma_1 \Gamma_2 = \pm \frac{(r_1 + 1)(r_2 + 1)}{r_1 r_2}, \quad (2.10)$$

where the $(-)$ sign applies to the case of a negative branch resonator.

Therefore, in a 1D resonator, also called a strip resonator, only a fraction $1/\Gamma_1 \Gamma_2$ of the energy initially contained in the wave returns to the same mirror after a full round-trip. Consequently, the round-trip loss is equal to $1 - 1/\Gamma_1 \Gamma_2$. For a 2D resonator the round-trip loss will be $1 - 1/(\Gamma_1 \Gamma_2)^2$.

Geometric optics tells us that the factor Γ is nothing but the linear round-trip magnification M of the optical system. *We thus see that the magnification, which is a purely geometrical concept, determines the losses, and, by consequence, the dynamics of the cavity.* This implies that the magnification is *the* natural parameter to specify an unstable cavity. All other characteristics, like the sensitivity of the cavity output to changes in cavity length, mirror radius of curvature, or mirror misalignment, can be phrased in terms of the magnification. Reference [43] provides a thorough analysis for the case of confocal unstable resonators.

Only with great difficulty can the present approach be generalized to resonators with more than 2 mirrors. We therefore will not pursue that route. Before ending this section we recast Eq. (2.10) into a form that eliminates any reference to the virtual centers: [32, 33]:

$$M = \pm \frac{1 + \sqrt{1 - (g_1 g_2)^{-1}}}{1 - \sqrt{1 - (g_1 g_2)^{-1}}} = \pm \frac{\sqrt{|g| + 1} + \sqrt{|g| - 1}}{\sqrt{|g| + 1} - \sqrt{|g| - 1}}, \quad (2.11)$$

where $g \equiv 2g_1 g_2 - 1$. We will return to this equation.

2.3.2. Ray-optics approach

Ray optics, especially when cast in its $ABCD$ -matrix form, has become one of the most popular formulations of geometric optics [5, 6, 36, 44]. Our aim here is to summarize the most relevant aspects of this description in connection with the problem of eigenmodes of an unstable resonator.

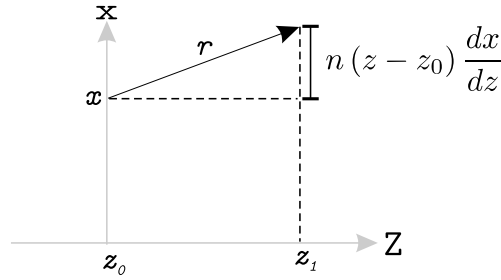


Figure 2.4: Two component representation of a ray \mathbf{r} . The crossing point of the ray with a plane Z_0 yields the component r_1 , labeled x in the graphic; the rate of change $n \frac{dx}{dz}$ yields the second component of the vector \mathbf{r} .

In the matrix description of geometrical optics a ray is represented by a two-component ray vector (\mathbf{r}). One component of the ray vector represents the distance of the ray to the optical axis (z) of the system, while the other represents the rate of change of this distance as we move along that axis, see Fig. 2.4. Here we assume that the medium is transversely homogeneous and characterized by the refractive index n [5, 44]. The ray vector is given by:

$$\mathbf{r} = \begin{pmatrix} x \\ n \frac{dx}{dz} \end{pmatrix}. \quad (2.12)$$

We also assume that each optical element extends infinitely in the transverse direction.

As we follow the ray through an optical system, its vector changes from one reference plane to another according to

$$\begin{pmatrix} x_2 \\ n \frac{dx_2}{dz} \end{pmatrix} = \begin{pmatrix} A & B \\ C & D \end{pmatrix} \begin{pmatrix} x_1 \\ n \frac{dx_1}{dz} \end{pmatrix}, \quad (2.13)$$

where \mathbf{r}_1 is the vector representing the ray at the first plane, \mathbf{r}_2 represents the ray at the second plane of the system, while the $ABCD$ matrix specifies the transformation of the ray. A complete optical system built of elements that by themselves are loss-free, is also characterized by an $ABCD$ matrix. The latter is simply the product of the transfer matrices of free-space propagation, and of refracting or reflecting elements, in the order that they are encountered while a ray traverses the optical system.

At this point, it is convenient to introduce a conceptual tool that is frequently used in cavity optics: the *equivalent periodic waveguide*. This is simply a periodic sequence of refractive optical elements that mimics the action of the various optical surfaces that a ray encounters as it goes back and forth through a cavity. The period of the sequence is equal to the length of a full round trip through the resonator (see Fig. 2.5). If the ray vector at the end of the unit cell is equal to a simple multiple of the vector at the beginning of that cell, this vector will remain "unchanged" when propagating through the whole infinite sequence. Obviously, such a ray vector is an eigen-ray (see [5]) of the unit cell and, thus of the cavity.

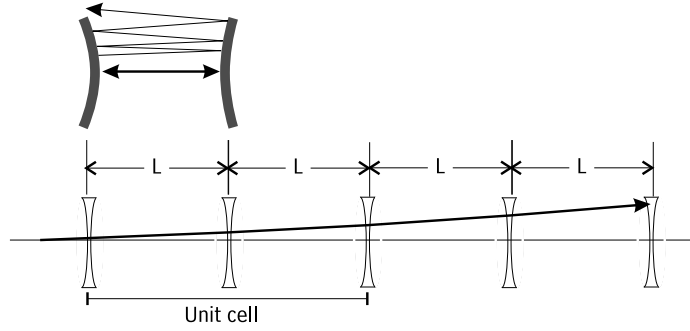


Figure 2.5: Unstable cavity (top) and its equivalent periodic waveguide (bottom). The figure also contains a sketch of the trajectory of a ray that traverses the system (thick solid line).

For our purpose we need only two $ABCD$ matrices:

1. The matrix describing propagation of the ray over a length L :

$$\mathbf{T}_L = \begin{pmatrix} 1 & L \\ 0 & 1 \end{pmatrix}. \quad (2.14)$$

2. The matrix describing reflection at a mirror

$$\mathbf{T}_{Ri} = \begin{pmatrix} 1 & 0 \\ -\frac{2}{R_i} & 1 \end{pmatrix}, \quad (2.15)$$

where R_i is radius of curvature of the mirror labeled i , chosen to be positive for concave mirrors.

As a starting point of our description of a ray's path we choose a plane in the center of one of the equivalent lenses. The transfer matrix for the unit cell will then be given by:

$$\begin{aligned} \mathbf{T}_{\text{rt}} &= \begin{pmatrix} 1 & 0 \\ -\frac{1}{R_1} & 1 \end{pmatrix} \begin{pmatrix} 1 & L \\ 0 & 1 \end{pmatrix} \begin{pmatrix} 1 & 0 \\ -\frac{2}{R_2} & 1 \end{pmatrix} \begin{pmatrix} 1 & L \\ 0 & 1 \end{pmatrix} \begin{pmatrix} 1 & 0 \\ -\frac{1}{R_1} & 1 \end{pmatrix}, \\ &= \begin{pmatrix} g & 2Lg_2 \\ (g-1)g_1/L & g \end{pmatrix}, \end{aligned} \quad (2.16)$$

where we used $g = 2g_1g_2 - 1$. This specific form of the ray-transfer matrix is a direct consequence of our choice of reference plane, and is not often encountered in the literature. The eigenvalues of the round-trip matrix, which are insensitive to this choice, are given by:

$$\lambda_1 = \left(g + \sqrt{g^2 - 1}\right) \quad \lambda_2 = \left(g - \sqrt{g^2 - 1}\right). \quad (2.17)$$

Note¹ that $\lambda_1\lambda_2 = 1$.

So far, our discussion applied to both stable and unstable resonators. Whereas the former have $|\lambda_i| = 1$, the latter are characterized by $|\lambda_i| \neq 1$. Since for unstable resonators the absolute value of g is larger than one (see the discussion in Section 2.2), both eigenvalues are real, and thus $\lambda_2 = \lambda_1^{-1}$. We now find the following expression for λ_1 :

$$\lambda_1 = \pm \frac{1 + \sqrt{1 - (g_1g_2)^{-1}}}{1 - \sqrt{1 - (g_1g_2)^{-1}}} = \pm \frac{\sqrt{g+1} + \sqrt{g-1}}{\sqrt{g+1} - \sqrt{g-1}}, \quad (2.19)$$

where the (\pm) sign indicates the type of resonator: $(+)$ for a positive-branch resonator and $(-)$ for a negative branch resonator.

The last expression reminds us of that for the magnification of the system, as in Eq. (2.11), and therefore we write:

$$\lambda_1 = M \quad \lambda_2 = 1/M. \quad (2.20)$$

We have already mentioned that the magnification M is the natural parameter for a description of the unstable optical resonator and therefore we recast the round-trip matrix in terms of the parameter M as:

$$\mathbf{P}_{\text{rt}} = \begin{pmatrix} \frac{M^2+1}{2M} & \frac{L}{g_1} \frac{(M+1)^2}{2M} \\ \frac{g_1}{L} \frac{(M-1)^2}{2M} & \frac{M^2+1}{2M} \end{pmatrix}. \quad (2.21)$$

¹There are certain constraints that a transfer matrix must fulfill in order to represent a physically realizable system. For the discussion at hand the most pertinent property is that its determinant must be equal to one,

$$\begin{vmatrix} A & B \\ C & D \end{vmatrix} = 1. \quad (2.18)$$

The reader can check for additional constraints in the literature [5,44].

The eigenvectors \mathbf{V}_1 and \mathbf{V}_2 , of this matrix have the general solution:

$$\mathbf{V}_1 = \begin{pmatrix} \frac{M-1/M}{2[\mathbf{P}_{\text{rt}}]_{21}} \\ 1 \end{pmatrix} \quad \mathbf{V}_2 = \begin{pmatrix} -\frac{(M-1/M)}{2[\mathbf{P}_{\text{rt}}]_{21}} \\ 1 \end{pmatrix}. \quad (2.22)$$

where $[\mathbf{P}_{\text{rt}}]_{ij}$ stands for the (i, j) element of the matrix \mathbf{P}_{rt} .

Equation (2.22) has a rather convenient form, because it shows that the eigenrays of the unstable resonator are distributed over a sphere. To see this we start by observing that if a vector \mathbf{V}_1 is an eigenvector, then a vector $\mathbf{V}'_1 = b\mathbf{V}_1$ is also an eigenvector. Then we calculate the crossing point of the \mathbf{V}_1 family with the z -axis (see Fig. 2.4):

$$P_{\mathbf{V}_1} = -\frac{L(M+1)}{g_1(M-1)}, \quad (2.23)$$

in other words, all the eigenrays of this resonator cross the axis at the same point. An unstable resonator has a *fan* of eigenrays.

Interestingly, the point $P_{\mathbf{V}_1}$ is the same virtual center of curvature found previously. This is not immediately obvious since we have chosen to write the $ABCD$ matrix with the reference plane in the "middle" of mirror 1. If we propagate the ray to the exterior of the lens, by writing,

$$\mathbf{V}_1'' = \begin{pmatrix} 1 & 0 \\ -\frac{1}{R_1} & 1 \end{pmatrix} \mathbf{V}_1 \quad (2.24)$$

and use the fact that $\lambda_1 = M$, (Eq. (2.20)) we obtain the following expression for P_1 :

$$P_1 = L \frac{\sqrt{1 - (g_1 g_2)^{-1}} - 1 + g_1^{-1}}{2 - g_1^{-1} - g_2^{-1}}, \quad (2.25)$$

exactly the same expression as Eq. (2.8). In other words, the *ad-hoc* treatment of Siegman, discussed in the previous section is contained on the geometrical-optics ABCD-matrix approach.

Let us examine what happens during the evolution of a ray through a cavity. We start by noticing that the system of eigenvectors $\mathbf{V}_1, \mathbf{V}_2$ form a linearly independent, *though not orthogonal*, set. Therefore, an arbitrary ray vector \mathbf{r}_i can be represented as a linear combination of these vectors:

$$\mathbf{r}_i = a\mathbf{V}_1 + b\mathbf{V}_2. \quad (2.26)$$

The interesting consequence of propagating this arbitrary input ray through the cavity is that, N round trips after, only the part coupled to the component \mathbf{V}_1 will survive [44]. This happens since N round-trips after, the ray is written as:

$$\begin{aligned} \mathbf{r}_{iN} &= (\mathbf{P}_{\text{rt}})^N \mathbf{r}_i \\ &= (\mathbf{P}_{\text{rt}})^N (a\mathbf{V}_1 + b\mathbf{V}_2) \\ &= aM^N \mathbf{V}_1 + bM^{-N} \mathbf{V}_2 \\ &\approx aM^N \mathbf{V}_1, \end{aligned} \quad (2.27)$$

Note that this result does not mean to say anything about the *intensity* of the mode after the N -th roundtrip, it simply says that the curvature of the fan of rays that remain inside the cavity, is equal to that of the fan associated with the eigenvector \mathbf{V}_1 . Note as well that this conclusion holds for all input conditions, except if \mathbf{r}_1 is parallel to \mathbf{V}_2 . In that case the rays will converge *ad-infinitum* towards the optical axis. This is not a physical situation, and, eventually, a fundamental limit that stops this convergence is reached. Nevertheless, we maximize the time that a ray spends inside the cavity by injecting purely along the fan of the eigenvector family \mathbf{V}_2 . This is the essence of the technique of adjoint coupling [45, 46]; this technique is used to optimize the pumping of unstable resonator lasers.

2.4. The eigenmodes according to wave optics

When we abandon the assumption that the wavelength of light is negligibly small we enter the realm of physical optics, and diffraction effects can no longer be ignored. Actually, in the wave-optics description of light propagation in an unstable cavity, diffraction plays an all-important role, because any wave injected in such a resonator will eventually come in contact with the edge of the confining aperture, which may simple be the rim of one of the mirrors.

Essential to a physical-optics description of light propagation is the use of diffraction theory in one of its variants. The key component of such a theory is the propagation kernel and we will spend some effort here in "deriving" the latter for a plano-convex resonator. This has two functions, namely, it connects elegantly with the eigenmodes according to the geometric-optics description, and helps us to identify the new elements that diffraction bring.

We start our discussion by formulating some approximations that permit us to handle the problem. We will assume i) that the wavelength λ of light is, by a large margin, the shortest linear dimension of the system; ii) that our cavity has a square aperture, and iii) that the side of such an aperture is substantially shorter than both the resonator's length L , or any of the radii of curvature of the cavity mirrors. By means of these approximations we justify the use of the Fresnel approximation for calculating the diffraction profile produced by the aperture [41, 42, 47, 48], and the use of the parabolic approximation to the phase shift of a wavefront as it traverses a lens [41, 42, 47, 49]. In addition, it can be shown [50] that, within these approximations, the propagation integral for an unstable resonator containing a square aperture can be separated, i.e., that the mode $\Phi(x, y)$ can be written as:

$$\Phi(x, y) = U(x) V(y). \quad (2.28)$$

Here U and V are functions of only x and y respectively, while the mode propagates along z . Each of the eigenfunctions U and V satisfies an independent eigenvalue equation. For the remainder of this section we will assume the aperture to be square so that the mode can be separated as in Eq. (2.28). The result of all the constraints mentioned in this paragraph is to approximate all curvatures encountered in the problem by parabolic surfaces, our treatment is thus a paraxial one. In view of the fact that the problem is separable we will, henceforth, *continue our discussion as if the problem is one-dimensional*.

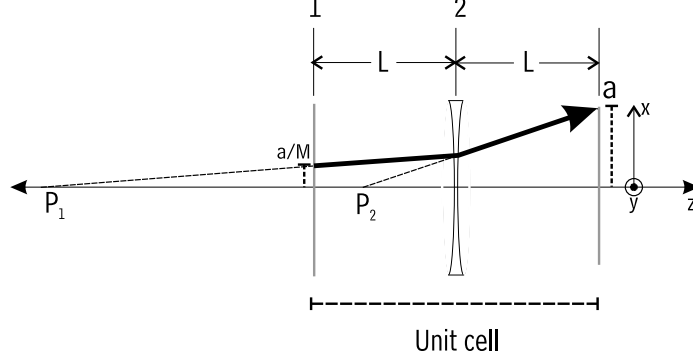


Figure 2.6: Unit cell of the equivalent waveguide of a plano-convex resonator, together with the virtual centers P_1 and P_2 of the geometric optics eigenmode, and the trajectory of an eigen-ray (think solid line).

Our analysis starts by taking a look at Fig. 2.6, where both the equivalent periodic waveguide of a plano-convex resonator and its fundamental mode according to geometric optics are shown. Our choice for this type of resonator is motivated by the fact that all mode parameters are determined by the curved mirror, and that we have used this type of resonator in our final series of experiments (see Chapter 6). For the remainder of this section we will adhere to this type of resonator.

Using Eq. (2.11), the fact that $g = 2g_1g_2 - 1$, and that $g_1 = 1$ for the plano-convex resonator, we find:

$$2g_2 - 1 = \frac{M^2 + 1}{2M}. \quad (2.29)$$

We can use this equation to express the radius of curvature of mirror 2 in terms of the round-trip magnification M , and length L of the cavity. We use the x as the transverse coordinate.

We position the square aperture of side $2a$ at the flat mirror and write the field profile just before the aperture as $G_{\text{in}}(x_{1\text{in}})$. After reflection in the mirror and diffraction by the aperture, the field in a plane just in front of the curved mirror, from here on labeled 2, can be written, using the Fresnel approximation [48, 51], as:

$$G_2(x_2) = r_1 e^{\frac{-i2\pi L}{\lambda}} \sqrt{\frac{i}{\lambda L}} \int_{-a}^a \exp\left[\frac{i\pi}{\lambda L} (x_{1\text{in}} - x_2)^2\right] G_{\text{in}}(x_{1\text{in}}) dx_{1\text{in}}. \quad (2.30)$$

Here r_1 is the amplitude reflectivity of the first mirror and, $e^{\frac{-i2\pi L}{\lambda}}$ represents the change of phase upon propagation from mirror 1 to mirror 2.

On its way back the field is affected by two processes; first, at the surface of mirror 2 it experiences a transverse phase shift due to the curvature of the mirror, and second, the field travels back to the mirror 1.

The transverse phase shift is given by:

$$\Delta\phi(x_2) = \frac{-2\pi x_2^2}{\lambda R} = \frac{\pi}{L\lambda} \frac{(M-1)^2}{2M} x_2^2,$$

where the (-) sign comes from the fact that $R < 0$ for a concave mirror. Multiplying by this term, and taking into account the reflectivity r_2 of the curved mirror we find the field at the flat mirror after one round-trip as:

$$G_{\text{out}}(x_{1\text{out}}) = \frac{ir_1 r_2 e^{-\frac{i4\pi L}{\lambda}}}{\lambda L} \int_{-\infty}^{\infty} \left[\int_{-a}^a e^{\frac{i\pi}{\lambda L} (x_{1\text{in}} - x_2)^2} G_{\text{in}}(x_{1\text{in}}) dx_{1\text{in}} \right] e^{\frac{i\pi}{\lambda L} \left[(x_2 - x_{1\text{out}})^2 + \frac{(M-1)^2}{2M} x_2^2 \right]} dx_2,$$

where we assumed mirror 2 to be infinitely large.

Exchanging the order of the integrals, grouping together all the factors that depend on the coordinate x_2 , and using the relation [52]:

$$\int_{-\infty}^{\infty} e^{-p^2 x^2 \pm qx} dx = \frac{\sqrt{\pi}}{p} \exp \left[\frac{q^2}{4p^2} \right], \quad (2.31)$$

we obtain:

$$G_{\text{out}}(x_{1\text{out}}) = K \int_{-1}^1 e^{\frac{i\pi a^2}{\lambda L} \left[\frac{M^2+1}{(M+1)^2} (x_{1\text{in}}^2 + x_{1\text{out}}^2) - 2x_{1\text{in}} x_{1\text{out}} \frac{2M}{(M+1)^2} \right]} G_{\text{in}}(x_{1\text{in}}) dx_{1\text{in}}, \quad (2.32)$$

$$K = r_1 r_2 e^{-\frac{i4\pi L}{\lambda}} \sqrt{\frac{i2M}{(M+1)^2} \frac{a^2}{L\lambda}}$$

By introducing the effective Fresnel number we can make a transformation that considerably simplifies the diffraction integral. Following Horwitz [32] we express the effective Fresnel number N_{eff} by first introducing the so-called collimated Fresnel number N_{coll} :

$$N_{\text{coll}} = \frac{1}{2g_2} \frac{a^2}{\lambda L}. \quad (2.33)$$

Next, N_{eff} is given by:

$$N_{\text{eff}} = \sqrt{g^2 - 1} N_{\text{coll}},$$

$$= \frac{1}{2} \left(M - \frac{1}{M} \right) N_{\text{coll}}, \quad (2.34)$$

with $g = 2g_1 g_2 - 1$.

The collimated Fresnel number multiplied by the magnification M determines the maximum spatial frequency of the function $U(x)$. The effective Fresnel number determines the curvature of the wavefront (see references [5, 51] for a more detailed discussion).

For our plano-convex resonator¹ these Fresnel numbers can be expressed in terms of the magnification as:

| | |
|---|---|
| Collimated Fresnel number (N_{coll}) | $\frac{2M}{(M+1)^2} \frac{a^2}{L\lambda}$ |
| Effective Fresnel number (N_{eff}) | $\frac{M-1}{M+1} \frac{a^2}{\lambda L}$ |

Table 2.1: Expressions of the relevant Fresnel numbers for a plano-convex cavity.

By introducing

$$U(x) = e^{-i\pi N_{\text{eff}} x^2} G(x), \quad (2.35)$$

we can write the diffraction integral as:

$$U_{\text{out}}(x_{1\text{out}}) = K \int_{-1}^1 \exp \left[i\pi M N_{\text{coll}} \left(x_{1\text{in}} - \frac{x_{1\text{out}}}{M} \right)^2 \right] U_{\text{in}}(x_{1\text{in}}) dx_{1\text{in}}. \quad (2.36)$$

For U to be an eigenmode we require that the fields U_{in} , and U_{out} are identical except for a multiplicative factor γ :

$$\gamma U(x_{1\text{out}}) = K \int_{-1}^1 \exp \left[i\pi M N_{\text{coll}} \left(x_{1\text{in}} - \frac{x_{1\text{out}}}{M} \right)^2 \right] U(x_{1\text{in}}) dx_{1\text{in}}. \quad (2.37)$$

We want to make some last remarks about the Huygens-Fresnel integral for unstable resonators. First, Eq. (2.37) only applies when the intracavity aperture is placed at or very near to, one of the cavity mirrors. Second: the value of the collimated Fresnel number (see Eq. (2.33)) depends on g_2 . Consequently all the parameters will change when the intracavity aperture is moved from one mirror to the other.

For a *general* unstable cavity (not necessarily plano-convex) the divergent eigenmodes are described by the following relations [32]:

$$\begin{aligned} \gamma U(x_{\text{out}}) &= K_2 \int_{-1}^1 \exp \left[-i\pi M N_{\text{coll}} \left(x_{\text{in}} - \frac{x_{\text{out}}}{M} \right)^2 \right] U(x_{\text{in}}) dx_{\text{in}} \\ U(x) &= e^{-i\pi N_{\text{eff}} x^2} G(x) \\ N_{\text{eff}} &= \frac{1}{2} \left(M - \frac{1}{M} \right) N_{\text{coll}} \\ K_2 &= r_1 r_2 e^{\frac{-i4\pi L}{\lambda}} \sqrt{i N_{\text{coll}}} \\ N_{\text{coll}} &= \frac{1}{2g_2} \frac{a^2}{L\lambda}. \end{aligned} \quad (2.38)$$

¹Note that the values in the table apply only to the case of a plano-convex resonator. In most of the literature the problem of unstable-resonator eigenmodes is analyzed for a confocal positive-branch resonator, where the parameters have different functional forms in terms of the magnification.

2.5. Finding the eigenmodes: Asymptotic expansion

It is not a trivial task to find good approximations to the solution of Eq. (2.38) because in many interesting cases the collimated Fresnel number (N_{coll}) is large; even direct numerical integration proves to be tricky. Many techniques have been developed to simplify the diffraction problem such as the continuous Fourier-transform method [53], exotic special functions [54], special forms of the coupled-mode theory [55,56], etc. Most of these approximations were developed at a time when unstable cavities were primarily seen as a tool to build high-power lasers. Consequently, the main goal was to find methods to reliably estimate the losses (i.e. the eigenvalues) of the laser mode while the structure of the modes (i.e. the eigenfunctions) was considered unimportant.

An important breakthrough in unstable-resonator research occurred when Horwitz [32, 57] applied the technique of asymptotic expansions to the analysis of the mode structure of an unstable resonator with a square aperture. His approach was extended to study resonators with circular apertures [58,59], and strip resonators¹ near the edge of stability [60]. These techniques evolved into what has become known as Virtual Source Theory [26, 27]. In this section we will focus on the essentials, bringing out what is most relevant to analyze the fractal properties of the modes of unstable cavities.

All approximative methods that we just mentioned have in common that they depart from a simplification of Eq. (2.38) by using the stationary-phase approximation. The essence of this method is rather simple: Suppose we have an integral of the form:

$$I(x_1, x_2) = \int_{x_1}^{x_2} g(x) \exp[ikf(x)] dx. \quad (2.39)$$

When k is large the exponential factor will oscillate rapidly and give rise to a vanishing contribution to the integral, except near the points x_s where the function $f(x)$ is constant ($f'(x_s) = 0$). These points are called *stationary points*. An additional contribution will come from the end points x_1 and x_2 . Thus, we can write the integral as:

$$I(x_1, x_2) \approx \sum F[g(x_s)] + \varkappa(x_1) + \varkappa(x_2), \quad (2.40)$$

where the summation accounts for the possibility of having more than one stationary point. The term F in Eq. (2.40) accounts for the contribution of the stationary points, while the terms \varkappa yield the end-point contributions. The power of the Stationary-Phase Method lies in the possibility of using well-defined procedures to construct, in a systematic fashion, the contributions from both the stationary and end points, to an arbitrary order of approximation. The reader who is interested in the general form of the method is invited to read the detailed and general description, for both uni- and bi-dimensional integrals, in the book by Stamnes [47]. Most of the advanced textbooks on optics include introductions to the Stationary-Phase Method [42,61,62]. We will introduce the method in an *ad-hoc* fashion, using those elements that are essential.

¹ An strip resonator is an unstable resonator with 1D mirrors; it can be made used cylindrical mirrors.

2.5.1. Stationary phase contribution

We start by comparing Eq. (2.39) with the canonical propagation equation for unstable resonators (Eq. 2.38), identifying the factor k of Eq.(2.39) with the factor πMN_{coll} of Eq.(2.38). The latter factor is rather large, even for a resonator of modest size. The exponential has a single stationary point, $x_s = x_{\text{out}}/M$. Following Stamnes [47], we write for the contribution of the stationary point:

$$F[U(x_s)] = K_2 \int_{-1-x_s}^{1-x_s} e^{-i\pi MN_{\text{coll}} t^2} \left[U(x_s) + \frac{dU}{dt} \Big|_{x_s} t + \frac{1}{2} \frac{d^2 U}{dt^2} \Big|_{x_s} t^2 + \dots \right] dt \quad (2.41)$$

with $t = x_s - x_{\text{out}}/M$. The field $U(x_{\text{in}})$ has been expanded in a Taylor series around the stationary point x_s . The stationary-phase contribution to the field at a point with coordinate x , located in the front (output) of the unit cell, originates at a point with coordinate x/M located in the rear (input) of that cell. Figure 2.7 shows that when the magnification M is large the

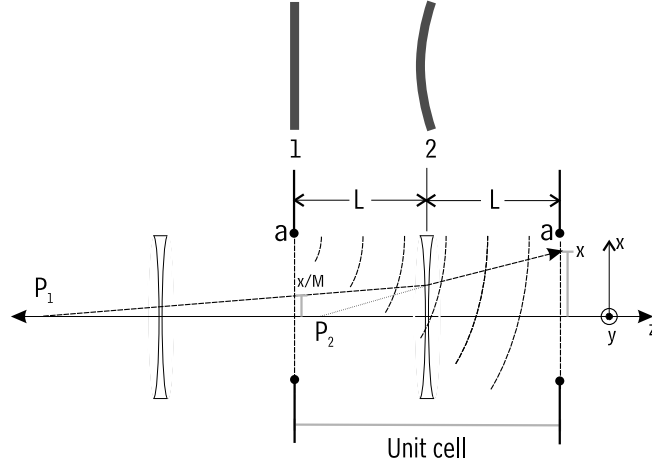


Figure 2.7: Different contributions to the propagation integral in a high- M plano-convex unstable-cavity of aperture size $2a$. The straight lines represent the stationary contribution, the curves the end-point contribution, $\varkappa[U(1)]$.

stationary point will lie far from the edge of the aperture, close to the axis of the equivalent lens guide. It is then allowed to move the integration limits to infinity without affecting the result. Then all odd powers in the series expansion of U vanish. Assuming that the field varies so slowly that the contributions of the higher derivatives are zero, we find:

$$F[U(x)] = r_1 r_2 \sqrt{iN_{\text{coll}}} e^{-\frac{i4\pi L}{\lambda}} U(x/M) \int_{-\infty}^{\infty} e^{-i\pi MN_{\text{coll}} t^2} dt, \quad (2.42)$$

and evaluating the integral, using Eq. (2.31), we obtain:

$$\gamma U(x) = e^{-i\frac{4\pi L}{\lambda}} r_1 r_2 \frac{U(x/M)}{\sqrt{M}} + r_1 r_2 \sqrt{iN_{\text{coll}}} e^{-\frac{i4\pi L}{\lambda}} [\varkappa(1, x) + \varkappa(-1, x)]. \quad (2.43)$$

We see that the functional¹ F acts like a linear map of the field across the transverse plane, taking the role of a geometric-optics propagator. That being said, it becomes tempting to associate the functionals \mathcal{F} with the diffractive propagator since, in their absence, important physical parameters such as the diffraction limit and the aperture size are not included in our description. This discussion is postponed to section 2.6.

Neglecting the edge contributions we obtain the *purely geometrical* form of the propagation integral [51]:

$$\gamma U(x) = e^{-i\frac{4\pi L}{\lambda} r_1 r_2} \frac{U(x/M)}{\sqrt{M}}. \quad (2.44)$$

One well-known family of eigenfunctions of this geometrical eigenvalue equation is [51]:

$$U_n(x) = x^n \quad \gamma_n = \frac{e^{-i\frac{4\pi L}{\lambda} r_1 r_2}}{M^{n+1/2}}. \quad (2.45)$$

Strictly speaking, these functions provide a non-physical solution since they diverge at infinity. Nevertheless, they have proven useful in the context of explaining why the losses of the fundamental mode of the resonator are synchronized with the effective Fresnel number [63].

There is another family of eigenfunctions of the purely geometric propagator that has, to our knowledge, been overlooked, but perfectly fits into the postulate of Karman and Woerdman [8]. These functions are closely related to the Mandelbrot-Weierstrass function (see Eq. (1.2)) and can be written as:

$$M_D(x) = \sum_{n=-\infty}^{\infty} \frac{e^{iM^n x}}{M^{(2-D)n}}, \quad (2.46)$$

with $0 \leq D \leq 2$, and eigenvalue:

$$\gamma_D = \frac{e^{-i\frac{4\pi L}{\lambda} r_1 r_2}}{M^{1/2} M^{(2-D)}}. \quad (2.47)$$

The lowest-loss geometric mode of our 1D (strip) resonator corresponds to the function $M_2(x)$, and therefore has fractal (box) dimension 2 (see Section 1.1.1 for the box dimension of the Mandelbrot-Weierstrass function).

Interestingly, *all* periodic functions $A(x/\tau)$, of period τ , can be used to construct solutions of the purely geometric eigenvalue equation (Eq. 2.44). These generalized solutions J_D are built by mimicking the structure of the Mandelbrot-Weierstrass function:

$$J_D(x) = \sum_{n=-\infty}^{\infty} \frac{A(M^n x/\tau)}{M^{(2-D)n}}. \quad (2.48)$$

The eigenvalues of this solution are also given by Eq. (2.47). Note that the solutions that we have obtained here are also fractal. Nevertheless, we can not be sure that the value of the parameter D that appears in their definition is equal to their box dimension, unless the functions $A(x/\tau)$ are harmonic, as in the M_D function (Eq. (2.46)), or in the Mandelbrot-Weierstrass function (see Eq.(1.2)).

¹ A functional is a function that takes functions as its argument

At this point we must turn the attention of the reader to one particular characteristic of the structure of the family of eigenfunctions that we have just found: they are composed of multiple (reduced) copies of themselves. Functions M_D and J_D fit in to the most general definition by Mandelbrot [9] of what a fractals is: a fractal is a rough or fragmented geometric shape that can be subdivided into parts, each of which is (at least approximately) a reduced copy of the whole (see section 1.1).

2.6. Eigenfunctions of an unstable resonator: the Virtual Source Theory

As was shown in Section 2.5.1, the purely geometrical form of the propagator (Eq. 2.44) supports both algebraic and fractal eigensolutions. This lack of uniqueness occurs because the diffractive contributions from the end points were neglected, whence the boundary conditions of the system remained unspecified. In the present section we will resolve this issue. We will answer three important questions: i) does the system prefer the fractal or the algebraic eigenfunctions?, ii) if the system prefers the fractal eigenfunctions, what is the dimension of the fundamental mode?, and iii) what are the limits of this behavior?.

We start by transforming the Huygens-Fresnel integral (Eq. 2.38):

$$\gamma U(x_{\text{out}}) = r_1 r_2 e^{\frac{-i4\pi L}{\lambda}} \sqrt{iN_{\text{coll}}} \int_{-1}^1 e^{-i\pi MN_{\text{coll}}(x_{\text{in}} - \frac{x_{\text{out}}}{M})^2} U(x_{\text{in}}) dx_{\text{in}}, \quad (2.49)$$

to a form that emphasizes the relevance of the resonator size (the parameter that justifies an expansion in virtual sources). By introducing the variables $t = \pi MN_{\text{coll}}$, $\xi = \gamma/\beta$ and $\beta = \frac{r_1 r_2 e^{\frac{-i4\pi L}{\lambda}}}{\sqrt{M}}$, Eq. (2.49) can be cast in the more attractive form [32]:

$$\xi U(x_{\text{out}}) = \sqrt{\frac{it}{\pi}} \int_{-1}^1 e^{-it(x_{\text{in}} - \frac{x_{\text{out}}}{M})^2} U(x_{\text{in}}) dx_{\text{in}}. \quad (2.50)$$

The eigenvalue ξ of the mode $U(x)$ is normalized to the loss of the geometric-optics eigenvalue $|\beta|$. In other words: a geometric-optics unstable resonator has an eigenvalue ξ equal to 1. The advantage of the use of normalized eigenvalues will become clear when we study the structure of the eigenmodes.

The whole treatment here is based on an asymptotic expansion of the propagation integral (Eq. (2.50)), which requires that the magnification M is sufficiently large, in practice $M > 1.4$. This expansion is discussed in some detail in Appendix A (see also Ref. [32]). For resonators with sufficiently large Fresnel number ($a^2/\lambda L > 100$)¹ the integral equation (2.50) for the even modes² can be written as:

$$\xi U(x) = U(x/M) - \frac{U(1)}{2\sqrt{i\pi t}} \left[\frac{e^{-it(1+x/M)^2}}{1+x/M} + \frac{e^{-it(1-x/M)^2}}{1-x/M} \right], \quad (2.51)$$

¹In practice the approximation has been shown to work already at Fresnel numbers of about 5 [64].

²The odd modes are treated in an analogous fashion, with the plus sign between the two terms inside the brackets replaced by a minus sign.

where the eigenfunctions $U(x)$ are restricted to the domain $[-1, 1]$. We will now proceed to find its solutions.

2.6.1. Expansion in Virtual Sources

By introducing the approximations that lead to Eq.(2.51) we have made a major step towards solving the eigenvalue equation. Southwell [26, 27] developed a practical method to find the solution of Eq. (2.51); this method is known as the Virtual Source Theory. We will introduce that theory in two steps: first, we will study the decay of a simple (plane-wave) field configuration that circulates through the resonator. This serves to identify a family of functions that are intrinsically associated with the intra-cavity propagation of a field. Under round-trip propagation the elements of this family of functions are mapped onto each other according to a well-defined hierarchy; due to this self-mapping property they constitute an ideal basis set to build the solutions of the eigenvalue equation.

In the second step we use a linear combination of virtual sources to solve Eq. (2.51). We restrict our discussion to the principal points of the derivation; the reader interested in more details can take a look at references [26, 27]. The final part of this Chapter is devoted to study the structure of the solutions found by Virtual Source Theory. This analysis provides answers to the questions formulated at the beginning of Section 2.6.

What happens to a plane wave injected into an unstable resonator

The field E_{out} at the output of the unit cell of Fig. 2.7 is related to the field E_{in} at its input, by the Huygens-Fresnel diffraction integral:

$$E_{\text{out}}(x_{\text{out}}) = r_1 r_2 e^{-\frac{i4\pi L}{\lambda}} \sqrt{iN_{\text{coll}}} \int_{-1}^1 e^{-it(x_{\text{in}} - \frac{x_{\text{out}}}{M})^2} E_{\text{in}}(x_{\text{in}}) dx_{\text{in}}. \quad (2.52)$$

Using an expansion similar to the one that resulted in Eq.(2.51) we can rewrite Eq. (2.52) as:

$$E_{\text{out}}(x) = \beta \left(E_{\text{in}}(x/M) - \frac{E_{\text{in}}(1)}{2\sqrt{i\pi t}} \left[\frac{e^{-it(1+x/M)^2}}{1+x/M} + \frac{e^{-it(1-x/M)^2}}{1-x/M} \right] \right). \quad (2.53)$$

Equation (2.53) is our starting point; we inject a plane wave ($E_0(x) \equiv 1$) into the resonator. After a single round trip the plane wave has evolved into:

$$E_1(x) = \beta \left(1 - \frac{1}{2\sqrt{i\pi t}} \left[\frac{e^{-it(1-x/M)^2}}{1-x/M} + \frac{e^{-it(1+x/M)^2}}{1+x/M} \right] \right). \quad (2.54)$$

In words: the field at the output is the result of the interference between the injected plane wave and an edge wave that arises from the scattering of the plane wave by the edges of the aperture. Both fields are attenuated by a factor β equal to the losses of the geometric-optics eigenmode.

After two round trips the field configuration is given by:

$$E_2(x) = \beta^2 - \frac{\beta^2}{2\sqrt{i\pi t}} \left[\frac{e^{-it(1-x/M^2)^2}}{1-x/M^2} + \frac{e^{-it(1+x/M^2)^2}}{1+x/M^2} \right] - \frac{\beta E_1(1)}{2\sqrt{i\pi t}} \left[\frac{e^{-it(1-x/M)^2}}{1-x/M} + \frac{e^{-it(1+x/M)^2}}{1+x/M} \right]. \quad (2.55)$$

By examining the structure of Eq. (2.55) we find that, during the second round trip, the wave $E_1(x)$ is expanded by a factor M (and therefore its amplitude is reduced by an additional factor β) while its interaction with the aperture generates a fresh edge wave (the third term), exactly as it occurred during the first round trip (see Eq. 2.54).

This process continues for a while: each time that the wavefront circulates through the cavity a new edge wave is created, while the existing profile is expanded by a factor equal to the magnification of the resonator¹. Thus, after m iterations the field configuration is given by:

$$E_m(x) = \beta^m + \sum_{n=1}^m a_n D_n(x), \quad (2.56)$$

with a_m a weighting factor, and D_n , the n -th edge wave, given by:

$$D_n(x) = -\frac{1}{2\sqrt{i\pi t}} \left[\frac{e^{-it(1-x/M^n)^2}}{1-x/M^n} + \frac{e^{-it(1+x/M^n)^2}}{1+x/M^n} \right] = -\frac{1}{\sqrt{i\pi t}} \left[\cos\left(\frac{2t}{M^n}x\right) + i\frac{x}{M^n} \sin\left(\frac{2t}{M^n}x\right) \right] \frac{e^{-it\left(1+\frac{x^2}{M^{2n}}\right)}}{1-\frac{x^2}{M^{2n}}}. \quad (2.57)$$

Within the aperture ($-1 \leq x \leq 1$) the spatial variation of the edge waves becomes less rapid going from $D_n(x)$ to $D_{n+1}(x)$. At a certain value of n , hereafter labeled N , the spatial variation of the edge wave, $D_N(x)$, within the aperture is negligible. From that point on it is useless to continue the expansion in terms of edge waves and we can write

$$E_N(x) = \beta^N + \sum_{n=1}^N a_n D_n(x). \quad (2.58)$$

Horwitz [32] has proposed a rather strict criterium for the value of N ,

$$N \approx \frac{\log(250N_{\text{eff}})}{\log M}. \quad (2.59)$$

For a cavity with $M = 2$ and $N_{\text{eff}} = 1000$, this yields $N = 18$.

¹This process has been called the Monitor-Outside-a-Monitor effect [65–69]

Solving the eigenmode equation

The solution of the eigenvalue equation for the case of a confocal positive-branch unstable resonator by means of an expansion in virtual sources was introduced in references [26, 27]¹. Here we summarize the main points of this procedure, but we do not limit ourselves to a particular resonator architecture. Consequently, this theory also applies to the nonconfocal resonator used in Chapter 6.

Our starting point is, again, the approximate eigenvalue equation (2.51),

$$\xi U(x) = U(x/M) - \frac{U(1)}{2\sqrt{i\pi t}} \left[\frac{e^{-it(1+x/M)^2}}{1+x/M} + \frac{e^{-it(1-x/M)^2}}{1-x/M} \right],$$

which can be written as:

$$\xi U(x) = U(x/M) + U(1) D_1(x). \quad (2.60)$$

Virtual Source Theory involves the following Ansatz [26, 27] for the eigenmodes of this equation:

$$U(x)_{(N)} = \beta^N + \sum_{m=1}^N \beta^{N-m+1} D_{N-m+1}(x) c_m, \quad (2.61)$$

where c_m is the strength of the m -th virtual source, and N is the number of virtual sources that is supported by the cavity² (see Eq. 2.59). The factor β^{N-m+1} appears because the contribution to the eigenmodes of a given virtual source is modified by a factor β after each round trip. We now substitute the Ansatz into Eq. (2.60) and use the fact that:

$$D_n(x/M) = D_{n+1}(x), \quad (2.62)$$

to arrive at the following relations:

$$\begin{aligned} c_1 &= \frac{\xi - 1}{D_{N+1}(1)}, \\ c_m &= (\gamma)^{m-1} c_1, \\ U(1) &= c_{N+1}, \\ \gamma^N c_1 &= \beta^N + \sum_{m=1}^N \beta^{N-m+1} D_{N-m+1}(1) \gamma^{m-1} c_1. \end{aligned} \quad (2.63)$$

Substituting the value of c_1 , we obtain a polynomial equation for the eigenvalues:

$$\xi^{N+1} - (1 + D_1(1)) \xi^N + \sum_{m=0}^{N-1} (D_{N-m}(1) - D_{N-m+1}(1)) \xi^m = 0. \quad (2.64)$$

¹The concept of virtual sources was introduced in reference [70], where it was demonstrated, geometrically, that the solutions of the eigenvalue equation can be built as the sum of the fields radiated by a set of Virtual Apertures. Southwell's [26, 27] important contribution to Virtual Source Theory is that he introduced suitable approximations that make the virtual-source approach both practical and precise.

²Note that this implies that an unstable resonator supports a limited number of modes, and that this number grows very slowly with the size of the resonator.

The eigenmodes are given by:

$$U_\xi(x) = 1 + \sum_{m=1}^N \xi^{m-1} D_{N-m+1}(x) \frac{\xi - 1}{D_{N+1}(1)}. \quad (2.65)$$

Below we will study these eigenmodes in some detail.

As shown in Appendix B, for practical unstable cavities the largest ($|\xi|$) eigenvalue has $|\xi| \approx 1$. This eigenvalue corresponds to the fundamental mode.

2.6.2. Eigenmodes of unstable resonators: Fractality

We start by studying a limiting case, i.e., a resonator with very large Fresnel number. For such a resonator, for which $t \rightarrow \infty$, the only possible solution is a plane wave, with eigenvalue $\xi = 1$. In that case we see from Eq. (2.63) that $c_1 = 0$ so that $c_n = 0$ for all values of n . The eigenvalue and eigenmode are given by:

$$\gamma = \beta = \frac{r_1 r_2 e^{-4i\pi \frac{t}{\lambda}}}{\sqrt{M}} \quad U(x) = 1, \quad (2.66)$$

i.e., exactly the solution predicted by geometrical optics.

A more interesting situation arises when we study the solutions for a resonator of finite Fresnel number. Substituting Eq.(2.57) into Eq.(2.65), we obtain the eigenmodes:

$$U_\xi(x) = 1 + \frac{\xi - 1}{\sqrt{i\pi t} D_N(1)} \sum_{m=0}^{N-1} \xi^m \left[\cos\left(\frac{2t}{M^N} M^m x\right) + i \frac{M^m x}{M^N} \sin\left(\frac{2t}{M^N} M^m x\right) \right] \frac{e^{-it\left(1 + \frac{x^2 M^{2m}}{M^{2N}}\right)}}{1 - \frac{x^2 M^{2m}}{M^{2N}}}. \quad (2.67)$$

When $m \ll N$, i.e., at low spatial frequencies, only the cosine term contributes significantly to the eigenmode; therefore, at those spatial frequencies the eigenmode can be approximated by:

$$U_\xi(x) \approx 1 + \frac{\xi - 1}{\sqrt{i\pi t} D_N(1)} \sum_{m=0}^{N'} \xi^m \cos\left(\frac{2t}{M^N} M^m x\right), \quad (2.68)$$

with $N' < N$. It is interesting to compare this low-spatial-frequency approximation to the eigenmodes with the expression for the modes based on the Mandelbrot-Weierstrass function, given in Eq. (2.46). Realizing that the eigenvalues ξ in Eq.(2.68) are all smaller or equal to one, one sees that the similarity between these expressions suggests that the eigenmodes of the unstable resonator are fractals, as predicted in references [8, 25]. Here we emphasize that the similarity between the eigenmode of an unstable resonator and the geometric eigenmode (Eq. (2.46)) holds only in the low- and middle-range of spatial frequencies, i.e., precisely where geometric-optics provides a good description of the propagation of light.

By comparing Eq. (1.2) and Eq. (2.68) we obtain a relation between the eigenvalue ξ and the box dimension D of the mode:

$$\frac{1}{M^{2-D}} = \xi \rightarrow D_{\text{box}} = 2 + \frac{\log \xi}{\log M}. \quad (2.69)$$

This same relation was obtained using a different technique by Yates and New [31].

To find the fractal dimension of the fundamental mode we need an estimate of its eigenvalue. Note that this eigenvalue can not be exactly equal to 1 since, according to relation (2.65), this implies that the eigenmode is a plane wave. Using the method described in appendix B, we find that the eigenvalue ξ_0 is contained within a band given by (Eq.B.11):

$$1 - \frac{\log_M(250t)}{\sqrt{\pi t} - \log_M(250t)} < \xi_0 < 1 + \frac{\log_M(250t)}{\sqrt{\pi t} - \log_M(250t)}.$$

For sufficiently large values of the parameter t this yields $\xi_0 \approx 1$. Therefore the fractal (D_{box}) dimension of the fundamental mode of an unstable resonator is, on average, equal to 2. This agrees with the value of the Fourier dimension calculated by Berry *et al.* [29].

The Fourier dimension of the fundamental mode of an unstable resonator

Our argument about the fractal character of the eigenmodes of an unstable resonator is restricted in the sense that it does not apply to all spatial-frequency scales. Moreover, the argument was formulated in terms of the field and not in terms of the intensity distribution. Consequently, our prediction can not be directly tested in an experiment.

Berry and collaborators [29, 30] took the Fourier approach (see Section 1.1.2) which avoids these issues. They showed that the power spectrum of the fundamental modes of a confocal positive-branch unstable-resonator follows a power-law

$$P^2(k) \approx \frac{P(0)}{k^\beta}, \quad (2.70)$$

which implies that the mode is fractal, and has Fourier dimension $D_F = (5 - \beta)/2$. They then showed that $D_F = 2$ for the one-dimensional problem considered here.

Figure 2.8 shows both the intensity distribution and the power spectrum of the two lowest-order even modes of a plano-convex unstable resonator calculated with the formalist developed in this chapter. In the low and intermediate spatial-frequency range the spectrum is dominated by spikes, each corresponding to an individual virtual source. At high spatial frequencies the spikes have merged into a continuum. Nevertheless, the scaling relation is obeyed through the whole frequency range, as shown by the fit (thick solid line).

The treatment based on the power spectrum has the advantage of being directly comparable with experimental results and therefore this method will be used to evaluate our experimental data.

2.7. Conclusion

At the beginning of Section 2.6 we formulated the following questions: i) does the system prefer the fractal or the algebraic eigenfunctions? ii) if the system prefers the fractal eigenfunctions, what is the fractal dimension of the fundamental mode? and iii) what are the limits of this behavior? We have found the following answers:

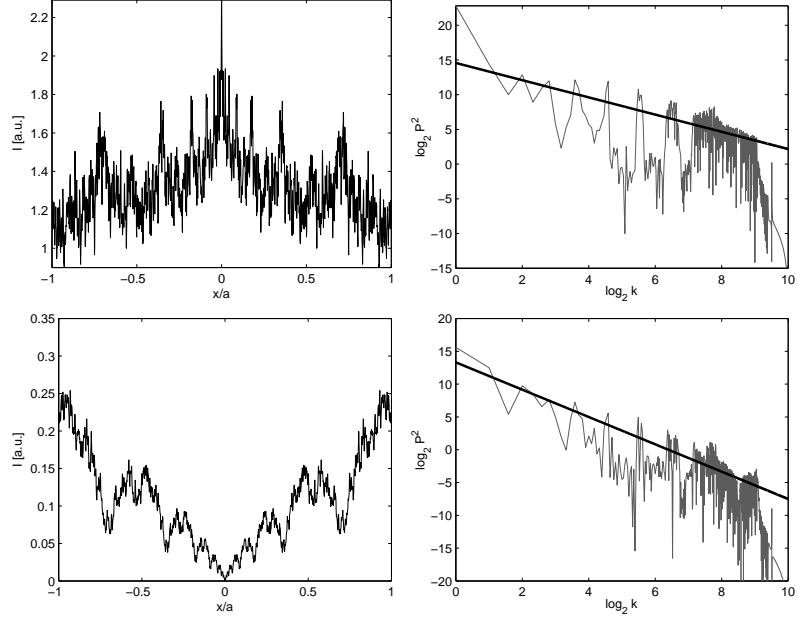


Figure 2.8: Top row: the intensity distribution (left) and associated power spectrum (right, plotted on a log-log scale) of the fundamental mode of a plano-convex unstable cavity, with magnification $M = 2$, and Fresnel number $N_F \approx 500$. The mode has a scale eigenvalue $\xi = 1.03$ and Fourier fractal dimension $D_F = 2.02$. Bottom row: similar graphs for the first excited even mode of the same cavity. Here $\xi = 0.77 - 0.15i$, $D_F = 1.45$.

1. The modes of unstable resonators are deterministic self-affine fractals, whose fractal dimension is related to their loss by means of the relation (Eq. 2.69)),

$$D_{\text{box}} = 2 + \frac{\log \xi}{\log M},$$

where ξ is the scaled eigenvalue of the mode, and M the magnification of the cavity.

2. The fundamental mode of an unstable resonator has, on average, a box-counting dimension $D_{\text{box}} = 2$ for low- and mid-range spatial frequencies, and a Fourier dimension $D_F = 2$ for all spatial frequencies.
3. This behavior requires that the magnification M should be larger than 1.4, and that the collimated Fresnel number N_{coll} of the resonator should not be too small, say of order 32.

Chapter 3

Behold the darkness!

3.1. Introduction

The previous chapter dealt with the theoretical background required to understand why the eigenmodes of unstable resonators are fractal. It concluded with the prediction that the Fourier fractal dimension of the lowest order mode of a unstable strip resonator is equal to 2. This agrees with the prediction by Berry [29] that the Fourier dimension of the fundamental mode of two-dimensional confocal positive-branch unstable resonators has a value equal to 2. In the remainder of this thesis I discourse on our effort aimed to test the validity of these predictions.

The general idea of the experiment is to inject light into an unstable cavity, make use of the self-filtering properties of such a cavity to reduce the contribution of higher order modes to the overall intensity profile, and capture the resulting pattern by means of a suitable camera. It is then possible to analyze the fractal characteristics of this pattern by means of one of the standard characterization methods for fractals [16]; here we choose the Fourier method in view of the fact that Berry *et al.* [29, 30] used this approach in their theoretical work, and we aim to compare our experimental results against that theory.

In the present chapter the design of the experiment is worked out. It starts with an overview of possible approaches with their advantages and problems. We give estimates of some key experimental parameters that specify the light source that we need. The second part of the chapter covers our search for a source fulfilling our requirements.

3.2. How to isolate the fundamental mode of a cavity

The natural approach to study the lowest-loss eigenmode of an optical resonator is to build a laser with that cavity, since the lasing mechanism preferentially selects this mode. This method has been in use for many decades; it works well for stable resonators because their eigenmodes have a small volume and it is thus relatively easy to insert an amplifying medium with transversely homogeneous gain. Unfortunately, this approach does not work well for unstable resonators, because their eigenmodes fill the entire volume of the cavity

and it is virtually impossible to insert a gain element which is sufficiently homogeneously pumped.

Consequently, for eigenmode studies of an unstable resonator the "laser approach" is out. What remains is to characterize the eigenmodes of the *passive* cavity. That means that we are faced with the full consequences of the fact that unstable resonators are inherently very lossy. The transverse eigenmodes of the cavity are thus spectrally broad and indistinguishable. However, just as in the case of a stable resonator, the loss of the fundamental mode of an unstable resonator is lower than that of the higher-order transverse modes. In fact, the relative loss difference between the lowest-loss and higher-loss modes is much larger in an unstable than in a stable cavity [5], so this works to our advantage.

Thus, when a superposition of modes of an unstable resonator is excited during a limited time interval, the fundamental mode will lose its energy at a slower rate than any of the other eigenmodes of that cavity: in the time domain the cavity is self-cleaning. This is the approach we take to study the fractal properties of the fundamental mode of an unstable resonator. In a different context the method is known as cavity ring-down [45, 71–74]. The output beam of an external laser is injected into the unstable resonator, thereby exciting a multitude of cavity modes. The injection is rapidly switched-off, and the cavity will mould the transverse intra-cavity intensity distribution, whereupon that distribution is measured. A major issue that we have to contend with is the overall time-scale of this sequence of events, which is of order 20–25 ns for a realistic cavity configuration; this makes the experiment far from simple. Another important point to realize is that the transverse intensity profile should be measured at very well defined times in view of the fact that that profile is rapidly changing and dimming. We thus require a camera with a shutter time smaller than the cavity round-trip time.

In view of the foregoing, the experimental issues relate to three parts of the experiment:

1. the injection beam and the possibility to switch it off;
2. the unstable cavity itself;
3. the camera.

Although we will discuss these three components separately, we will see that the non-ideal behavior of one part imposes constraints on the other ones.

3.3. Estimating the parameters of the experiment

The fractality of the fundamental mode of an unstable resonator has, due to the necessary approximations, been theoretically proven in the limit of very large Fresnel number. Naturally, in an experimental verification of that fractality, one would like to use a cavity with a large collimated Fresnel number, N_{coll} , the variant of the Fresnel number relevant to the problem at hand. This is defined for the case of a confocal cavity as [5]:

$$N_{coll} = \frac{M^2}{M+1} N_F,$$

with M the magnification of the cavity and $N_F = a^2/\lambda L$ the conventional Fresnel number. Here a is the radius of the confining aperture, λ the optical wavelength, and L the mirror separation.

If only the collimated Fresnel number would have to be maximized, the roadmap for the experiment would be simple. The choice would be for a short cavity with reasonably large magnification M and large aperture. Note however that the magnification is linked to the round-trip losses by the relation:

$$P_n = \frac{P_{n-1}}{M^2}, \quad (3.1)$$

where P_n is the power of the mode during the n^{th} round-trip, and we assume a 3D cavity. Therefore, the total loss over n round-trips can get very large unless the magnification is of order 1, say between 1 and 2.

The cavity length L is connected to the cavity round-trip time τ_L by the simple relation:

$$\tau_L = \frac{2L}{c}, \quad (3.2)$$

so that the cavity round-trip time gets small when the mirror spacing is reduced. The experimental limit is set by the desire to distinguish, with the camera, successive round trips through the cavity. Given the minimum shutter time of the camera (≈ 2.5 ns), the cavity length should be $L > 37$ cm.

The camera imposes an additional constraint on the Fresnel number to be used since the amount of independent detail of the fractal image, or of any image for that matter, scales linearly with the Fresnel number (in each transverse dimension). Obviously, it does not make sense to create a fractal image whose detailed structure can not be recorded. Usually, CCD cameras have of the order of $10^3 \times 10^3$ pixels, the natural limit to the Fresnel number is of order 10^3 .

These considerations impose quite strict constraints on the design of the cavity, since we have

$$\begin{aligned} N_F &\leq 1000 ; \\ 1 &< M < 2 ; \\ L &> 0.37 \text{ m} ; \\ \lambda &\approx 1 \text{ } \mu\text{m} . \end{aligned}$$

In view of the fact that the magnification M is at most of order 2 we can, for the purpose of making estimates, ignore the differences between the various Fresnel numbers, and continue our discussion using the conventional Fresnel number (N_F).

An important quantity that we must estimate is the number of round-trips that is required to extinguish the higher-order modes so that only the fundamental mode remains. An approximate value of that number can be found by applying the geometric-optics model for an unstable-cavity as reported by Zemskov *et al* [75–77]. In that model the cavity's eigenmodes are the spherical waves predicted by geometrical optics and any modulation of their spherical wavefront is seen as a perturbation.

Let us assume, following this model, a wavefront perturbation which has a spatial extent equal to the minimum supported by the cavity:

$$d = \frac{a}{N_F},$$

3 Behold the darkness!

with a the size of the intracavity aperture and N_F the Fresnel number of the apertured cavity. Light within the resonator reaches the fundamental mode when the smallest possible perturbation has been filtered out. This happens when:

$$M^n d = a \Rightarrow M^n = N_F, \quad (3.3)$$

where n is the required number of round trips through the resonator. Let us assume a realistic cavity, of magnification $M = 2$, length $L = 50$ cm, containing an aperture of 5 mm radius, and illuminated by light at $\lambda = 800$ nm; these data lead to a Fresnel number $N_F \approx 62.5$. Equation (3.3) predicts then that the intracavity distribution is that of the fundamental mode after 6 round trips.

The relationship between number of round trips, magnification and Fresnel number that as given by Eq. (3.3) shows that the total loss incurred during the mode filtering is *independent* of the magnification. The power P_n that reaches the fundamental mode is related to the power originally injected into the cavity, by:

$$\frac{P_n}{P_1} = M^{-2n} = \frac{1}{N_F^2}, \quad (3.4)$$

For a cavity with parameters as stated above we have:

$$\frac{P_n}{P_1} \approx 2.5 \times 10^{-4}$$

Let us assume, for the moment, that the numbers just quoted are realistic. We can then estimate the number of photons that has to be injected into the cavity so that ultimately, a pattern with good (intensity) signal to noise, say 10, appears. We set the quantum efficiency of our detector to a realistic value of 0.2, and the transmissivity of the two cavity mirrors at 0.1. For a detector of 512×512 pixels we require as input to the front mirror of the cavity 5×10^{13} photons, corresponding to an energy of $\approx 10 \mu\text{J}$. In order to deliver such an amount of energy in a time of the order of the cavity round-trip time one requires a pulsed laser. Unless such a laser is available, the fractal pattern can not be recorded in a single shot but requires a protocol involving many thousands of τ_L exposures. Note that this problem gets more dramatic when the cavity's Fresnel number is chosen to be larger than the value assumed here ($N_F = 62.5$).

In an ideal experiment, the injected beam is switched-off instantaneously and fully, having thus an infinite extinction ratio; however, this is not the usual situation since phenomena such as relaxation oscillations may affect the laser shutdown. Light emitted after the laser is nominally off, i.e., afterglow, is then a major concern in our experiment. For instance, the discussion presented above seems to suggest that the extinction ratio of the injection laser should be of order 10^{-4} only; in that case, however, the afterglow from the laser, leaking through the unstable-cavity input mirror is of equal strength as that representing the fractal. Realistically, thus, the extinction ratio of the laser should be of order 10^{-6} or better.

The experimental problem at hand is a formidable one. We wish to "completely" switch-off a laser beam in a few ns, that is, we need to verify that after the switch we have roughly 6 orders of magnitude of lower intensity. This verification issue is the real challenge. To set the stage, the straightforward measurement of an intensity drop of 6 orders of magnitude in a

period of a couple of ns would minimally require a 20 bit A/D convertor at a clock speed of ≈ 500 MHz. Such convertors simply do not exist. For instance, oscilloscopes fall far from the 20 bit requirement, having at best 11 bits for digitalization.

3.4. In search of the ideal light source: fast modulation of a CW laser

In the simplest possible experimental configuration, light from a CW laser travels through an optical modulator towards the cavity. A change in the state of the modulator stops the flow of light, thereby starting the experiment. This approach has many advantages since modulators are stable, easily-controllable and fast. Actually, this approach is widely used in traditional cavity ring-down spectroscopy [72, 73]. We tested both electro-optical and acousto-optical modulators.

3.4.1. Electro-optical modulators as light switches

Electro-optical modulators (EOMs) employ the electro-optical effect to change the polarization state of a polarized light beam passing through them [6]. In essence, they are electrically tunable wave plates and, together with a polarizer, they can be used to open and close the flow of light.

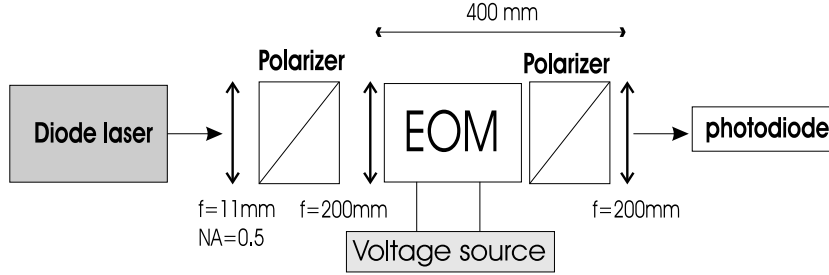


Figure 3.1: Experimental setup employed to test the modulation power of the electro-optic modulator (EOM) sandwiched between two polarizers.

Figure 3.1 shows our setup. Light from a laser diode (SHARP LM741), emitting at $\lambda = 785$ nm, is first fully polarized by a Glan polarizer, yielding a polarization ratio P_{\parallel}/P_{\perp} of 4000. The light then passes through a low-voltage electro-optic modulator (Gsänger LM0202) which has a half-wave voltage of 160 V at $\lambda = 488$ nm, and a specified extinction ratio of 250 at that wavelength. A second Glan polarizer prism acts as an analyzer of the polarization state of the light emerging from the modulator. The fact that the extinction ratio of this modulator is orders of magnitude smaller than what we aim for, is not necessarily a problem, since it may be possible to cascade a number of such modulators.

In the CW regime we measure an extinction ratio of 360, a value that looks quite promising since it implies that a cascade of just two modulators would be sufficient to yield 5 orders of magnitude of attenuation. However, our experiment requires pulsed operation of the

EOMs, and it is not known how well the EOMs will behave in that regime. Therefore we replaced the CW voltage source of the EOM by a Hewlett-Packard model 8116A pulse generator, with a pulse rise time of 6 ns, and pulse amplitude of 30 V.

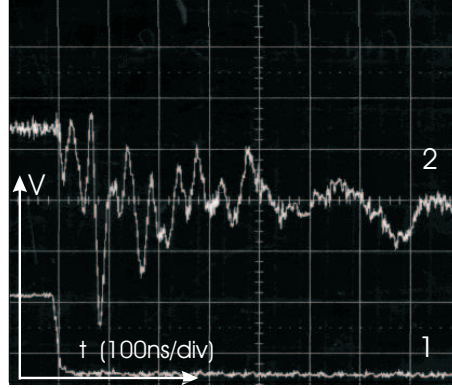


Figure 3.2: *Light intensity modulation produced by pulse modulation of an EOM. Curve 1 shows the time trace of the applied voltage, changing from -15 V to 15 V. Curve 2 shows the optical response of the EOM; its zero level is at the bottom of the scale.*

Figure 3.2 shows a typical result: the transmitted intensity fluctuates wildly over a time of $\approx 0.5 \mu\text{s}$. We attribute these fluctuations to a combination of piezo-electric and elasto-optic effects in the electro-optic crystal. We have also tested a Pockels cell modulator (Gsänger LM81). For this modulator we have found oscillations similar to those of Fig. 3.2. Because of the wildly fluctuating transmission when used in pulsed mode, these modulators can not be used in our experiment.

3.4.2. Acousto-optical modulators as light switches

In acousto-optical modulators (AOMs), a piezo-electrically excited propagating sound wave creates local variations in the density of a crystal. Thereby inducing a spatial periodical modulation of its refractive index, which effectively acts as a grating. Light falling on an AOM is thus diffracted as in Bragg scattering. The modulation is caused by the fact that the diffraction mechanism can be switched on and off simply by launching the acoustical wave, or not. In the latter case the quantity of energy that is scattered into a diffracted order is negligible.

We first measure the extinction ratio of the diffracted beam when the AOM is operated in the CW regime. Figure 3.3 shows the setup; we use a He-Ne laser and a modulator (ISOMET, model 1206) containing a Lead Molybdate crystal with an acoustic velocity equal to $3.63 \text{ mm}/\mu\text{s}$. The modulator is controlled by a driver with a center frequency of 80 MHz, and a rise time of 5 ns. We measured the transmitted zeroth and first order beams by means of large-area photodiodes; we were very pleased to find that the extinction of the first-order diffracted beam is more than 7 orders of magnitude.

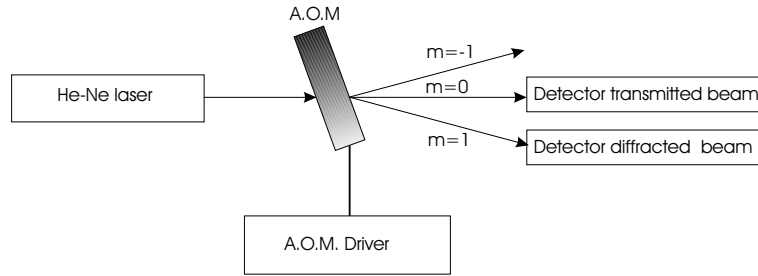


Figure 3.3: Schematic diagram of an experiment to find the CW modulation depth of an acousto-optical modulator.

However, as in the case of the EOM, it is the pulsed regime that counts. The duration of the switch-off process is in principle determined by the time that the sound wave needs to travel across the width of the optical beam. Two contradictory requirements must be fulfilled in order to achieve fast and deep modulation. Fast modulation requires a small transit time of the acoustic wave through the optical beam, i.e., a small spot size of the laser beam, while one needs a large spot size to obtain many acoustic wavelengths, i.e., a high diffraction efficiency.

We chose for speed over efficiency. Figure 3.4 shows our setup, where a $f = 100$ mm lens focuses the beam in the center of the acousto-optical modulator. We optimize the switch-off time by longitudinally translating the modulator around the beam's focus. The diffracted beam is captured by a $f = 70$ mm lens and focussed on a fast photodetector. A pulse generator (HP 8116A) generates a train of square pulses that digitally modulates the AOM's RF driver.

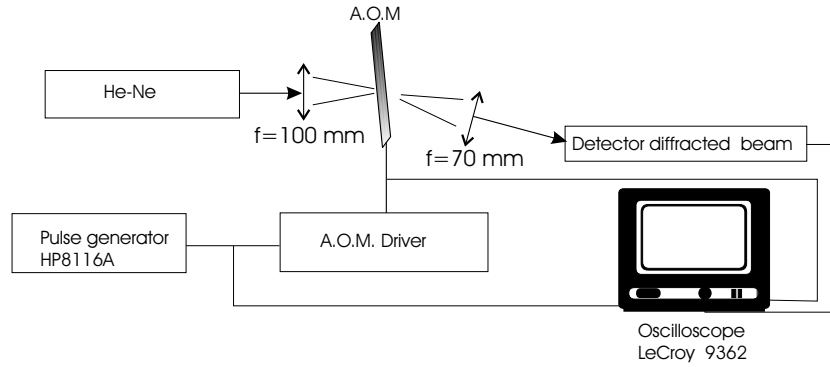


Figure 3.4: Schematic diagram of the experiment to find the dynamic modulation characteristics of an acousto-optical modulator.

Our best results are shown in Fig. 3.5. They correspond to the case where the laser is focused in the center of the modulator. It can be seen that the detector signal has a fast component, that decays in around 25 ns, and a slow part whose trace can be detected even 50 ns after the trigger pulse. The fast decay covers only a single decade; its speed is determined by the time it takes the acoustic wave to travel across the laser beam. From this measurement

we calculate that the diameter of the effective interaction cross-section between the light and the acoustic grating is of the order of $90\text{ }\mu\text{m}$. This number is consistent with the estimated spot diameter of $100\text{ }\mu\text{m}$, that follows from the values of the focal distance of the in-coupling lens, the optical wavelength, and the radius of around 1.5 mm of the laser beam.

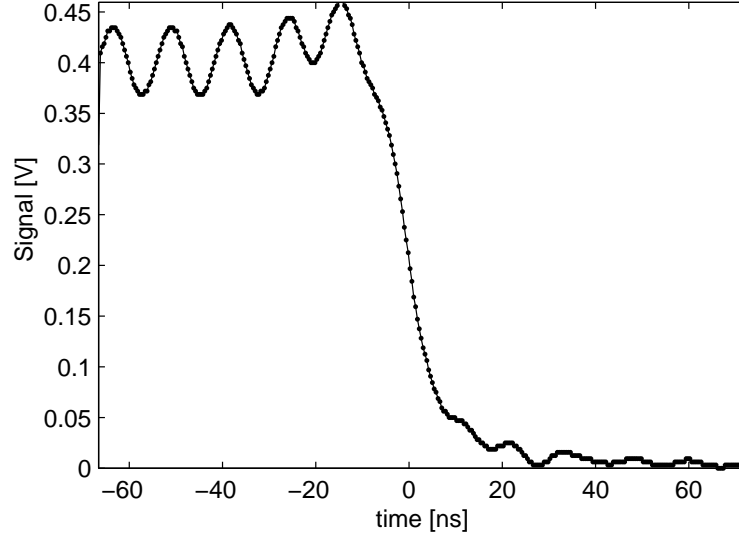


Figure 3.5: *Signal monitored by the detector in the diffracted beam, for the case that the decay time of the light is minimal.*

We believe that the slow component of the decay comes from the ineffective damping of the acoustic energy in the crystal [78]. Once the acoustic wave has been nominally shutdown the modulator behaves as a scatterer of acoustic energy, until, as a consequence of the crystal's intrinsic damping, that scattered acoustic energy is converted into heat. This process is slow on the time scale of our planned experiment.

Interestingly, before the decay starts the diffracted power shows a well developed amplitude modulation. We believe that the origin of this phenomenon lies in the small effective area of interaction between the light and the acoustic grating. In fact, the combination of sound speed in the crystal, and modulation frequency of the RF driver, yields a wavelength of $45\text{ }\mu\text{m}$ for the acoustic wave. A comparison with the inferred beam diameter yields that on average only 2 grating lines are contributing to the diffracted beam. Consequently, we expect that the diffraction efficiency is modulated with the acoustical period. A confirmation of this hypothesis comes from the measured period of the amplitude modulation, 12.5 ns , just the period of the acoustical wave.

The results reported here suggest that a single acousto-optic modulator will not provide the modulation depth our experiment requires. This conclusion is based on our belief that the double tail decay process is universal to all devices of this kind.

3.5. Afterglow of pulsed lasers

The use of pulsed lasers, instead of modulated CW sources, has several advantages. First and foremost, the energy per pulse is usually much higher than what can be achieved by using CW lasers. Additionally, if the duration of the laser pulse is shorter than the round-trip time of the unstable resonator, and therefore, as a result of our cavity's design, shorter than the exposure time of our camera, then all of that energy can be captured in a single camera exposure; moreover, the underlying mechanisms of laser pulse formation suggest that the afterglow emission may be very weak.

We will evaluate the performance of two types of pulsed lasers: a microchip Q-switched laser, and a regeneratively amplified mode-locked laser.

3.5.1. Afterglow of a sub-nanosecond passively Q-switched microchip laser

Our light source is a JDS Nanogreen laser [79]. This compact device uses a laser diode to pump a $750\text{ }\mu\text{m}$ thick ($\text{Nd}^{3+}:\text{YAG}$) crystal that is glued to a $60\text{ }\mu\text{m}$ thin layer of ($\text{Cr}^{4+}:\text{YAG}$), which acts as saturable absorber, i.e., as a passive Q-switch. A pulse is initiated once the optical energy density inside the gain medium has reached the threshold of the saturable absorber. The output of this laser passes through a KTP crystal that doubles its frequency to 532 nm . The output consist of $\approx 520\text{ ps}$ long laser pulses at a repetition rate of $\approx 30\text{ KHz}$.

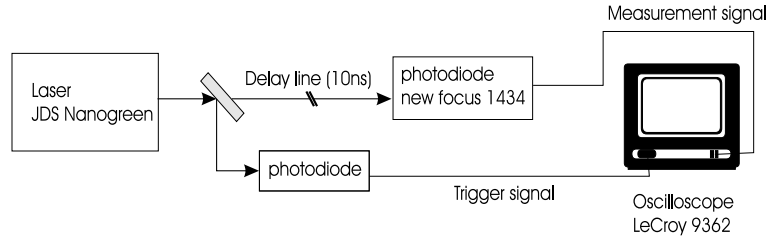


Figure 3.6: Diagram of the experiment to measure the pulsed output of a μ -chip Q-switched laser.

One inherent problem of passive Q-switching is the lack of control over the instant of laser emission. This implies that in an experimental setup (see Fig. 3.6) the laser must become the master clock. In the experiment we split the laser beam in two by means of a beamsplitter. The pick-off beam is sent to a photodiode whose output triggers a fast oscilloscope. The main beam is sent to a 3 meter long delay line, at the end of which a fiber-coupled ultrafast photodiode picks up the signal. The time trace is recorded on the oscilloscope.

Figure 3.7 shows the trace recorded on the oscilloscope, revealing the existence of two additional pulses whose intensities are roughly 300 and 3000 times weaker than that of the main peak. We attribute these afterpulses to relaxation oscillations of the laser.

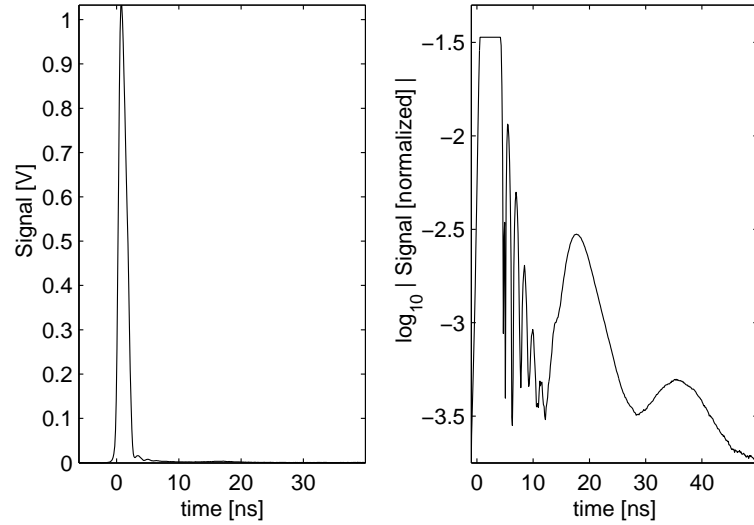


Figure 3.7: Trace of the power output registered by a fast photo-detector (New Focus model 1434). The left picture show the laser pulse on a linear scale, while, on the right, the normalized pulse is displayed on a logarithmic scale to bring forward its late time behavior.

It is clear that this laser is not suitable for our purposes since its power output exhibits a complicated structure on intensity and time scales that are not in accordance with our planned experiment.

3.5.2. Afterglow of a regeneratively amplified mode-locked laser

Mode-locking is another technique commonly used to generate short laser pulses. In this technique many longitudinal modes of the laser cavity are allowed to coexist, but are forced to have a fixed phase relation; as a result, the laser repetitively emits light spikes. This technique is broadly used to generate ps or fs light pulses.

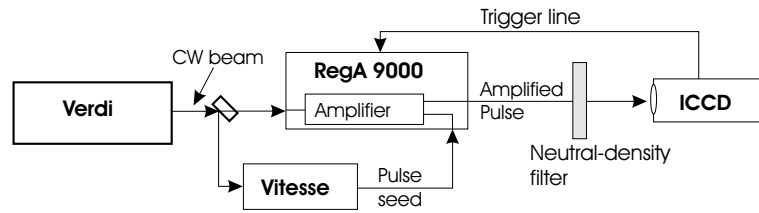


Figure 3.8: Schematic of the setup to measure the afterglow of a fs pulse laser system.

We characterized the light output from a regenerative amplified mode-locked Titanium:Sapphire laser, see Fig. 3.8; the regenerative amplifier was a Coherent RegA 9000 . This system produces 160 fs long pulses, at a wavelength centered around 810 nm; its maximum repetition

rate is 100 kHz, while the typical energy per pulse is 3 μJ . The regenerative amplifier is pumped by a CW laser (Coherent Verdi), and requires a pulse seed. This comes from a CW mode-locked laser (Coherent Vitesse), that is pumped by the same laser as the regenerative amplifier.

We use an ICCD camera with spatial integration as measuring device. This is convenient since that camera has a minimum exposure time of 2.5 ns (FWHM). The idea is to use the camera as trigger for the laser, and scan the trigger delay. Figure 3.9 shows our experimental results. The main pulse is followed after ≈ 15 ns, by a secondary pulse that is four orders of magnitude weaker. The presence of this after-pulse is the result of non-ideal behavior of the cavity dumper in the regenerative amplifier. Approximately 20 ns after the main pulse the light level is reduced by seven orders of magnitude. Then a train of pulses appears, with a period of 11 ns. This train represents an echo of the pulse train emitted by the seed laser, reflected off some intra-amplifier optics. Note that despite the fact that the light pulses supposedly have a length of around 160 fs, the output of the gated ICCD camera shows pulses of a few ns. This is a consequence of the finite response time of the ICCD.

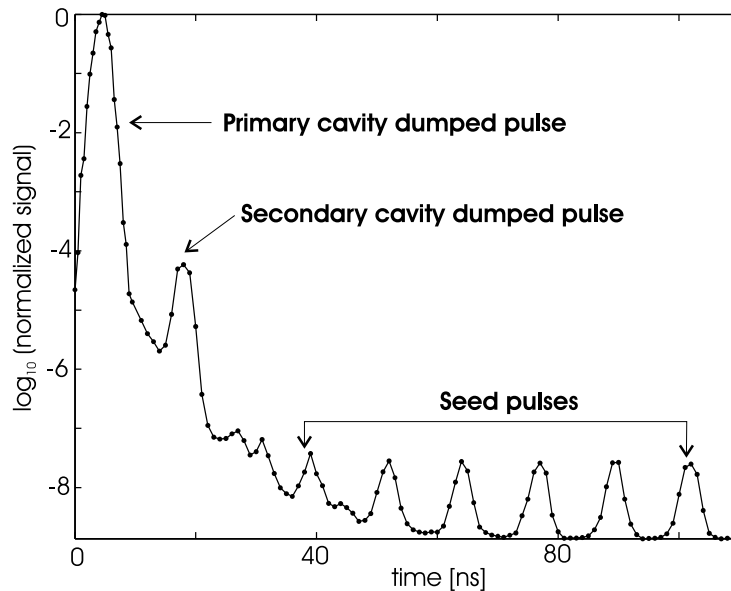


Figure 3.9: Light emission from a RegA 9000 fs laser system, as recorded with an ICCD camera with a temporal resolution of 2.5 ns. The results follows from joining two sets of measurements, taken with different neutral density filters.

The results of Fig. 3.9 show that the regenerative amplifier cannot be used directly in the planned experiment, unless an additional technique is devised to selectively extinguish the first afterpulse, without affecting the main pulse.

3.6. Could a semiconductor laser diode be the solution to our problem?

The idea of using a semiconductor diode laser to solve the issue at hand is based on the following considerations:

1. Semiconductor diode lasers have a small cavity volume and consequently the intra-cavity photon lifetime is very short (of the order of 10 ps). A direct consequence is that their relaxation-oscillation frequency lies in the 1-10 GHz range, which indicates that sub-ns switching speeds are possible [80].
2. Semiconductor lasers can be easily amplitude modulated at high speeds, just by modulating the injection current between values far below and far above threshold [80].
3. The spontaneous-emission radiation emitted by the active medium during the off state can be suppressed by applying a reverse bias to the diode's junction¹.

We therefore intend to drive the laser by means of positive current pulses superimposed on a negative voltage bias. We aim to create a high power pulse, while most of the time the laser is off.

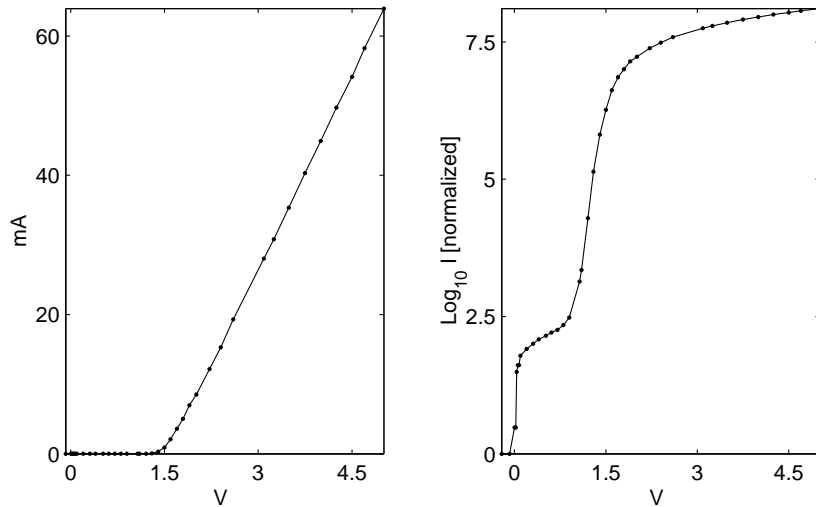


Figure 3.10: Current-voltage characteristic of a semiconductor laser diode (Sharp LM024MD0); on the left, plotted on a linear scale, and, on the right, on a logarithmic scale. The diode was connected in series with a resistor of 50 Ω . We measure the potential drop across the diode and the current through the circuit.

¹It has been shown [81–83] that the lifetime of carriers trapped on both sides of a diode's junction can be reduced by applying a bias across the junction. One typically observes that the carrier lifetime is smaller than 500 ps when a negative bias of 4 V is applied.

The characterization of the semiconductor diode laser follows a similar path to that of optical modulators. First we test and optimize the setup in the CW regime; this is necessary because the unavailability of a "real-time" detection system with a sufficiently large dynamical range makes the latter task impossible in the pulsed regime. Once this step is completed, we proceed to obtain data on its pulsed behavior.

Two curves summarize the behavior of a diode laser in the CW regime: the relation between the injection current I and the voltage V across the p-n junction, and its optical power output as a function of the injection current.

Measurement of the I-V curve is straightforward, we want to identify the threshold of the diode's conduction, as well as the order of magnitude of the current that flows when the diode is nominally non-conducting. The results are shown in Fig. 3.10, revealing that the impedance of the diode changes at 1.5V; it also shows that, in the high impedance regime (below 1.5V), the diode still conducts slightly, the current being of the order of 10^{-7} A. From the figure we conclude that the diode has an effective resistance of 4.8Ω in the low-impedance regime, and of $10 \text{ M}\Omega$ in the high impedance one.

The optical output as a function of the voltage (Fig. 3.11) shows two sharp transitions. The first transition accompanies the change of the diode's impedance, whereas the second transition signals the start of the lasing process. An analysis based on rate equations [5] shows that the latter transition has the potential to yield an extinction ratio of 5 orders of magnitude, if we manage to isolate the light emitted by the single lasing mode from the spontaneous emission light emitted by the device below threshold.

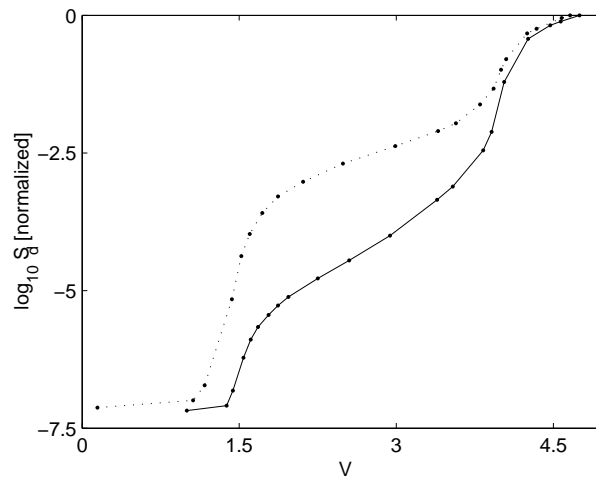


Figure 3.11: Normalized power output of the diode laser vs forward voltage across the junction. The solid line corresponds to the filtered light, with the monochromator set for a 0.3 nm linewidth (100 μm input and output slits); the dotted line corresponds to the total (i.e. non-filtered) laser output.



Figure 3.12: Diagram of the experiment to measure the attenuation depth and switching speed of a diode laser. The central element is an Ebert-type monochromator ($f = 250$ mm, $f/3.5$, with a 1180 g/mm grating, blazed at 700 nm), with 100 μm input and output slits. It filters, both spatially and spectrally, the light produced by a Sharp LM024MD0 laser diode. Light was in- and out-coupled to the monochromator by means of a pair of $f = 50$ mm antireflection coated lenses. We measured the output in the CW regime by means of a large-area photodiode, in the pulsed regime we use single-photon sensitive detectors.

We use an Ebert-type monochromator for spectrally filtering and spatially isolating (by means of the narrow input slit) a narrow band of the light emitted by the laser diode (see Fig. 3.12); this setup allows us to resolve wavelength differences of 0.33 nm at $\lambda = 800$ nm, and has a transmission efficiency of 12%.

Figure 3.11 shows our results. We choose to present the power output as a function of the voltage across the juncture, instead of the more familiar representation of power output vs injected current. The reason for this choice is to stress that the amount of light emitted by the laser in the high impedance regime is tiny, but significant.

A look at the total power emitted (dotted line) reveals a contrast of at least 7 orders of magnitude in this CW experiment. We do not know the exact value for the contrast when using spectrally and spatially filtered light (solid line), since for that case, the signal in the high impedance regime is below the sensitivity limit of our detector. In any case, a comparison of both curves for applied voltages between 1.5V and 5V shows that at least 2 orders of magnitude are gained by means of spectral and spatial filtering.

The numbers for the CW regime look sufficiently good to go ahead with the characterization of the pulsed regime.

3.7. Afterglow of a pulse-driven semiconductor diode laser

We would like to know whether a pulse-driven semiconductor laser, whose light is filtered by a monochromator, maintains the behavior seen in the CW regime. A positive answer implies that a semiconductor diode laser would be the light source of choice for our experiment.

Our pulsed setup is identical to that of Fig. 3.12. We replace the DC current source by a pulse generator (HP 8116a), which generates pulses of maximum 8V, while the minimum negative bias is -8 V, and a shortest pulse duration of 10 ns (6 ns rise time). The beam path connects the monochromator with a suitable single-photon sensitive device; we use either a multichannel plate photomultiplier or an ICCD camera.

3.7.1. Detection by means of time-correlated single-photon counting

An interesting possibility for probing the on/off ratio of our diode laser is offered by time-correlated single photon counting (TCSPC), as used in, for instance, fluorescence-lifetime measurements. This method has sub-nanosecond resolution and accumulates data points in a digital register.

In essence, by TCSPC, one reconstructs the time evolution of the emitted light pulse by registering the arrival time of individual photons. Thus, when we assume that the light pulse from our source cuts off very rapidly, with an infinite on/off ratio, a TCSPC with a 16-bit register will generate a record of that pulse with a sub-nanosecond resolution and an on/off ratio of 2^{16} . It is possible to accumulate many of those records to increase the dynamical range of the measurement.

Our photon-counting module (Becker & Hickl SPC-330) has a 16-bits register, and a maximum time resolution of 6 ps. The experimental time resolution, however, is limited by the jitter of the single-photon sensitive detector. We used a multichannel plate photomultiplier (Hamamatsu R3809U), that has a transit time spread of 45 ps. This combination of photomultiplier and photon-counting module provides a 16-bit dynamic range with a 45 ps time resolution.

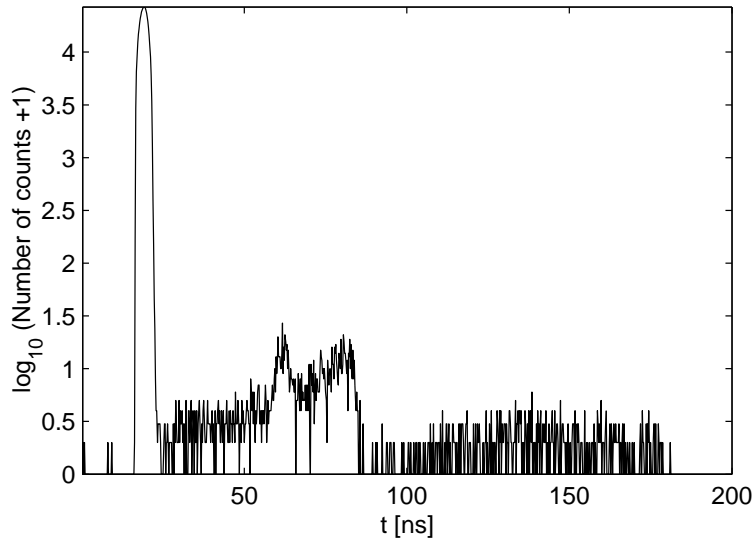


Figure 3.13: Typical photon counting trace. We drive the laser by 10 ns long pulses, with an amplitude of 9 V over a permanent bias of -1 V. The bandwidth of the monochromator is equal to 0.3 nm.

The results are disappointing. Figure 3.13 shows a typical experimental trace. Not only are there some additional low-intensity peaks after the main pulse, but the detector also seems to indicate that the laser never stops emitting. Whatever we did, this particular behavior proved to be persistent; therefore we conclude that it is caused by the detection system, and not by the light source.

We think that both the secondary peaks and the background, are essentially artifacts that originate from the ionization of helium atoms inside the photomultiplier. These atoms can permeate from the atmosphere into the evacuated volume of the multichannel plate, probably through its glass window [84]. During each pulse, there is a probability that the accelerated electrons (≈ 3.4 kV) ionize some of these He atoms; the resulting ions are then accelerated in the opposite direction, and generate secondary electrons after collision with the photomultiplier's amplification stages. These electrons arrive to the detector's electrode after certain delay. Therefore we interpret the secondary peaks as ionic "echoes" of the main electronic peak.

3.7.2. Using an ICCD camera

Alternatively, we can use an ICCD camera to study the temporal profile of the emission by the pulsed semiconductor laser, just as it was done for the mode-locked laser. An ICCD contains a MCP just as the photomultiplier employed with the TCSPC technique and is therefore open to similarly suffer from electron-impact ionization. This is not the case however, because our ICCD includes a 4th generation MCP. Obviously the time resolution of the ICCD is lower than that of a TCSPC module, but this is not a problem since we only require a time resolution as big as the unstable-cavity round-trip time, which by design, is equal to the ICCD minimum exposure time. An advantage of an ICCD device is the possibility of integrating the signal over many pixels, effectively extending the dynamic range of the device far beyond the level of its A/D convertor.

We have used an ICCD camera previously, in the characterization of the mode-locked laser. There the laser spot was concentrated in a small region, and the maximum signal of each image was taken as the criterion to compare the signal in consecutive frames. The present experiment differs from that one in that, while the output beam of the mode-locked laser was virtually aberration free, the beam emitted by our semiconductor diode laser is aberrated (this applies to most semiconductor diode lasers). Even worse: since our beam travels through a monochromator the natural astigmatism of the output beam is greatly enhanced. The implication is that the spot size on the camera is substantial.

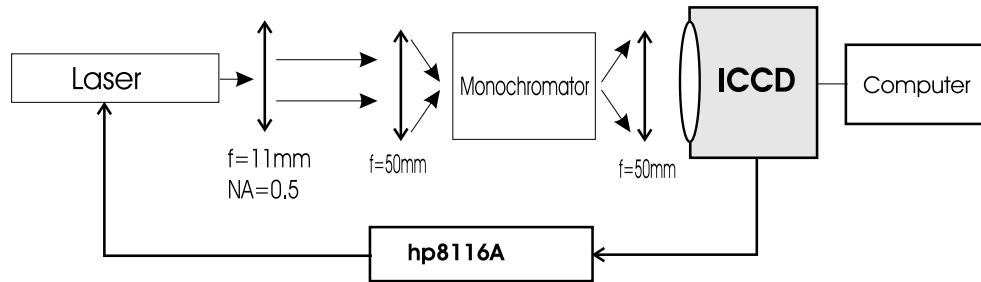


Figure 3.14: Setup to characterize the trace of a pulse-driven negative bias diode by means of an ICCD (Roper Scientific PI-MAX)

Figure 3.14 shows our setup; we image the output slit of the monochromator on the photocathode of the camera. The output of this experiment comes in the form of a sequence

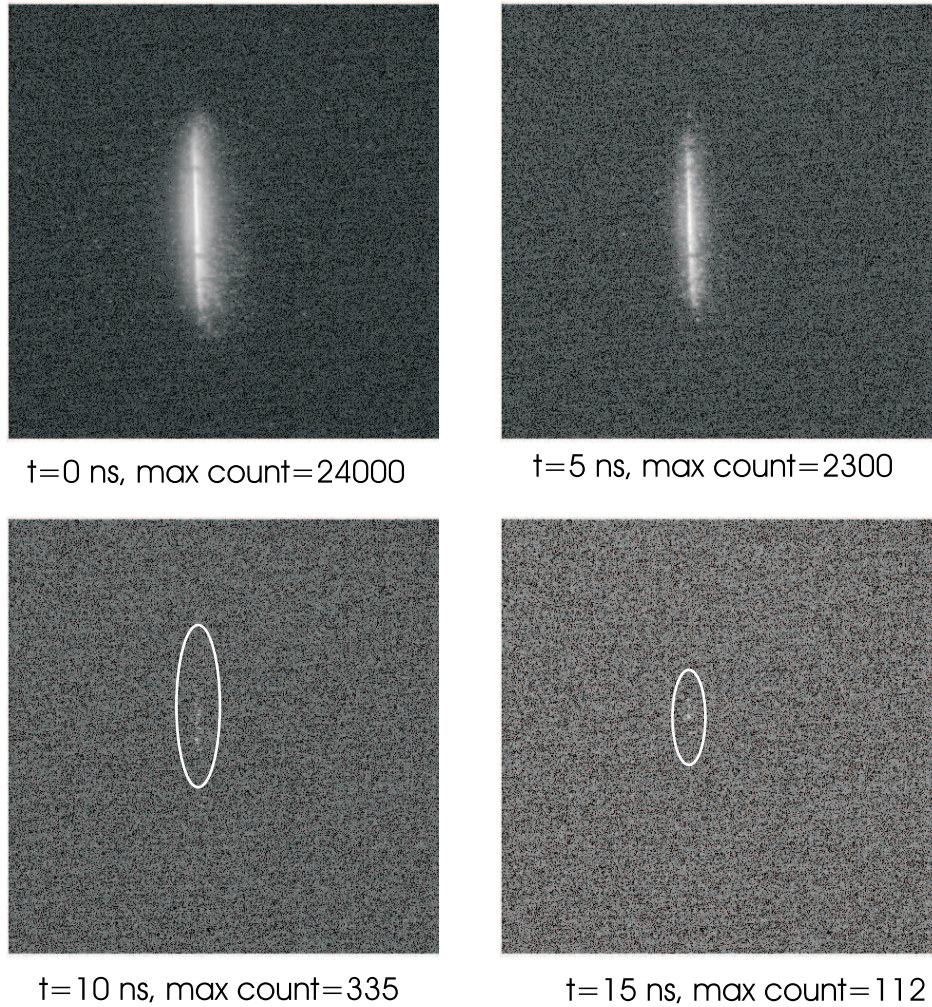


Figure 3.15: Typical sequence of pictures obtained during the study of the temporal behavior of a diode laser, all shown on a logarithmic scale, with black representing the minimum number of counts, defined to be 1, while white corresponds to the maximum count level. Each shot defines its own gray scale. Our detector has 512×512 pixels, and each pixel is digitized by a 16 bit A/D convertor. The ellipses show the regions where there are still some photons detected.

of bitmaps, each bitmap containing the number of photons that has reached the camera in an exposure.

Figure 3.15 shows a typical sequence of images, taken around the moment when the decay starts. The rapid decay is evident, the maximum number of counts per pixel decreases by a factor of 200 in 15 ns. This sequence also shows that, late in the decay, the signal-to-noise level is very low. Nevertheless, as we show next, by carefully analyzing the histogram of the signal level it is possible to discriminate the signal from the background.

Discriminating signal from background in an ICCD image

In order to extract the number of photons present in an ICCD image, like those of Fig. 3.15, one first needs to distinguish pixels that have been activated by one (or more) signal photons from pixels that have been activated otherwise ("background"); this is done by comparing the charge count value of each pixel against a reference threshold. The value of those pixels that satisfy the threshold condition is then integrated. To define this threshold we first determine the histogram of pixel counts, i.e., we determine how many pixels contain a specified number of counts.

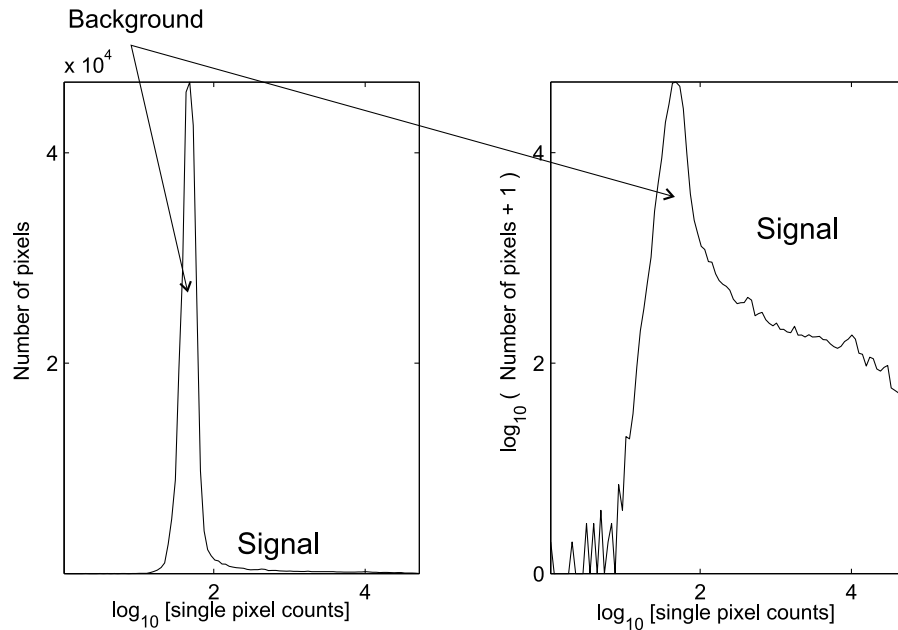


Figure 3.16: Histogram of pixels counts for the highest signal-to-noise image shown in Fig. 3.15. Left plot: vertical scale is linear; right plot: vertical scale is logarithmic.

Figure 3.16 shows the histogram of pixel counts of the first image in Fig. 3.15 (the one with the highest signal to noise). In that image only a small fraction of the pixels contains the signal, so the dominant feature of the histogram corresponds to the background level of the CCD. The background pixels are typically concentrated in a narrow peak. In contrast,

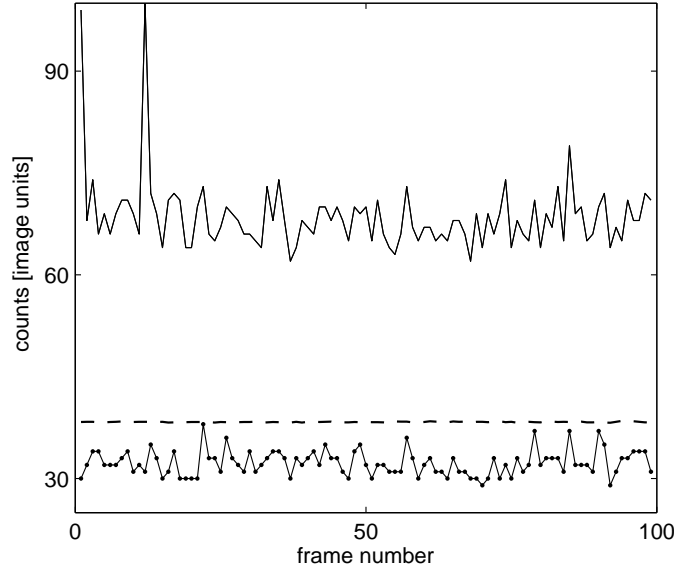


Figure 3.17: Comparison of counts per image, of a series of 100 dark images. Solid line: highest count value per image. Solid line with dots: Median $Z(k)$ of the number of counts per image. Dashed line: $8D_{abs}(k)$.

the pixels that contain the signal are spread over a broad region in the histogram, with, in general, a small probability. Generally, the peak and tail of the histogram are connected rather smoothly. This implies that no simple tool is available for separating what is background and what is signal.

If the signal level is high, as in the upper row of images of Fig. 3.15, one can safely set the threshold at a relatively high value. The reason is that the integrated contribution of those pixels that contain signal at a level below the chosen threshold, is very small with respect to that of the pixels that have a signal level above that threshold. However, if the signal level is low, as in lower row of images in Fig. 3.15, the effect of a high threshold setting may be to eliminate the signal altogether. In an experiment like ours, it is necessary to set the threshold level at the lowest possible value.

Naively, one would think that one could employ a single threshold level for all images of a decay sequence. This approach yields good results when the statistical properties of the background do not change significantly from frame to frame. To test whether that approach applies to our experiment we have taken 100 dark images, i.e., images where no light impinges on the camera, one after the other. Figure 3.17 shows the highest count value of a series of consecutive frames. The fluctuations seem to be quite substantial making the present approach inadequate. What one needs to solve the problem at hand is to define a *per-image* background threshold.

In the context of defining this threshold it is, however, not very useful to investigate the fluctuations in the highest count number per dark image, since that number always provides an overestimate of the threshold. Moreover, in a signal-containing image this method fails completely because, in that case, the maximum number of counts represents part of the signal one wants to measure.

It is much more relevant to consider the distribution of dark levels, i.e., the histogram of pixel counts. From that histogram one can determine the median value $Z(k)$ of pixel counts of an image k , and its dispersion:

$$D_{abs}(k) = \frac{1}{N} \sum_{i,j=1}^N |k(i,j) - Z(k)| \quad (3.5)$$

where N is the linear dimension of the CCD array, and $k(i,j)$ is the signal of the image k at the coordinates (i,j) of the array.

If one considers a series of dark images one finds, for each frame k , a value of the median $Z(k)$ and of its dispersion $D_{abs}(k)$. These values have been included in Fig. 3.17. While the dispersion is very constant for this set of images (this is not always the case), the median of dark counts is seen to vary (its range being equal to 9 units), though less than the maximum counts per image (range equal to 25 units).

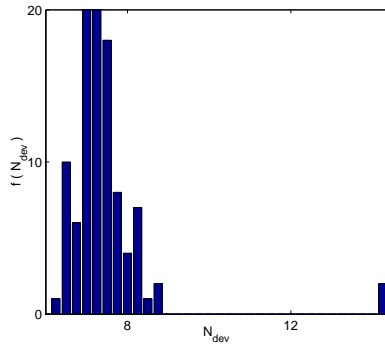


Figure 3.18: Histogram of maximum number of counts per image in a series of dark images, expressed in terms of N_{dev} .

One can now construct another histogram by normalizing the deviation of $\max(k)$ from $Z(k)$ by the dispersion:

$$N_{dev} = \frac{\max(k) - Z(k)}{D_{abs}(k)} \quad (3.6)$$

The histogram of normalized difference is shown in Fig. 3.18; it shows that the maximum dark count level is typically larger than the median of the distribution by 8 units of dispersion.

We now use this result to analyze images that do contain a signal. In that case the histogram of pixel values has a considerable tail. However, because the peak due to the background is so pronounced, it is still possible, using an algorithm as described in appendix C, to accurately determine the median and dispersion of the background pixels.

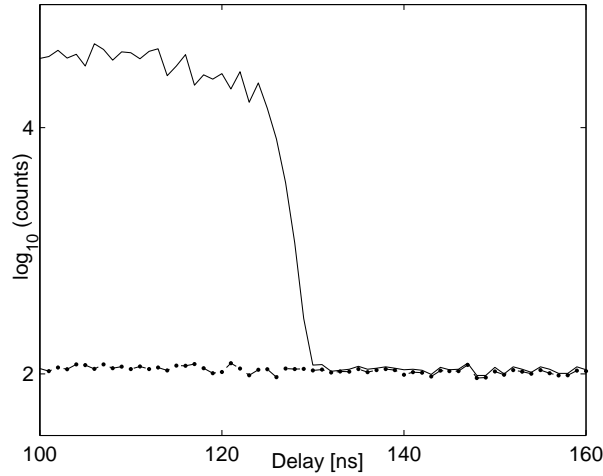


Figure 3.19: Results produced by our algorithm. Solid line: maximum pixel counts per image. Dotted line: Background threshold predicted by our algorithm.

The effectiveness of our algorithm is demonstrated in Fig. 3.19. We see the maximum number of counts together with the extracted background threshold of a series of images taken during the switch-off of the diode laser. After the decay, the background threshold (dotted line) follows rather closely the maximum number of counts of each image, meaning that our algorithm classifies all pixels as background. At high illumination ($t < 130$ ns), the per-image threshold level provided by our algorithm, is independent of the light intensity that reaches the camera, as it should.

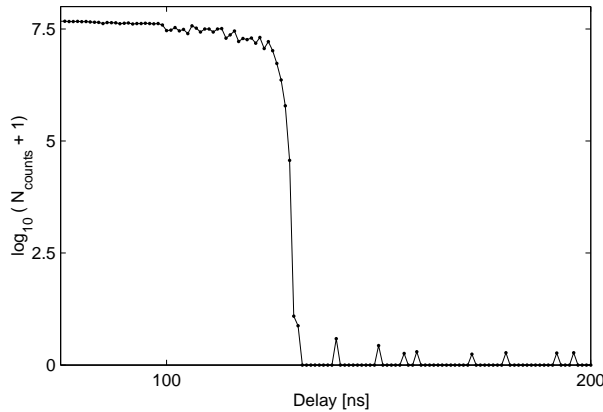


Figure 3.20: Afterglow of a pulse-driven negatively biased semiconductor laser diode whose light is filtered by a monochromator, as observed with an ICCD camera. The small peaks after the main decay are not the result of photons impinging on the camera but of small errors in the threshold procedure.

Application of this per-image background threshold, and integrating over the remaining, signal pixels, yields the results shown in Fig. 3.20. It is the time trace of the total intensity impinging on the camera, and shows that effectively extremely few photons arrive at the camera after the laser has been shut down. Moreover, it verifies that ICCD cameras can be used to study the afterglow of laser systems over ranges extending 7.5 orders of magnitude.

3.8. Conclusion

After careful consideration of many alternatives, we have come to the conclusion that a negatively biased, pulse driven semiconductor diode laser, whose light is spatially and spectrally filtered by a monochromator, is the ideal light source for our cavity ring-down experiment, when used in combination with an ICCD camera as a detector.

Chapter 4

Towards a fractal pattern

4.1. Introduction

As shown in the previous chapter, a negatively-biased pulse-driven semiconductor diode laser, together with a monochromator as its spatial and spectral filter, provides an adequate light source for our cavity ring-down experiment. In the present chapter we will apply the cavity ring-down method to study the evolution of the intracavity intensity distribution in several unstable resonators. We will use an ICCD camera to take snapshots of that distribution in a single transverse intracavity plane (defined by the cavity aperture), at different stages of the decay. We will see that this is not an easy task, in particular because of the scarcity of light in our experiment at the time the results become interesting. This is a consequence of the lossy nature of unstable resonators. We will analyze the intensity distribution in search of fractality to compare the results with the analytical theory by Berry *et al* [29, 30]. The influence of noise on the fractal pattern will be discussed in detail in the chapter 5.

4.2. Experimental method

Our experimental method has been described in detail in Chapter 3. Basically, we inject a laser beam into the unstable resonator, interrupt it in a time of the order of the cavity round-trip time, and study the ensuing intracavity distribution by observing the light that is transmitted through the cavity's output mirror (see Fig. 4.1). In that chapter we also gave estimates of key parameters of our experimental setup, enabling us to observe the predicted fractal pattern. These are:

$$\begin{aligned} N_{\text{coll}} &\leq 1000; \\ L &> 0.37 \text{ m}; \\ \lambda &\approx 1 \text{ }\mu\text{m}; \\ 1 &< M < 2. \end{aligned}$$

Here L is the cavity length, M the round-trip magnification, λ the wavelength of the input laser beam, and N_{coll} the collimated Fresnel number. The latter, defined for the case

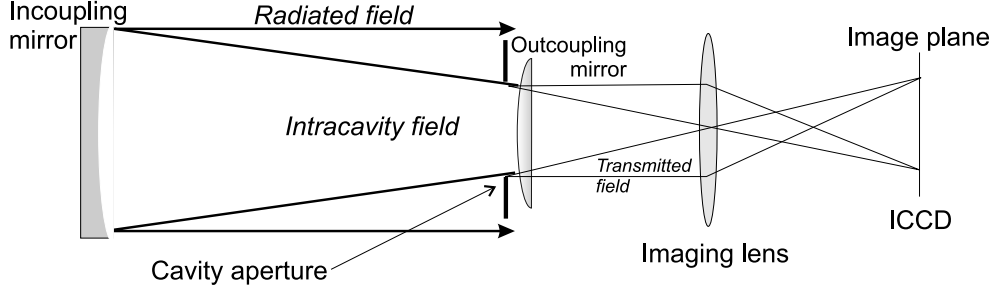


Figure 4.1: Radiated and intracavity fields of an unstable resonator. We use a lens to image the intensity distribution inside the intracavity aperture on the camera.

of a confocal resonator as $N_{\text{coll}} = \frac{M^2}{M+1} N_F$, with N_F the traditional Fresnel number of the resonator, determines the spatial dynamic range of the fractal under study¹. The limited power of our spectrally and spatially filtered diode laser beam implies that the experiment can not be performed on a single-pulse basis. Instead, we will accumulate, on-chip in the ICCD camera, many exposures at a given time delay.

4.2.1. Experimental setup

Figure 4.2 shows our setup. The output beam from a single-mode diode laser² is collimated by a $f=8$ mm, $\text{NA} = 0.5$ aspheric lens. Subsequently, it traverses a $4\times$ anamorphic prism pair to reduce its astigmatism. It is then aperture matched by a pair of $f = 160$ mm lenses to an Ebert monochromator ($f = 250$ mm, $f/3.5$, with a 1180 g/mm grating, blazed at 700 nm), whose input and output slits are 100 μm wide each.

The beam coming out of the monochromator is sent towards the unstable resonator. The latter is composed of a concave spherical input mirror, having a radius of curvature of 10 m, and a convex output mirror, separated by a distance of 50 cm. The convex output mirror with an effective radius of curvature of 4 m is a reverse-mounted concave mirror with 6 m radius of curvature. The diameter of both mirrors equals 25 mm. This arrangement yields a non-confocal resonator, with a magnification $M \approx 1.6$, and Fresnel number $N_F = 390$. Both mirrors have coefficients of reflectivity equal to $R = 0.9$ at $\lambda = 810$ nm and are anti-reflection coated on their flat surface. The object plane is defined by positioning a diffractive aperture, with a size typically in the range $1 - 12$ mm, inside the cavity approximately 1 cm in front of the output mirror.

We use a $f = 200$ mm lens to image the intracavity intensity distribution on the ICCD camera. Alternatively, the output beam can be directed to a fast photodiode, for alignment purposes.

¹Note that for values of the round-trip magnification between 1.5 and 2 , N_{coll} and N_F have very similar values; therefore, it is possible to indiscriminately use these quantities to parametrize the cavity.

²For this experiment we use a Sharp LD024MD0 semiconductor diode laser, at $\lambda = 785$ nm

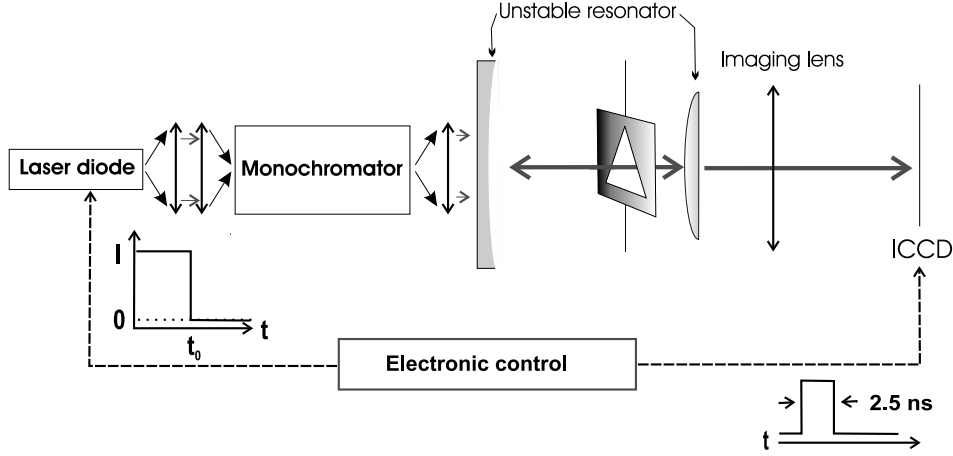


Figure 4.2: Schematic of the unstable-resonator cavity ring-down experiment. The left part sketches the light source, the center part is the resonator with a triangular aperture positioned inside, while at the right, one sees the lens that creates an 1:1 image of the aperture on the photocathode of the ICCD camera.

4.2.2. Aligning the cavity

We aligned the cavity with respect to the input beam by using it as an optical spectrum analyzer. When aligning a high-finesse optical cavity, one either sweeps the cavity length or the frequency of the input beam. One then monitors, with the help of a photodiode mounted behind the cavity, the signal transmitted by the cavity. For a stable resonator, one adjusts the cavity parameters until the transmitted signal contains just a few, very sharp peaks. Usually this involves a form of mode matching of the input beam to the stable resonator modes of that type of cavity. In the present case this approach can not be followed because the transmission spectrum of our unstable resonator consists of very broad peaks, a consequence of the very low effective finesse of the cavity ($\mathcal{F} \approx 4.5$). Additionally, there is no way to mode match to a single transverse cavity mode since all transverse modes are aperture filling. However, the modulation depth of the transmission spectrum of the unstable resonator still provides a handle on the alignment of the resonator.

In the experiment we monitor this by observing the power transmitted by the cavity, while the input beam is being pulsed by driving the diode laser above threshold for a few hundred ns. Figure 4.3 shows the trace of the signal picked up by a fast photodiode mounted behind the cavity. One sees both the rising and falling edges of the light pulse injected into the cavity. Additionally, one observes a steadily increasing noise-like component which is very sensitive to the alignment of the cavity. We checked that this noise-like component is not present in the intensity of the optical signal injected into the cavity, and is therefore not the result of optical feedback into the laser diode. This noisy component in the transmitted signal appears because the frequency of the injection laser is chirped, a consequence of the fact that the laser operates in pulsed mode. The modulation reflects the fact that the injection laser tunes in and

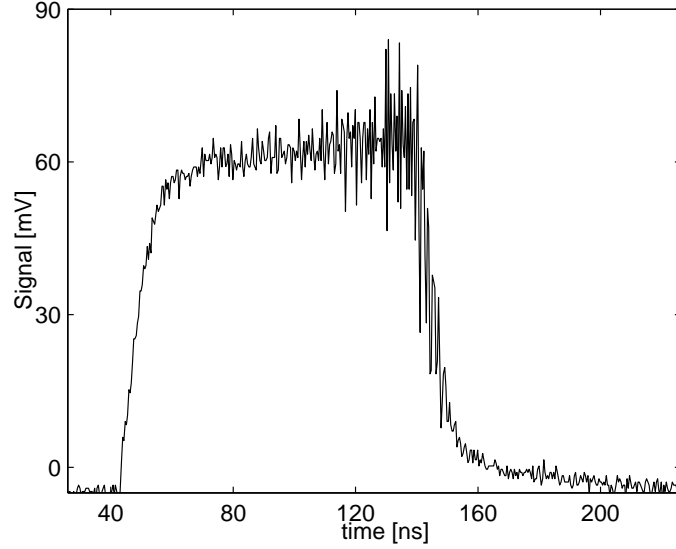


Figure 4.3: Waveform of the light pulse injected into the unstable resonator, as detected by a photodiode mounted behind the output mirror.

out of resonance with the unstable resonator, thereby indicating that the cavity is well aligned. The late appearance of the modulation comes about because the laser chirp rate diminishes rapidly during the current pulse, so that the resulting signal modulation can be, at some point, monitored.

We consider the cavity to be aligned with respect to the input beam when both the transmission of the cavity and the rapid oscillations are large.

4.2.3. Evolution of the intracavity intensity profile

Let us now move on to describe the results of a measurement of the evolution of the intracavity beam profile. Here we will focus on data obtained with an hexagonal intracavity aperture. Its circumscribing circle has a diameter of 10 mm, resulting in an unstable cavity with a Fresnel number $N_F \approx 80$. The intracavity aperture is placed at approximately 1 cm from the output mirror.

Figure 4.4 shows a typical example of the early evolution of the intensity profile. These snapshots reveal how the injected beam expands and, after reaching the aperture's edges, fades away. At the same time an intricate pattern of lines parallel to the edges of the aperture emerges, progressively covering the full aperture. This evolution occurs very rapidly. In just a few round trips the initial beam expands until it completely fills the aperture, and the profile of the injected beam can no longer be recognized. What we see here is a transition towards the asymptotic state that we seek. The pattern that emerges when the input pattern can no longer be distinguished consists of lines parallel to the edges of the aperture, and seems to agree with the hypothesis of the progressive development of edge waves as the primary mechanism for

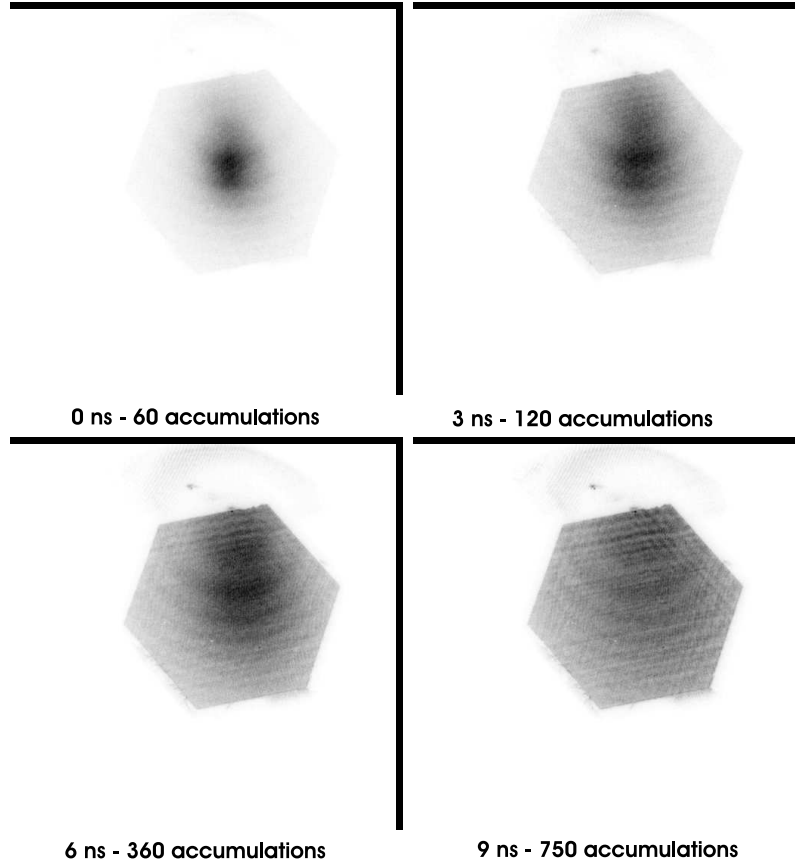


Figure 4.4: Snapshots of the intensity distribution during the first few roundtrips in the plane of a hexagonal aperture inside an unstable cavity with $M \approx 1.60$ and $N_F \approx 80$. The first picture is taken at the start of the decay. Below each picture the time elapsed since the start of the decay and the number of accumulated images are indicated. The latter number was adjusted to keep the maximum signal level approximately constant. Black: $\approx 3 \times 10^4$ counts, White: $\approx 10^2$ counts. The x and y axis of all images, i.e., the axes of the ICCD array, are aligned parallel to the horizontal and vertical directions of the page, respectively.

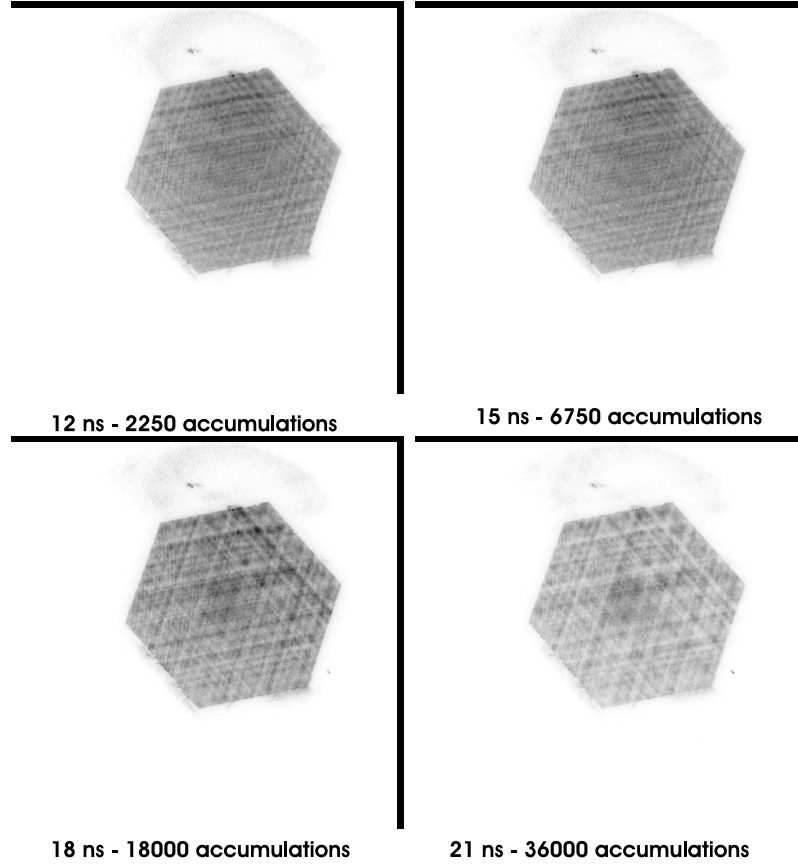


Figure 4.5: Development of a quasi-stable intracavity intensity distribution. Below each picture the time elapsed since the start of the decay and the number of accumulated images are indicated. The latter number, in all the shots but the last one, was chosen to keep the maximum signal approximately constant. Black: around 3×10^4 counts, White: $\approx 10^3$ counts.

mode formation, as proposed by Southwell [26,27]. The circular fringes at the upper edge of the aperture are caused by scattering from a localized irregularity that was unfortunately present on the aperture's edge.

The evolution of the intracavity pattern changes as the decay progresses, as shown in Fig. 4.5. First of all, the circular features seen in Fig. 4.4 are being replaced by a clearly visible highly structured pattern with hexagonal symmetry. That pattern changes slowly, a sign of convergence to an asymptotic state.

4.3. Formation of an asymptotic intracavity pattern

At this point it is not possible to continue evaluating the tendency of the profile towards the asymptotic state by mere visual inspection. Rather, we must find a procedure to determine the similarity between consecutive images. The intracavity aperture is the key to this comparison. It can be used as a reference not only because its position does not change between the images of a given decay sequence, but also because it is the origin of the diffraction that ultimately forms the fractal. Within this context a pixel to pixel comparison inside the aperture makes sense; therefore, we introduce the normalized difference image, defined within the aperture as:

$$F(i, j) = \frac{2|h_1(i, j) - h_2(i, j)|}{h_1(i, j) + h_2(i, j)}, \quad (4.1)$$

where h_1 and h_2 are the *normalized* images we wish to compare, and (i, j) are the pixel coordinates. The normalization involves an intensity scaling of one of the images so that the aperture-integrated signals of the two images are equal:

$$\sum_{\text{aperture}} h_1(i, j) = \sum_{\text{aperture}} h_2(i, j). \quad (4.2)$$

Figure 4.6 shows the results of calculating the normalized difference image late in the decay, using a single gray scale. The images shown here are for the same aperture as used previously (Figs. 4.4 and 4.5), but have been recorded with a magnifying imaging system instead of the 1:1 imaging lens of Fig. 4.2.

The complete lack of structure in the last difference image indicates that the intracavity pattern has stabilized. This would imply that the pattern that arises after 8 round trips represents the asymptotic intracavity intensity distribution, i.e., the profile of the fundamental mode of the cavity.

4.3.1. Influence of the blocking factor of the ICCD camera

A troublesome feature of the images taken after 8 round trips, as shown in Fig. 4.6, is the appearance of a bright spot in their center. This spot is very weak in the images of Fig. 4.5, but becomes more prominent as the decay of the light reaches more advanced stages. The shape of this spot is similar to that which is observed at the start of the decay process. Its presence comes somewhat as a surprise since, according to the measurements presented in section 3.7.2, all laser emission is stopped by the time that the spot is observed. An alternative explanation is that this spot is a consequence of the imperfect operation of the ICCD camera, in that it records light during the time that the photocatode is illuminated but supposedly inactive.

A first indication of the care required to properly operate the ICCD camera comes from a study of the influence of the frame rate of the ICCD camera on the measured afterglow of the diode laser. For this experiment we sent the strongly attenuated output beam of our negatively-biased pulse-driven semiconductor diode laser directly to the photocathode of the ICCD camera, i.e., without intervention of the monochromator and unstable cavity.

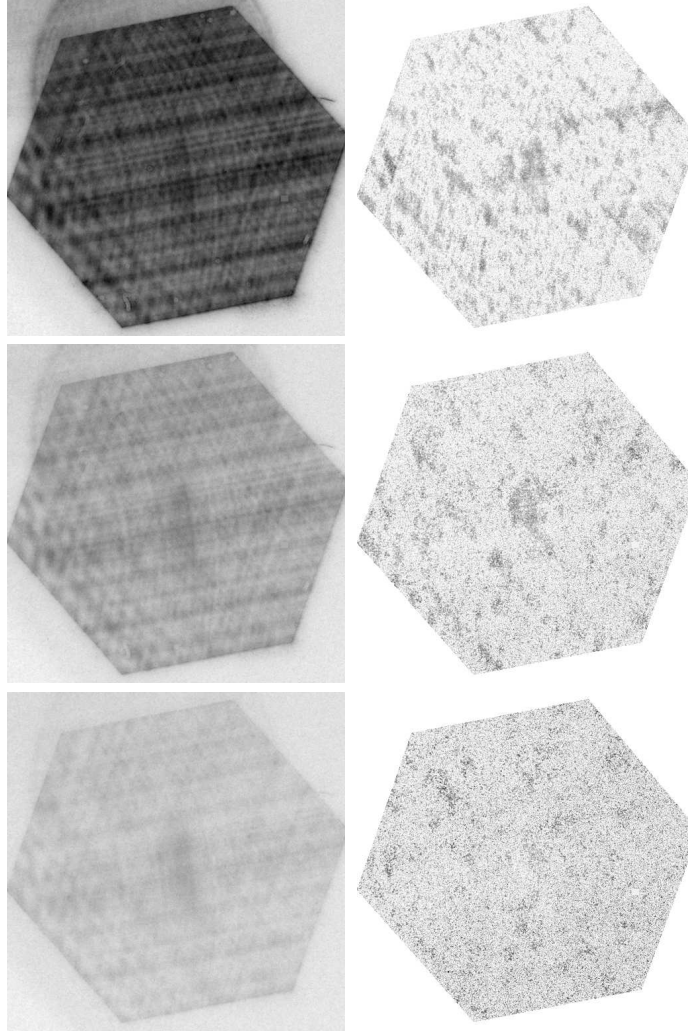


Figure 4.6: Development of a quasi-stable transverse pattern. All the images represent the sum of 100 000 camera shots. The column to the left shows, from up to down, the intracavity intensity profiles observed after 6, 7 and 8 round trips, respectively. The images are encoded with black meaning 2^{16} counts and white meaning 0 counts. The column to the right shows the image of the normalized difference between the intracavity intensity profiles at consecutive round trips. Thus, the upper image represents the normalized difference between the upper two intensity profiles of the left column, and so on. The image in the right column is encoded with black meaning highly different and white meaning highly similar. A mask has been applied to remove the area outside the aperture.

In this experiment we first roughly sample the laser output pulse by stepping the delay of the photocathode high-voltage pulse. Halfway down the pulse we choose a reference time, and carefully study the decay from that reference point on. At this stage of the laser's decay the observed signal is very weak, and therefore we are forced to accumulate many exposures to obtain a good S/N; this brings us precisely into the regime that we want to study.

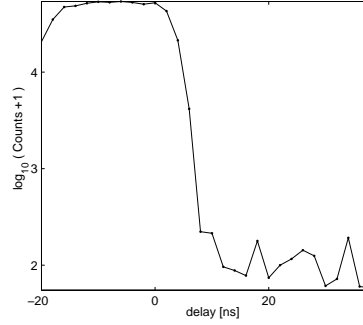


Figure 4.7: Trace of the maximum number of counts per frame vs time; the zero on the time axis is put at the start of the decay.

We drove the laser diode, biased at -4 V, by means of a square pulse with a maximum voltage of 8 V. Five ns after the beginning of the decay ($t = 0$), the maximum number of counts per pixel is about 2 orders of magnitude smaller than at the peak (see Fig.4.7). It is at this stage of the decay that we switch to the regime of multiple exposures per frame: at a repetition rate of 1 kHz, 70 hardware accumulations are enough to bring the maximum number of counts per pixel close to the saturation level of the CCD sensor.

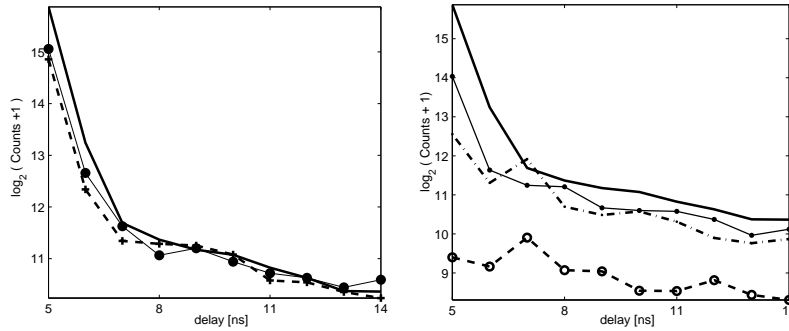


Figure 4.8: Left side: trace of the decay process at different repetition rates for all data points we recorded 70 frames. Solid thick line: at 1 kHz, solid thin line with points: at 100 Hz, dotted line: at 10 Hz. Right side: trace of the decay process as a function of the maximum laser voltage. Thick solid line: 8 V, thin solid line: 7 V, dotted-dashed line: 6 V, dashed line: 4 V.

The left side of Fig. 4.8 shows the subsequent maximum signal yield frame. The data are taken at three different repetition rates: 1 kHz, 100 Hz, and 10 Hz. We distinguish two regimes:

1. At a delay shorter than 7 ns the signal decays rapidly, and its value depends on the repetition rate of the experiment; the number of counts at a repetition rate of 1 kHz is almost twice the number as that at 100 or 10 Hz.
2. After 7 ns the decay process slows down; hereafter the number of counts per frame becomes, in essence, independent of the repetition rate of the experiment.

Note that the repetition rates chosen here are all within the specs of the camera. Possibly, the anomalous large signal at 1 kHz repetition rate is related to the fact that this repetition rate is of the same order as the decay rate of the phosphor that sits at the back end of the MCP.

The right side of Fig. 4.8 shows the signal decay as a function of delay, for laser pulses of different amplitudes (8, 7, 6 and 4 V, respectively). The intensity of the "afterglow" is seen to depend on the amplitude of the driving pulse. Such behavior can not be explained on terms of recombination luminescence in the laser diode, because the amount of light that is emitted once the laser diode is reversed biased mainly depends on the number of charges accumulated on both sides of the junction. The latter is determined by the capacitance and forward voltage drop of the diode; both quantities are independent of the forward current.

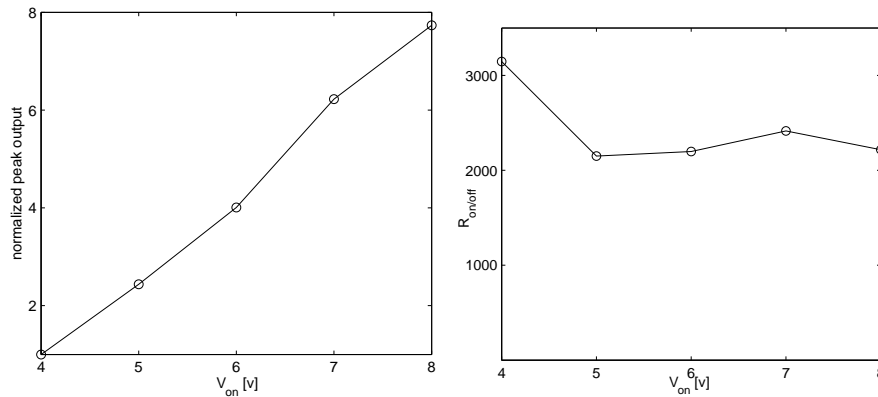


Figure 4.9: Left side: Normalized maximum counting yield as a function of the diode's peak driving voltage. The number of counts registered at 4 v was 7000. Right side: ratio between the number of counts at the peak and the number of counts 10 ns after the start of the decay, as a function of the peak voltage. 2500 accumulations were used to obtain the "afterglow" image.

The dependency of this "afterglow" with the amplitude of the driving pulse can be seen more clearly in Fig. 4.9. There we see that while the maximum light intensity scales linearly as function of the applied voltage (left image), the ratio between this intensity and that registered at reference time (10 ns after the beginning of the decay) within the slowly decay-

ing region, remains largely independent of the applied voltage(right image)¹. This evidence implies that the light observed during the slowly decaying tail also scales linearly with the pulse driving voltage. While this form of scaling is easily explained by the hypothesis of an imperfect shuttering, it is difficult to build a satisfactory model based on the luminescence hypothesis.

Therefore, we can conclude that the main limitation in the observation time of our cavity ring-down experiments, does not come from the afterglow of the laser source but from the limited blocking factor of the ICCD camera.

4.3.2. Is the asymptotic state unique?

If the asymptotic intensity distribution that we measure is that of the fundamental mode of the cavity, it should appear whatever beam we inject. To demonstrate this we modify the input beam profile by means of a diffuser, and compare the asymptotic intensity distribution acquired with that input beam with that obtained with an undiffused input beam.

The properties of the diffuser are critical. With an element that diffuses quite considerably the beam diverges so much that it is not possible to effectively couple to the fundamental mode of the cavity. On the other hand, if the diffuser is too weak, the resulting beam may not be sufficiently different from the original. Our best results were obtained when a thin Mylar sheet was used as diffuser. We start by placing the Mylar sheet just in front of the input mirror of our unstable cavity, thereby modifying the initial conditions of the decaying beam.

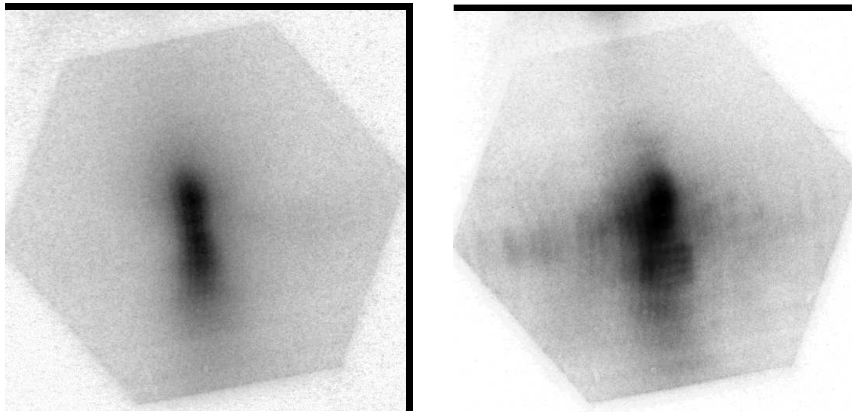


Figure 4.10: Left: original input beam. Right: input beam diffused by a Mylar sheet as observed through the unstable resonator.

Figure 4.10 shows the intracavity patterns at zero delay for a beam without (left) and with (right) diffuser. The beam that has passed the diffuser is more uniform than the original beam.

¹The intensity as a function of the voltage 10 ns after the start of the decay, was not obtained from the data set of the right side of Fig. 4.8, but of measurements with 2500 accumulations, at that specific decay

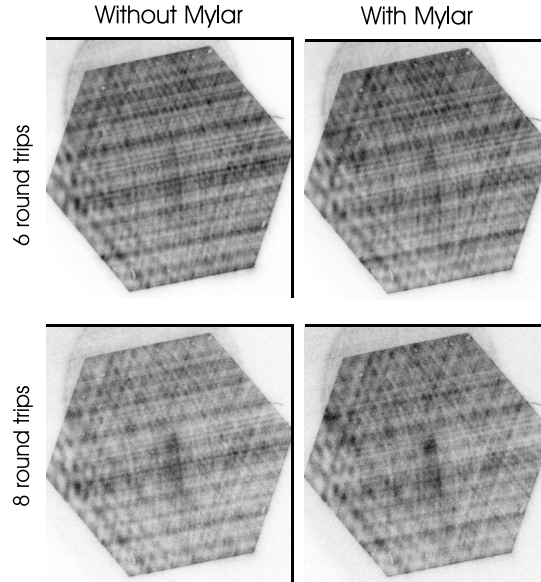


Figure 4.11: The evolution of the transverse intensity distribution for the original input beam (left column), and a diffused input beam (middle column). The images on the left are the sum of 100 000 camera shots, whereas the images obtained with the diffused beam contain 150 000 shots.

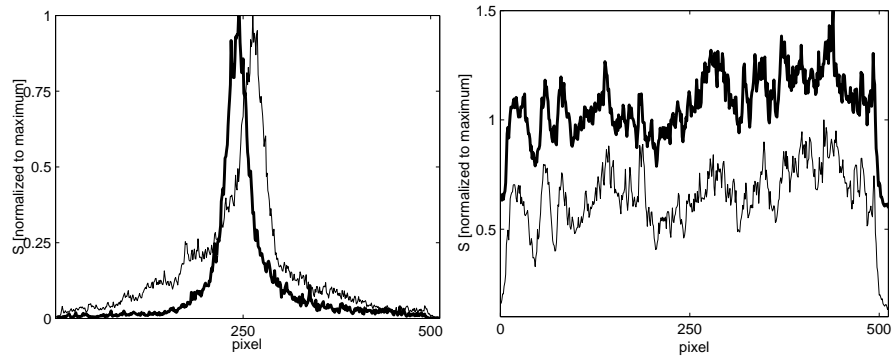


Figure 4.12: Comparison of the central horizontal cuts (i.e., cuts from left to right at half the image's height) through the intracavity intensity pattern produced by the original input beam and the diffused input beam. The thick line indicates the original beam, the thin line the diffused beam. Left figure: at the start of the decay. Right figure: same horizontal cuts after 8 round trips through the cavity; in this plot the thick line has an offset of 0.5.

Figure 4.11 shows the intracavity intensity profiles observed at late stages of the ring-down process. The eye-catching features of the profiles without and with Mylar appear identical. Unfortunately, the asymptotic convergence of the pattern could not be studied at longer delays because of the growing strength of the spot in the center of the images.

As it is not easy to estimate the importance of the differences between the images with and without Mylar, we compare a specific cut through the original images. Figure 4.12 shows a cut through the diffused and non-diffused initial beams, and a cut through the corresponding profiles 8 round trips into the decay process. The latter are highly similar: the positions and relative intensities of the main peaks and valleys are practically equal. Note that these data were taken 8 round trips into the decay where the fundamental mode may have not fully emerged.

It is important to realize that the effect of the Mylar sheet is not marginal, as could be concluded by examining Fig. 4.10. In fact, its effects on the phase of the optical field are rather considerable. To show this we introduce the Mylar sheet inside the unstable resonator and study the ensuing decay process; in such a cavity the fractal forming edge wave diffraction, i.e., the process that creates replicas of the aperture, competes with the phase randomizing effect of the diffuser. If the diffuser is too weak, then a pattern showing some resemblance to those of Fig. 4.11 or 4.6 would emerge; in contrast, if randomization is the dominant process then the fractal-looking structure will be absent in the intracavity intensity profile at the end of the decay process.

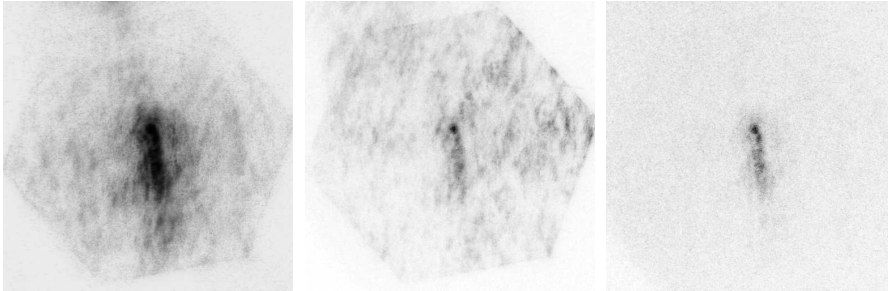


Figure 4.13: A recording of the intracavity intensity distribution when the Mylar diffuser is inside our unstable resonator. The pattern of the injection laser beam is shown in Fig.4.10 left. Left: shows the pattern emerging before the injection laser is switched off, while the frames in the middle and at right show the patterns 6 and 8 round trips into the decay, respectively. Black corresponds to a high intensity while white to a low intensity.

Figure 4.13 shows the intracavity intensity profiles observed with the Mylar sheet inside the cavity. Before the injection laser is switched off there are no major differences with the patterns observed before the beam is off with no Mylar sheet present (displayed at the left of Fig.4.10). In contrast, once the injection laser is switched off one does no longer observe the fractal-looking geometric patterns of Fig.4.11. This effect is most dramatic in the last frame, where nothing is seen but a central spot, which we attribute to the limited blocking factor of the camera. Clearly, the effect of the Mylar sheet on the amplitude and phase distribution of the intracavity light field is not marginal.

To summarize, by using a Mylar sheet as a diffuser in front of the unstable cavity, we have shown that the geometric patterns observable in the intracavity intensity distribution are essentially independent of the spatial details of the injection laser beam.

4.4. Is it a Fractal?

4.4.1. Characterizing the fractal

So far we have demonstrated that the intracavity intensity pattern reaches an asymptotic state, and that this state is roughly independent of the injection conditions. We now proceed to study its fractal features by using the Fourier method (see Section 1.1.2, and references [16, 20, 23]). In essence, the pattern under analysis is Fourier transformed, and the resulting power and phase coefficients are retrieved. The power spectrum (P^2) follows a power law:

$$P^2(k) \approx |k|^{-\beta},$$

where $P^2(k)$ is the power coefficient at frequency k , and β is the scaling coefficient. The coefficient β is linearly related with the Fourier dimension of the pattern. That relation takes the form:

$$D_F = \frac{5 - \beta}{2}, \quad (4.3)$$

when the object of analysis is a one-dimensional fractal distribution.

When the fractal imaged is "well behaved"¹, we can take 1D cuts through the 2D image, calculate their Fourier dimension (D_F) using the method outlined above, and deduce the Fourier dimension of the embedding image from [9]:

$$D_{F,2D} = D_F + 1. \quad (4.4)$$

Our procedure to study the fractal nature of the asymptotic intensity distribution consists then of:

1. Selecting a suitable 1D cut through the image.
2. Calculating the spatial power spectrum of that cut.
3. Plotting the power coefficients as a function of spatial frequency on a log-log plot, and fitting a straight line through the results.

Two complications arise here: First, the density of data points along the logarithmic spatial frequency axis is nonuniform, rapidly increasing with $\log(k)$. Consequently, the data points at low spatial frequencies carry more weight than the data points at high spatial frequencies, because the latter are very densely packed. Second, the power spectrum shows scale-dependent features, the scale being given by the cavity's magnification, due to the virtual sources [29] that give rise to the rich intensity structure. This scale dependence gives

¹By this we mean fractals that can be well defined by a single fractal dimension, in contrast to more complicated patterns like multi-fractals, anisotropic fractals, etc.

raise to deep dips in the power spectrum and can considerably affect the value of the fractal dimension obtained [85]. Yates and New [31] have suggested that both problems can be avoided by averaging the power coefficients over spatial frequency bands of constant logarithmic length. Following their idea we calculate the log-band-average power coefficients:

$$\langle P^2 \rangle_n = \frac{1}{b^n(b-1)} \sum_{k=b^n}^{b^{n+1}} P^2(k), \quad (4.5)$$

where $\langle P^2 \rangle_n$ is the log-band-average power in the n^{th} band, and b is an integer that sets the width of the logarithmic bands¹. In order to eliminate the deep dips in the power spectrum, mentioned above, the integer b has to be larger than the value of the round-trip magnification of the cavity.

4.4.2. Fractal analysis of an intracavity intensity profile

We start by analyzing a "mid-way" intracavity intensity profile, i.e., one that has not yet fully developed into an asymptotic profile; we do this since the signal-to-noise ratio of such a profile is much better than that of an asymptotic profile.

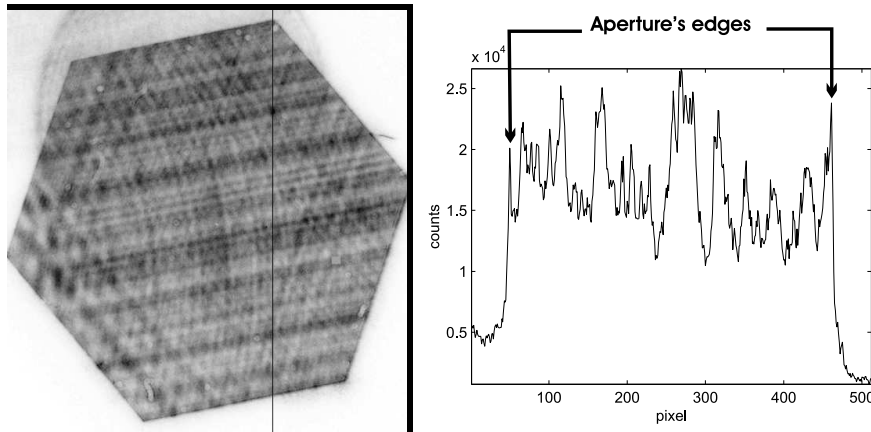


Figure 4.14: left: Intracavity intensity profile taken 7 roundtrips after the start of decay. The vertical line shows the position of the cut. Right: Intensity distribution along that cut.

¹Observe that since we are looking at a *scaling* property, the absolute values of both the power coefficients and the spatial frequency are completely irrelevant. The regressions shown from here on, are, therefore, set in terms of the $\log_2 P^2$ vs $\log_2 k$, where k is the index of the spatial frequency \mathbf{k} ($\mathbf{k} = 2\pi k/L$, with L the aperture's size, measured in camera pixels).

Figure 4.14 shows a typical¹ cut taken out of an image with hexagonal symmetry. In our analysis of this cut we include all data points. Therefore, our data set includes the signal outside the aperture and the edges of the aperture, which are indicated by arrows. It is seen that these edges do not introduce extreme signal variations. At this point we assume that the contribution from these edges will have a minor impact on the resulting power spectrum; the validity of this assumption will be investigated in the next chapter.

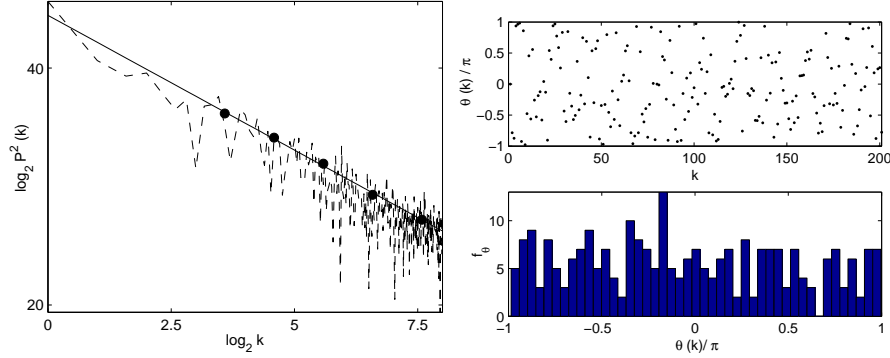


Figure 4.15: Left: Power spectrum of the data corresponding to the intensity cut of Fig. 4.14. The dashed line corresponds to the actual data, while the dots represent the log-band-average coefficients, with b equal 2. The solid line results from a fit to the dots, yielding $D_F = 1.4 \pm 0.2$. Upper right: phase $\theta(k)$ of the spatial Fourier components of the cut shown in Fig. 4.14. Lower right: the phase distribution, i.e., a histogram of the phase θ .

Figure 4.15 shows the power spectrum of the cut of Fig. 4.14 and its analysis using the log-band-average procedure. The magnification of our cavity being $M \approx 1.6$, we choose the band size $b = 2$. We fit the log-band-average power spectrum with a straight line over the range of spatial frequencies² (see Eq. (4.5)) $8 \leq k \leq 256$, i.e., $3 \leq n \leq 8$. We found that this yields a value for the fractal dimension, equal to $D_F = 1.4 \pm 0.2$. The phase component shows a homogeneous distribution, a typical signature of a fractal profile.

In order to obtain a statistically relevant value of the fractal dimension, we analyzed a series of parallel vertical cuts (Fig. 4.16, left image), of equal data length³. The histogram of values of fractal dimension D_F is also shown in Fig. 4.16. Both the mean and median of the resulting distribution yield a value of $\langle D_F \rangle = 1.37 \pm 0.03$. Based on all these results we can state that the intracavity profile of Fig. 4.15 is indeed a fractal, whose Fourier dimension is:

$$D_{F,2D} = 2.37 \pm 0.03. \quad (4.6)$$

¹By this we mean that here we deal with a cut taken at random, i.e., cuts that do not seem, qualitatively, to be different from other cuts taken at random.

²In this thesis the spatial frequency is given in units of the number of camera pixels per row, divided by the sample size.

³Observe that this requirement makes it difficult to choose cuts that are not aligned with the main axis of the detector's grid.

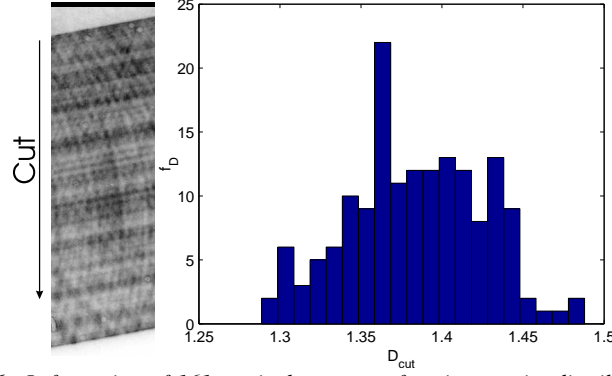


Figure 4.16: Left: region of 161 vertical cuts out of an intracavity distribution for a hexagonal aperture. Right: histogram of fractal dimensions (D_F) of the region. The center of the distribution yields a value $D_F = 1.37$, with a standard deviation of 0.03.

The consistency of this result can be checked by comparing it with the result of an alternative analysis, based on an regional average of the power spectrum over many cuts. We first calculate the average power spectrum $\overline{P^2(k)}$ at a given spectral frequency k . This average is defined by:

$$\overline{P^2(k)} = \frac{1}{N_{cuts}} \sum_{j=1}^{N_{cuts}} P_j^2(k), \quad (4.7)$$

where $P_j^2(k)$ is the power component at spatial frequency k of the cut numbered j . Subsequently, the averaged power spectrum is log-band-averaged according to the procedure of Eq. (4.5). Finally, we obtain the fractal dimension ($D_{F,<>}$) by performing a linear regression over the double averaged data set, on a log-log scale.

Figure 4.17 shows the fractal analysis of the average power spectrum for the same region previously analyzed (Fig. 4.16). The analysis of this data set yields a fractal dimension of the embedding image equal to 2.36 ± 0.02 . The agreement with the value obtained by the statistical method (see Eq. (4.6)), is excellent.

4.4.3. Evolution of the fractal dimension during the last stages of the decay

The fractal dimension measured in the previous section does not agree with the value for the fundamental mode as predicted by the theory by Berry *et al*, $D_{F,2D} = 3$ [29,30]. This does not pose a problem since the intracavity intensity profile of Fig. 4.14 has not yet converged to its asymptotic state. It was chosen as an illustrative example in order to explore our diagnostic capabilities.

We will now use the method of analysis presented of the previous section to analyze a sequence of images that includes what we believe to be the asymptotic state. We then hope

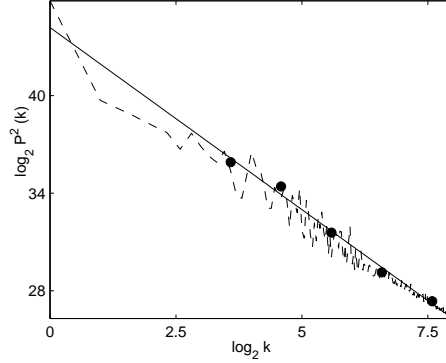


Figure 4.17: Fractal analysis of the average power spectrum of a selected region of the intracavity intensity distribution. The dashed line corresponds to the averaged power coefficients. The points indicate the log-band-average of these averaged power coefficients while the solid line shows the fit to this set of points.

that the Fourier dimension will be seen to converge to the theoretically predicted¹ value of 3 [29, 30].

We analyzed the different frames of the decay sequence shown in Fig. 4.6, by applying the average power-spectrum method of Eq. (4.7). In all frames we use the same set of cuts as shown in Fig. 4.16.

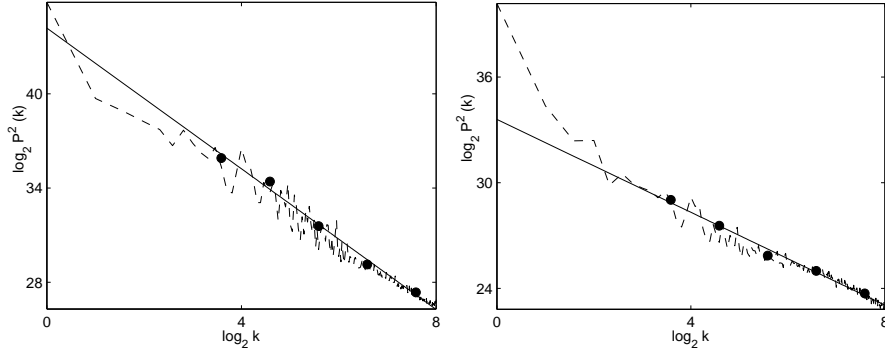


Figure 4.18: Averaged power spectra (dashed lines), their average over bands of logarithmical constant length, and the corresponding fits to straight lines (solid line). Left: 21 ns (7 roundtrips) after the start of the decay, $D_{F,<>} = 1.36$. Right: 27 ns (9 roundtrips) after the start of the decay, $D_{F,<>} = 1.79$.

¹The implication of the work by Yates and New [31] is that all modes of an unstable resonator are fractal, and that the fractal dimension of each mode is related to its loss. The higher the loss of a mode, the lower its fractal dimension. This implies that, as the intracavity beam pattern evolves towards that of the lowest-loss mode, the fractal dimension of the observed pattern will increase towards that of the fundamental.

Figure 4.18 shows some averaged power spectra of images after 7 and 9 round trips, respectively. The high-frequency data ($k > 8$) are seen to fit well to a straight line, while the low-spatial-frequency data deviate considerably, especially at longer delays. An important point to notice is that the slope of the fitted lines becomes smaller for longer delays, indicating an increase of the fractal dimension (see Eq. (4.3)).

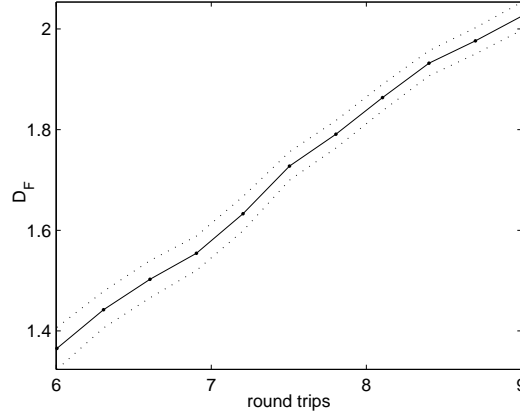


Figure 4.19: Region-averaged fractal dimension versus the number of round trips. D_F was calculated using the average over the power spectra of a region of parallel cuts. The solid line connects the data points that represent the value of the fractal dimension; the dotted line shows an estimate of the error in the value of D_F .

Figure 4.19 shows the evolution of the fractal dimension of the regional average, as a function of the number of round trips through the cavity. Clearly, the fractal dimension increases, just reaching the value of 2 at the last round trip that has been measured.

It is tempting to use these results as indirect evidence that the intracavity profile shown in the last row of Fig. 4.6 is indeed the fundamental mode of this cavity (i.e., assuming Berry's theory to be valid). This conclusion, nevertheless, must be drawn with care, since there are several issues that may be of importance and have not been included in our analysis yet. For instance, a quick look at Fig. 4.19 shows that the Fourier dimension D_F of the intracavity intensity pattern does not converge to the value of 2, but that it continues growing. This means that additional measurements at longer delays are needed. Unfortunately, that is not practical with the present setup, since the limited blocking factor of the camera makes that impossible.

4.5. Fractal dimension and the aperture's geometry: Triangular apertures

Berry [30] has predicted that the fractal dimension of the fundamental mode of an unstable resonator containing a polygonal aperture is independent of the aperture shape, although his actual considerations were mainly focused on the triangular case. Here we want to explore

the validity of this prediction.

In the experiment we replace the hexagonal aperture employed so far by an aperture in the shape of an equilateral triangle. The triangle is circumscribed by a circle of 6.2 mm radius. The Fresnel number N_F of the equivalent resonator containing a circular aperture of that radius is equal to 130. Figure 4.20 shows the transverse intracavity profile after 7 round trips.

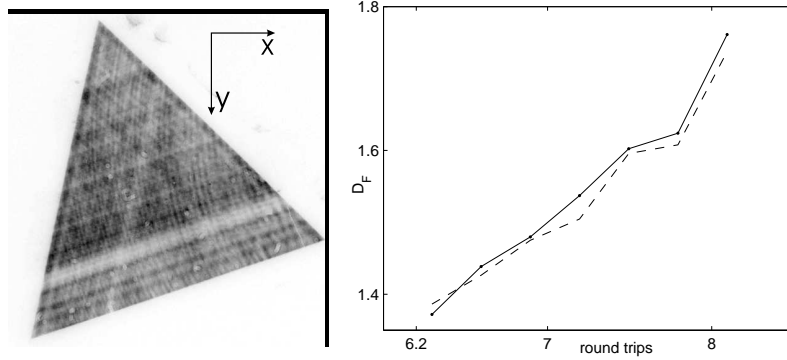


Figure 4.20: Left: transverse intracavity intensity distribution for our unstable resonator containing a triangular aperture. The pattern is taken 7 round trips after the start of the decay. Right: fractal dimension determined from a series of cuts versus the number of round trips for that resonator. The solid line represents the value for the Fourier dimension calculated from vertical cuts (y) through the image, while the dashed line shows the Fourier dimension calculated from horizontal cuts (x).

Because a triangle has no parallel edges a slight complication arises when calculating the average power spectrum in that the size of the data set that can be used is small. We therefore use only long and thin bands of data, oriented along the horizontal and vertical directions of the grid of pixels. Figure 4.20 shows the results for the fractal dimension along the vertical and horizontal cuts as a function of the number of round trips. We observe consistency between the values of the fractal dimension along the horizontal and vertical cuts, as expected. The fractal dimension does not reach the value of 2. We attribute this to incomplete mode selection. Unfortunately, the limited blocking factor of the camera made it impossible to take data further into the decay.

4.5.1. Improving the experiment by better mode matching: a pinhole as spatial selector

Mode matching of the injection beam to our unstable resonator, in a wave-optics sense, is impossible since that would require detailed knowledge of the transverse (fractal) profile. Nevertheless, a beam that propagates along the axis of the resonator, and that has a divergence that matches that of the geometric-optics eigenmode of the cavity can be viewed as effectively matched to that geometrical mode. Unfortunately, it is not possible to do this type of mode matching in a setup that contains the monochromator as a spatial/spectral filter

because the monochromator introduces much astigmatism and angular dispersion, the latter as a consequence of the frequency sweep of the diode laser. So, in order to mode match to the geometric mode we removed the monochromator and introduced, instead, a pinhole as a simple spatial filter. We checked that the "afterglow" suppression was better than the blocking factor of the camera, so we that we can proceed with the measurements.

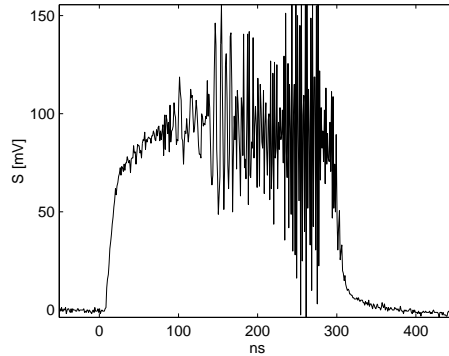


Figure 4.21: Time trace of the output of the cavity when only a pinhole is used for spatial filtering. The laser pulse was 300 ns long.

Figure 4.21 shows the response of the fast photodiode behind the cavity upon injection of a 300 ns long pulse of light. It shows that the signal is strongly modulated, which we interpret as an indication of good overall mode matching to the cavity (compare with Fig. 4.3).

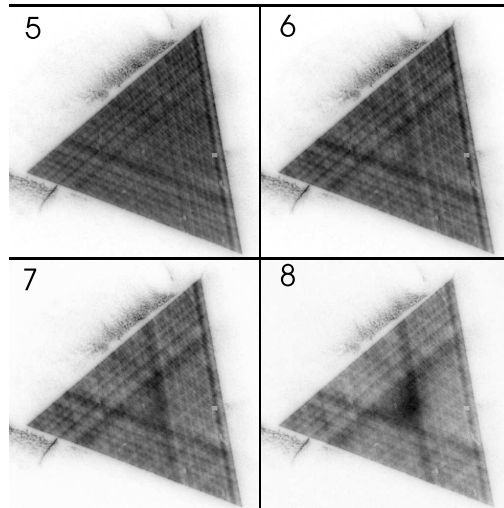


Figure 4.22: Evolution of the intracavity intensity profile through the decay. Shots corresponding to 5, 6, 7, and 8 roundtrips after the start of the decay. The number of exposures are 3×10^3 , 1×10^4 , 3×10^4 , and 6×10^4 , respectively.

Figure 4.22 shows the development of the mode profile inside the cavity. It follows, in general terms, a very similar evolution to that described in Fig. 4.5.

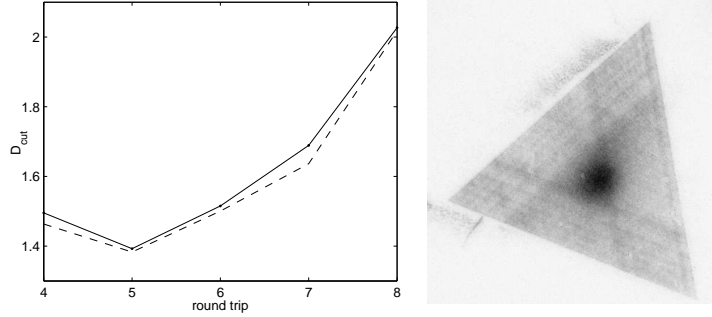


Figure 4.23: Left: Evolution of the Fourier dimension as calculated from the cuts, against the round-trip number. The solid line is the result of the regression over vertical cuts, the dotted line corresponds to the results for the horizontal cuts. Right: beam profile 9 round-trips after the start of the decay; its (2D)Fourier dimension is 3. The picture contains the sum of 6×10^4 frames.

In order to determine the fractal dimension we used regions containing the 25 longest cuts in both the horizontal and vertical directions. Figure 4.23 shows the dependence of the fractal dimension on the number of round trips; again the fractal dimension grows with time, reaching a value of 2 after 8 round trips. However, as in Sec.4.4.3, the dimension does not seem to stabilize around this value.

The intracavity intensity profile of Fig. 4.23 (9 round trips into the decay) seems to correspond to that of the fundamental mode. Our result for the value of the fractal dimension agrees with the theoretically predicted value, thereby reinforcing our earlier belief that this method to study the fundamental eigenmode of an unstable cavity is correct.

4.6. Conclusions

We have, for both hexagonal and triangular intracavity apertures, studied the evolution of the intracavity intensity distribution of an unstable resonator that is injected by a pulse of monochromatic light. For both types of apertures we find that the intracavity intensity distribution evolves towards a complex pattern that seems to stabilize after 8-9 round trips. That pattern is fractal and we find a value of the fractal dimension for the 2D image equal to three, i.e., in accord with theory. This value is, in each case, found when analyzing the intensity distribution after the maximum possible number of round trips.

Nevertheless, at this stage it is too early to draw conclusions, however tempting that may be. As we will discuss in the next chapter, the value of the fractal dimension obtained here may well have been boosted by the presence of different forms of noise. Additionally, it is not clear whether our, basically, 1D analysis method can be applied to the truly 2D fractals recorded here.

Chapter 5

Characterization of apertured fractal images carrying noise

5.1. Introduction

Our experimental method to find the structure of the fundamental eigenmode of an unstable resonator was explained in the previous chapter. There, we used the cavity ring-down method to follow the evolution of the intracavity intensity profile in a plane defined by an intracavity aperture. The fractality of the resulting images was analyzed by means of the Fourier method, applied to 1D cuts through the image. The results for the fractal dimension seemed to agree with the value predicted by Berry *et al* [29,30]. There is, however, reason to be sceptical about that result in view of the fact that:

- The number of pixels per row of our camera is larger than the collimated Fresnel number of our resonator. It is therefore doubtful that the highest spatial frequencies in the recorded intensity profile contain information on the fractal nature of the image.
- Many types of noise have a fractal signature of their own [9, 11, 12]. Therefore, the unavoidable noise that is part of our data may have influenced the results that we have obtained, in particular in those cases where the signal-to-noise ratio is small.
- We analyzed the full experimental image and not just the intensity pattern inside the intracavity aperture. Is that approach correct?

These points will be investigated in the present chapter. To do so we will use numerical simulations based on Berry's approximation [29,30] to the Virtual Source Theory [26,27,32], to calculate the profile of the fundamental mode of an appropriate model resonator. Since the points under discussion are of a general nature, we will do these calculations for a confocal strip resonator, where the fractal pattern is one-dimensional a priori, instead of for a more resonator with 2D apertures.

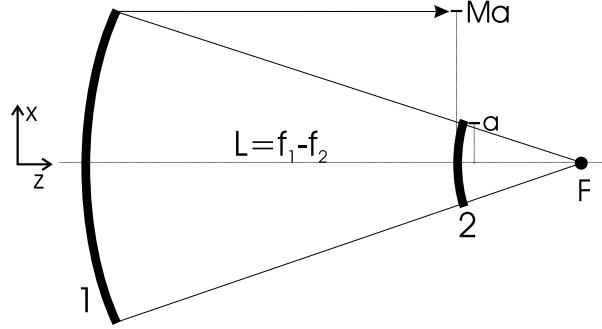


Figure 5.1: A confocal strip resonator. The concave and convex mirrors, spaced a distance L apart, share a common focal point F . The round-trip magnification M is equal to the ratio of the radii of curvature of the mirrors.

5.2. The intensity profile of our model resonator

A confocal strip resonator consists of a concave cylindrical mirror of focal length f_1 , located at a distance $L = f_1 - f_2$, from a convex cylindrical mirror of focal length f_2 . The round-trip magnification M of such a resonator is given by the ratio of focal lengths of both mirrors (see Fig. 5.1). The mode function of the fundamental mode $u_0(x)$ of this resonator, at a wavelength λ , in the region inside the intracavity aperture ($-a < x < a$), at the plane of that aperture, can be approximated by [29]:

$$u_0(x) = \frac{1}{M^{S_{max}/2}} \left(1 - \sqrt{\frac{i}{2\pi A}} \sum_{s=1}^{S_{max}} \frac{1}{\sqrt{\alpha_s}} \left[f\left(\frac{x}{M^s}, A\alpha_s\right) + f\left(-\frac{x}{M^s}, A\alpha_s\right) \right] \right), \quad (5.1)$$

where

$$A = 2\pi N_{coll} = 2\pi \frac{M^2}{(M+1)} \frac{a^2}{\lambda L}, \quad (5.2)$$

$$\alpha_n = \frac{1 - M^{-2}}{1 - M^{-2n}}, \quad (5.3)$$

$$f(y, B) = \frac{\exp\left[\frac{iB}{2}(1-y)^2\right]}{1-y}, \quad (5.4)$$

$$S_{max} = \frac{\log[A(1 - M^{-2})]}{\log M}. \quad (5.5)$$

We consider a cavity whose parameters have values close to the ones of the non-confocal cavity of section 4.2.1, i.e., its length L and magnification M are 500 mm and 1.6, respectively. This resonator contains a 1D intracavity aperture of width $2a = 12$ mm, and is illuminated by a monochromatic wave at $\lambda = 780$ nm. By inserting the values of these parameters in Eq.

(5.2) we find that the collimated Fresnel number N_{coll} of the cavity has a value of 91, roughly the same value as that of the cavity employed in the experiment described in the previous chapter. We calculate the intensity profile of the fundamental mode on a grid of length L_{grid} equal to 512 pixels, exactly the same number of pixels as that of a single row of our ICCD camera, and the results are shown in Fig. 5.2. Note that this pattern seems more regular than that found by making cuts through an experimental 2D pattern (see for instance Fig. 4.14).

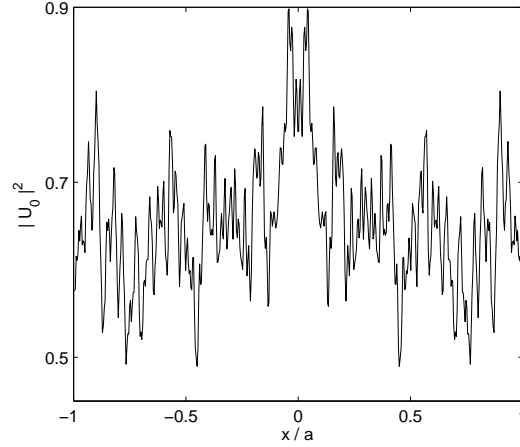


Figure 5.2: Intracavity intensity profile (calculated) of the fundamental mode of our model resonator

Figure 5.3 shows the power spectrum of the intensity profile of Fig. 5.2, Note the sudden power drop when, at the smallest spatial scales (corresponding to features approximately 6 pixels wide), the diffraction limit (i.e. $\approx a/N_{coll}$) is reached. When calculating the log-band average power coefficients (see section 4.4.1), indicated by dots in Fig. 5.3, the diffraction limit at high values of the spatial frequency is strongly felt. If one follows the standard procedure for calculating the fractal dimension of the image by fitting a straight line (dashed line in Fig. 5.3) through the log-band-average power coefficients, one finds for the slope coefficient $\beta = 1.59 \pm 0.13$, yielding $D = 1.7 \pm 0.07$. If, however, one includes only the log-band-average power coefficient for the intermediate spatial frequency range (leftmost 4 points), one obtains a fit (indicated by the solid line), with $\beta = 1.09 \pm 0.03$, thus $D = 1.95 \pm 0.02$, a value that is very close to the one predicted by Berry ($D = 2$). Note that the value for the fractal dimension $D = 1.7 \pm 0.07$ obtained by including all points in the fit has a substantially larger error than the value obtained by restricting the data set.

This behavior can be interpreted as follows: a look at the definition of $u_0(x)$ (see Eq. (5.1)) shows that it has a spatial cut-off frequency k_{max} proportional to the collimated Fresnel number N_{coll} . Therefore, its scaling behavior will be fractal up to frequencies of the order of k_{max} .

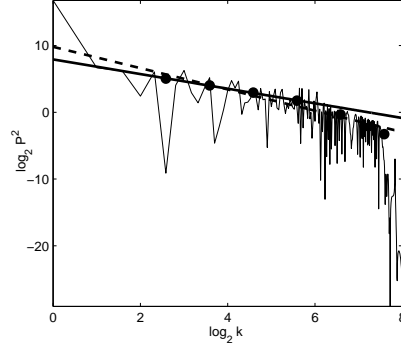


Figure 5.3: Power spectrum of the mode profile of Fig. 5.2 with the values of the log-band average indicated by dots. Solid line: fit to the four lowest log-band average points yielding $\beta = 1.09 \pm 0.02$ ($D_F = 1.91$); dashed-dotted line: fit to all values of the log-band average yielding $\beta = 1.59 \pm 0.13$ ($D_F = 1.7$).

The value of k_{max} depends quadratically on the aperture width a . Figure 5.4 shows the intensity profile and the power spectrum of the fundamental mode of an unstable resonator, whose parameters are identical to that of our model resonator, except that its aperture has a width of 40 mm. Its collimated Fresnel number N_{coll} equals 1000 ($\approx 2^{10}$). Note that, although this intensity profile appears to be very noisy, it is actually noise free. The high-frequency fluctuations that appear here are part of the fractal. In order to show the cut-off of the fractal in reciprocal space at $k \approx 2^{10}$, we have calculated the profile of the fundamental mode on a grid of 2^{16} pixels, so that k -space is sufficiently large to include the cut-off frequency.

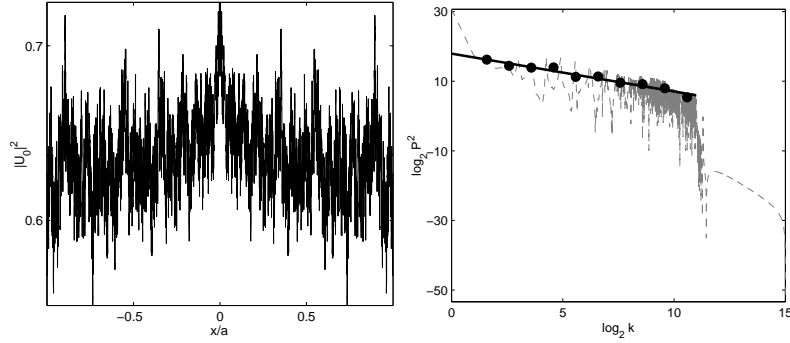


Figure 5.4: At left: Mode profile of a resonator of the same length, magnification and wavelength as our model resonator, but with an aperture of width $2a = 40$ mm. At right: The power spectrum of the mode, the fit (solid line) to the log-band averages (dots) yields $\beta = 1.08 \pm 0.05$.

Figure 5.4 shows that for spatial frequencies less than 2^{11} the power spectrum of this large-aperture resonator follows a power law. A fit (solid line) of the log-band average power coefficients (indicated by dots) yields a value for the β coefficient equal to 1.08 ± 0.05 , in excellent agreement with the value obtained for our model resonator, that has $N_{coll} = 91$. For scales beyond the resolution of the resonator (i.e., for features smaller than 16 pixels) nothing interesting is happening as indicated by the enormous drop in the power spectrum (P^2 drops by a factor of 2^{20}).

Based on these results we can reach the following conclusions:

1. A successful application of the Fourier method to the problem of finding the fractal dimension of a fractal intensity profile requires that the range of spatial frequencies on which the power coefficients are fitted to a power law, is restricted to frequencies lower than the cut-off frequency of the fractal.
2. In view of the previous conclusion we believe that the treatment of the experimental intracavity intensity profiles as presented in the previous chapter was, in hindsight, too naive. In that treatment the high spatial frequencies in the power spectrum were given undue weight.

We will now proceed to study the remaining problems identified in section 5.1, namely, the influence of image noise on the fractal profile, and the effect of not excluding the extra-aperture data.

5.3. Image noise and fractal dimension

The noise we refer to here is image noise, i.e., stochastic fluctuations either due to the discrete nature of light or to imperfections of the detector [86, 87]. To understand the origins of these fluctuations, we take a closer look at the heart of our measuring setup: the ICCD camera. Figure 5.5 shows a schematic diagram of that camera. There are 4 subsystems: i) a photocathode that converts, with probability of roughly 20%, an incoming photon into one electron; ii) a multichannel plate photomultiplier (MCP) that amplifies the charge pulse released by the photocathode; iii) a phosphor that converts the amplified charge pulse back into a light pulse, a process that is also amplifying; iv) a CCD array that converts the light pulses back into a charge; the latter is stored in a capacitor until the array is read out.

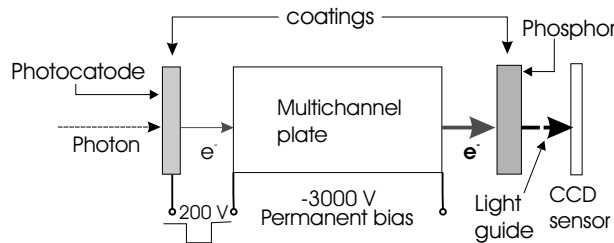


Figure 5.5: Schematic diagram of the components inside an intensified CCD camera.

An important aspect of the present ICCD camera is that the voltage difference between the photocatode and the MCP can be gated with a minimum gate time of 2.5 ns. The gate acts as a shutter for the ICCD. Note that the CCD itself is never gated, nor shuttered. It accumulates charge from one readout until the next. The charge of an individual pixel is, in the end, extracted by means of an amplifier circuit and a 16-bit A/D convertor.

So, summarizing we have:

$$5ph \xrightarrow{\text{photocathode}} 1e^- \xrightarrow{\text{MCP}} 10^4 e^- \xrightarrow{\text{phosphor}} 2 \times 10^7 ph \xrightarrow{\text{fiber}} 5 \times 10^5 ph \xrightarrow{\text{CCD}} 15 \times 10^4 e^-$$

Each subsystem contributes to the noise in the image:

1. The most important images to analyze with respect to their fractal behavior are those that are taken late into the decay of the intracavity distribution (see previous chapter). At those times the intracavity intensity is very small so that the number of photons per pixel of the CCD sensor is small even if very many frames are accumulated. Typically, the accumulated number of photons N per pixel is around 200. An image with that average number of photons per pixels is strongly affected by *shot noise*, the fluctuations in the number of photons being of order \sqrt{N} , i.e., 14 for the typical case mentioned above. Even if the other parts of the detection chain would be noise-free and thus perfect, the recorded image would carry the shot noise.

In principle the photonic shot noise can be made unimportant by accumulating a sufficient number of photons per pixel. In practice, this is less trivial than it seems, as we will see when discussing thermal noise.

2. Excess noise. This type of noise, inherent to the electron multiplication process in a multichannel plate is well known from photomultipliers. The number of electrons liberated upon impact of an electron with the walls of the MCP is not fixed but fluctuates about a mean. The result is that the output charge of the MCP per input electron varies. Additionally, when a high-energy electron hits the phosphor behind the MCP, the number of photons generated is also not constant. The various contributions to the noise of an MCP can be lumped together by specifying its excess-noise factor, which is defined as the ratio of output to input signal-to-noise ratio divided by the amplification. Typically, the excess noise factor of an MCP has a value 1.5-2 at high amplification [88].
3. CCD-sensor related noise sources, such as thermal noise, readout noise, amplifier noise, A/D conversion noise: all these sources of noise jointly contribute to the background in an image as studied in section 3.7.2. The specifications of the camera are such that the electronic noise (read-out, amplifier and A/D conversion noise) are negligible under almost all circumstances. The thermal noise of the CCD sensor is usually non-negligible, being of order 0.8 counts/pixel/sec; it gives rise to a spatially uniform background that slowly grows with time, on top of which the photonic signal resides.

This source of noise is generally weaker than shot noise. However its contribution becomes important in situations where only a few photons per exposure impinge on the CCD. In such a situation very many exposures (order 10^5 - 10^6) are necessary to form an image, and because of the limited repetition frequency of the camera (max. 5 kHz), the integration time on the CCD becomes of the order of one hour.

Because the dominant source of noise in our images is shot noise we will focus on that issue.

5.3.1. Shot noise and fractals

As seen in the previous chapter, or for that matter, in Fig 5.4, an image of a fractal intensity distribution exhibits substantial intensity variations. Consequently, both the photon number and its variance are variables that change from pixel to pixel. So, in order to construct a fractal function that carries shot noise we convert the local noise-free value $f(i)$ into a local noise-free photon number $N_{ph}(i)$. Subsequently, we include shot noise by replacing the number of photons $N_{ph}(i)$ by a random number $\mathcal{N}(i)$ obtained from a Poisson distribution with a mean photon number $N_{ph}(i)$ [89].

This conversion from the local value $f(i)$ of the fractal function to the local photon number $N_{ph}(i)$ requires a scaling parameter p that sets the overall signal to noise:

$$N_{ph}(i) = \text{int}[pf(i)]. \quad (5.6)$$

To set the scene for our study of shot noise on a fractal function we first analyze the situation where there is no fractal. Instead, the intensity distribution is flat with an average number of photons equal to 22500 per pixel. This situation, with excellent signal to noise, is shown in Fig. 5.6. The intensity scale has been chosen such that the (relatively) small signal fluctuations can be seen easily.

On the right hand of Fig. 5.6 we display the power spectrum of this intensity distribution. In line with what one expects, one sees a substantial zero-frequency component sticking out of an otherwise flat spectrum representing the noise. When the average number of photons per pixel across a flat intensity distribution is reduced, the power spectrum does not change shape, except that the peak at zero frequency is less prominent.

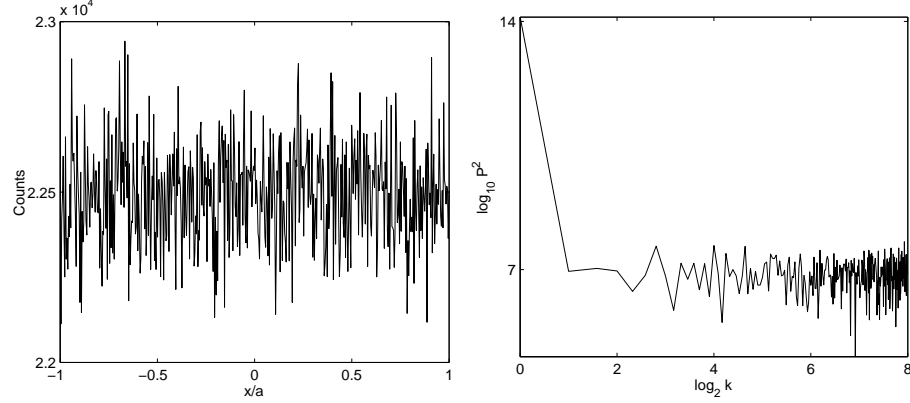


Figure 5.6: To the left: shot noise profile with 22500 average photons per channel. To the right: corresponding power spectrum.

When, in contrast, we take a *fractal* function with an average of 10000 photons/pixel, we obtain the result shown in the top row of Fig. 5.7. The mode pattern, displayed on the left, is very similar to that of Fig. 5.2, showing that, for this level of signal, shot noise is of minor importance, as expected. The power spectrum on the right shows some interesting differences with that of Fig. 5.3, in particular at the highest spatial frequencies. Whereas the noise-free fractal of Fig 5.2 carries no signal at these scales, as indicated by the sharp high-frequency drop in its power spectrum, the power spectrum of the noisy fractal does not drop as deeply at these frequencies but bottoms out at a value corresponding to the shot-noise level of the average photon number; the latter is indicated by the dotted line. Unsurprisingly, the slope parameter β of this high signal-to-noise image can be determined with high accuracy and yields a value ($\beta = 1.09 \pm 0.03$), in excellent agreement with theory.

The middle and bottom rows of Fig. 5.7 show the fractal function and its power spectrum for intermediate ($S/N = 15$) and low ($S/N = 5$) signal-to-noise ratios, respectively. For $S/N = 15$ the fractal mode profile can still be more or less recognized, while at $S/N = 5$ this is no longer true. This difference also holds for the power spectra. Whereas for $S/N = 15$ one finds $\beta = 1.09 \pm 0.03$, so that $D_F = 1.95 \pm 0.02$, in good agreement with theory, one obtains a value of $\beta = 0.50 \pm 0.07$ ($D_F = 2.21 \pm 0.03$) for $S/N = 5$. In that last case one obviously measures mostly noise. For both cases we have indicated in the graph of the power spectrum the level of shot noise corresponding to the average number of photons.

We find thus that the fractal characteristic of a 1D fractal function can be well reconstructed in the presence of substantial amounts of white noise. This is due to the fact that the fractal dimension is a parameter that measures the scaling behavior of the function, a behavior that is, apparently, not so quickly washed out by the presence of noise.

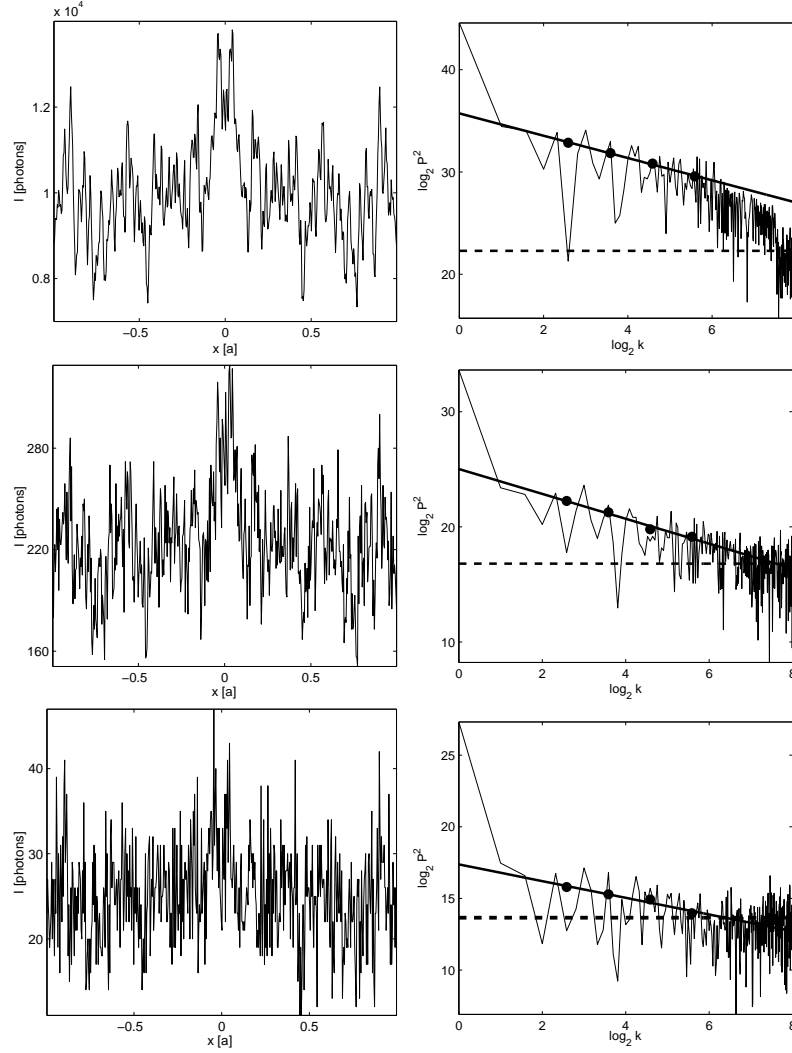


Figure 5.7: Upper row: left, Mode profile with, on average, 10^4 photons per pixel ($S/N = 100$). Right, its power spectrum yielding $\beta = 1.09 \pm 0.03$. The dashed line shows the average level of shot noise in the image, i.e., the square root of the power of its zeroth Fourier component. Middle row: left side, mode profile with, on average 225 photons per pixel ($S/N = 15$). Right side: its power spectrum; a fit to a straight line yields $\beta = 1.08 \pm 0.09$. Lower row: at the left: the mode profile with, on average, 25 photons per pixel ($S/N = 5$). To the right: its power spectrum with $\beta = 0.58 \pm 0.07$.

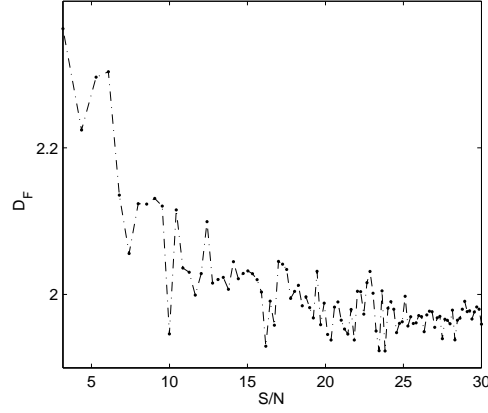


Figure 5.8: Fourier dimension of the intracavity intensity profile as a function of its signal-to-noise ratio.

In view of the fact that it is not easy to reach high levels of signal to noise in our experiments we need to know the minimum value of the S/N ratio that yields a reliable value of D_F . We have systematically evaluated the fractal dimension of our standard pattern as a function of the pattern-averaged signal-to-noise. The results are shown in Fig. 5.8 which shows that the fractal dimension obtained from such an analysis is equal to $D_F = 2.0 \pm 0.1$ if the signal to noise ratio is larger than 12. Note that if $S/N > 25$ the range of variation of the value of D_F is strongly reduced.

The sharp increase in the value of D_D at small S/N ratios reflects the fact that such images are noise-dominated. With decreasing S/N the power spectrum becomes flatter because of the ever increasing importance of noise, resulting in a larger value of D_F . The limit value is reached when the image is composed entirely of shot noise, with a maximum of $D_F = 2.5$ for a profile consisting entirely of shot noise, as trivially follows from the shot-noise profile of Fig. 5.6. Note that in the discussion presented here the excess noise has been neglected.

5.4. Apertured images

In the previous chapter we analyzed our 2D images by taking a convenient 1D cut through the image and performing a fractal analysis of that cut. Each of these cuts is 512 pixels long but the signal-containing part is, in all cases, shorter. The question we pose here is whether it is allowed to perform the fractal analysis on the full 512 pixels.

In order to clarify this issue we have to realize that the discrete Fourier transform, which is an essential step in generating the power spectrum of the mode, presupposes periodic boundary conditions. To set the stage, let us assume, for simplicity, that the mode function is constant over the full 512 pixels. This function has a nonzero Fourier component at zero spatial frequency only. If we "window" this function, i.e., impose a zero value at the beginning and end of the array, we find the Fourier spectrum of a block function (see Fig. 5.9). So, the immediate conclusion is that an analysis of cuts through the 2D image over the full 512 pixels, when not all pixels carry signal, is at best doubtful.

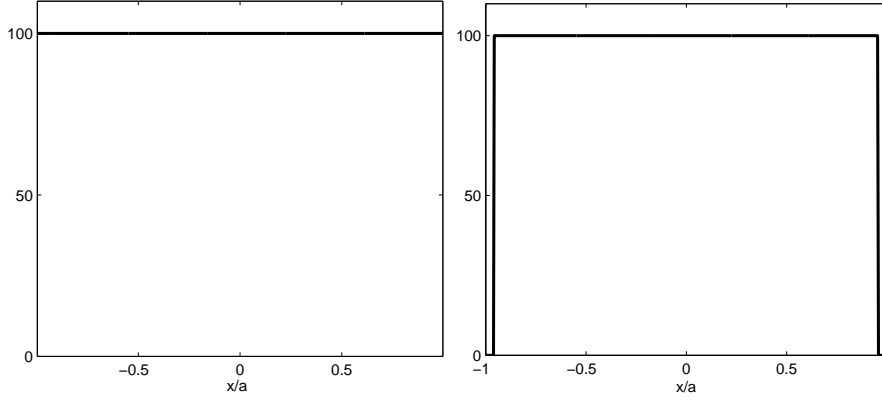


Figure 5.9: Left side: constant value function over 512 pixels. Right side: apertured function with 8 "empty" pixels both at the left and at the right side.

To see how this works out for the fundamental mode of our model resonator, we compare in Fig. 5.10 the mode function and its power spectrum for the case that the mode function fills all 512 pixels, and the case that it fills only 496 pixels, i.e., it is slightly compressed. In the latter case the intensity is set to zero in the first and last 8 pixels of the array. We will refer to this compressed version of the mode as "apertured".

We find that the power spectrum for these two situations is quite different, with slope parameters equal to $\beta = 1.09 \pm 0.02$ for the array-filling mode function, and $\beta = 1.4 \pm 0.03$ for the apertured mode function. This dramatic difference illustrates that the method of analysis used in the previous chapter is plainly wrong.

An interesting question is whether the effect of analyzing beyond the aperture can be remedied *a posteriori*. An important point here is that it is unattractive to simply remove all pixels situated outside the aperture area, as we will discuss below. One simple alternative is to reduce the DC level of the intracavity intensity function. This turns out to be helpful as indicated in Fig. 5.11. Here we plot the Fourier fractal dimension D_F of the apertured mode function as a function of the bias parameter

$$W = \frac{\bar{I}}{I_{max} - I_{min}}, \quad (5.7)$$

where \bar{I} , I_{max} , and I_{min} are the average, and the maximum and minimum values of the intensity within the aperture, respectively. It is seen that, as $W \rightarrow 0$ the value of D converges to the value of the fractal dimension of the non-apertured mode. For the case studied here, where the aperture covers 97% of the array, the deleterious effect of analyzing the fractal beyond the aperture thus can be remedied *a posteriori*.

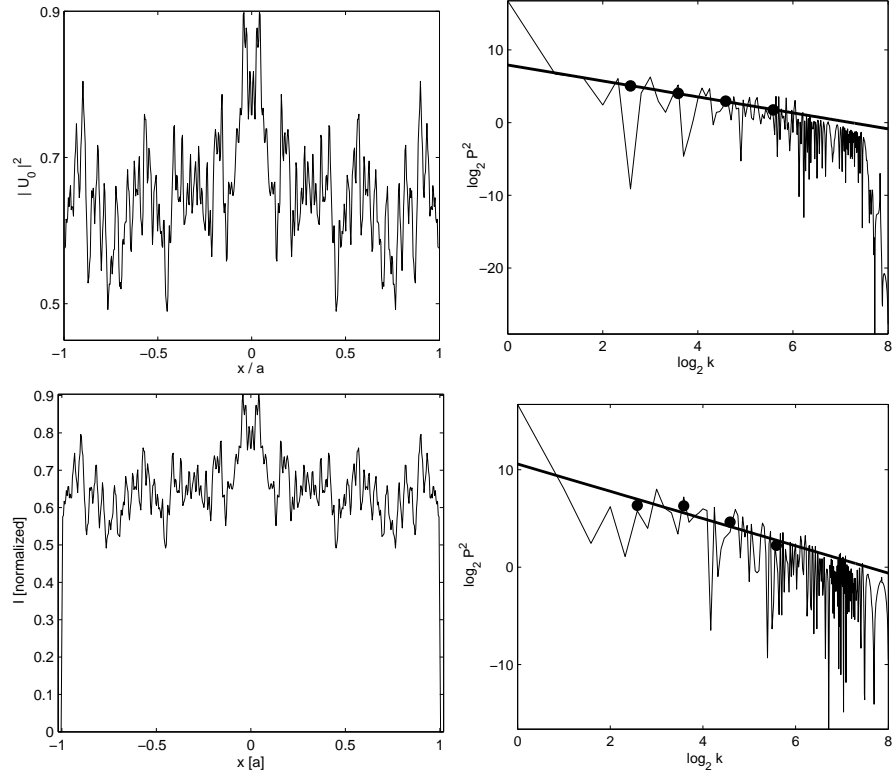


Figure 5.10: Upper row: array filling intracavity intensity distribution of the fundamental mode of our model resonator and its corresponding power spectrum (see captions of Figs. 5.2 and 5.3 for details). Lower row: spatially compressed intracavity intensity distribution of the same mode, surrounded by 8 pixels of zero intensity at both ends of the array, and its power spectrum. The fit (solid lines) to the log-band average values (dots) of the power spectrum yields $\beta = 1.09 \pm 0.02$ for the non-apertured function, and $\beta = 1.4 \pm 0.3$ for the apertured version.

At this point it is not clear how robust this approach is with respect to the variations in the compression ratio

$$Q = \frac{L_{\text{signal}}}{L_{\text{grid}}}, \quad (5.8)$$

where L_{signal} is the number of pixels that contain signal, while L_{grid} is the number of pixels of the array (512 for our camera). Here the intensity is set to zero in all pixels outside L_{signal} .

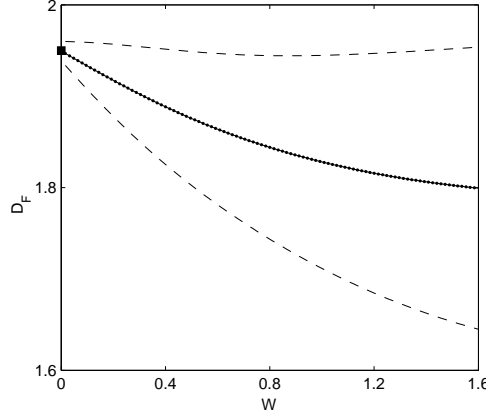


Figure 5.11: Fourier, fractal dimension of the intracavity intensity profile of Fig. 5.10 for different values of the bias parameter W . The line with dots shows the calculated value of the Fourier fractal dimension while the dashed lines show the corresponding error. The solid square indicates the value of D_F of the non-apertured intracavity intensity profile.

We will analyze this issue by assuming that the "empty" pixels are symmetrically positioned around the mode function, as in Fig. 5.12. Furthermore, in line with the previous discussion, we will remove the DC component of the mode intensity. The results for $Q = 0.99$ and $Q = 0.75$ are shown in Fig. 5.12. For the $Q = 0.99$ case we find for the slope parameter $\beta = 1.1 \pm 0.02$ while for $Q = 0.75$ we find $\beta = 0.91 \pm 0.14$. Note that the perfect case of Fig. 5.2 yields $\beta = 1.09 \pm 0.03$.

In Fig. 5.13 we show how the fractal dimension varies with the compression ratio Q . It shows that for $Q > 0.9$ the value of the fractal dimension and its error margin are similar to that of the ideal intensity profile, indicated by the solid square. Therefore, in that regime the aperture effect can be removed *a posteriori* by eliminating the DC level of the intracavity intensity distribution.

The reader may wonder why we prefer to minimize the error introduced as a consequence of analyzing the full array, instead of opting for the apparently simpler option of restricting the analysis to those pixels that carry the signal. The reason is that the latter option is not without its own problems, as we will argue here. An essential ingredient of our analysis is the use of the log-band average coefficients (Eq. 4.5):

$$\langle P^2 \rangle_n = \frac{1}{b^n(b-1)} \sum_{k=b^n}^{b^{n+1}} P^2(k),$$

where b is a number larger than or equal to the magnification of the cavity. So far we have assumed b to be integer-valued. If the maximum spatial frequency k_{max} of our image can not be written as b^N , with N an integer also, we are forced to restrict ourselves in Fourier space to those values of $k \leq b^{N-1}$, i.e., we have to throw away part of the data. A different approach involves allowing b to be non-integer valued. In that case we introduce rounding-off errors

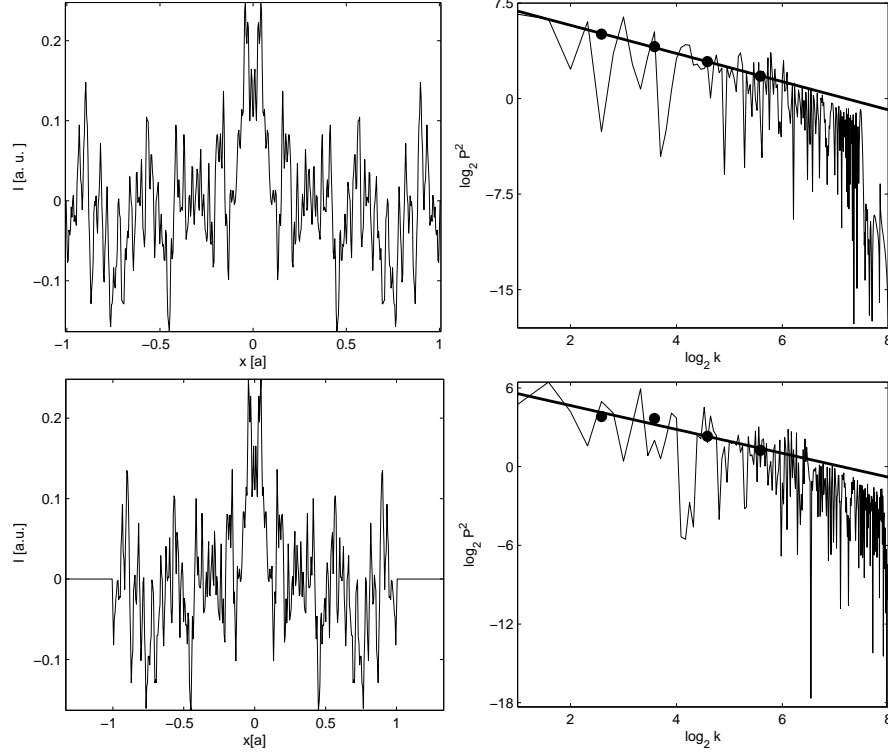


Figure 5.12: Upper row: (left): Mode profile with a filling factor $Q = 0.99$. (Right): power spectrum with regression to the region where the fractal description holds. $\beta = 1.1 \pm 0.02$. Lower row: (left): Mode profile with a filling factor $Q = 0.75$. (Right): power spectrum and its fitting to a straight line, this yields $\beta = 0.91 \pm 0.14$.

in the *length* of our logarithmic bands. These potential errors must be minimized, since they strongly affect the low-frequency components, that not only contain most of the power, but constitute a considerable component of our data set when the range of the fractal is limited.

There are three possibilities to remedy this situation: i) Limit the analysis to the largest subset of data with a number of elements b^n , where b is an integer; ii) Re-sample, by means of a suitable interpolation schema, the data under analysis to a size that fits in a segment of size b^n , with b integer; iii) The approach presented in this section. By the first approach we effectively exclude from the fit the lowest frequency components of the data set, therefore it is particularly unattractive when the range of the fractal is very limited. The second approach may work better; it is however considerably more complex than the approach presented here.

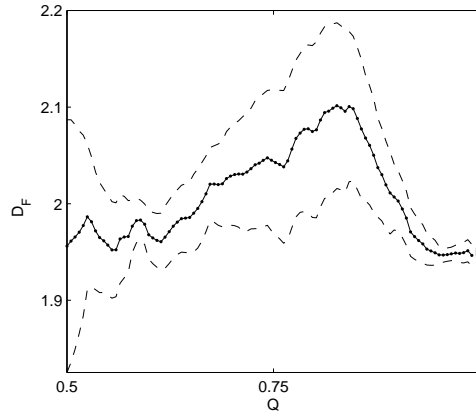


Figure 5.13: Dimension from Fourier analysis for the intracavity intensity profile of Fig. 5.12 for various compression ratios. The solid line with dots shows the value of the dimension while the dashed lines show the corresponding error margin. The solid square indicates the value of D_F of the non-aperture intracavity intensity profile.

5.5. Conclusions

We have shown that a determination of the Fourier fractal dimension of an experimentally recorded intensity pattern is not a trivial affair. In order to obtain a reliable value of the fractal dimension the experimental equipment must have very low intrinsic noise properties, and the ratio of the average signal to the level of shot-noise in the image has to be at least of order 15. Additionally, one has to take care that various experimental parameters such as CCD array size, collimated Fresnel number and image size are well tuned with respect to each other. If these parameters are out of tune the resulting value of the fractal dimension can be quite meaningless.

Based on the discussion in the last section of the present chapter we believe that it may be correct to use cuts through a 2D intensity profile that contain data both inside and outside the aperture. To do so we must remove their DC component, and the region inside the aperture must fill at least 90% of the CCD array.

Chapter 6

The fractal dimension of the fundamental mode of a plano-convex unstable resonator

6.1. Introduction

The exposition in the previous chapters brings out clearly that it is far from trivial to measure the fractal properties of the fundamental mode of an unstable resonator containing polygonal apertures. The work described in these chapters demonstrates that the experiment has to be designed with the utmost care. In particular, in the design of the experiment one has to be keenly aware of the possible pitfalls that can occur when analyzing the experimental data. It has also been shown that it is not too difficult to obtain a value of the “fractal” dimension of a certain subset of the data, but to do so in a meaningful way is not straightforward at all. In the present chapter we will show that, with a properly shaped aperture and cleverly designed experimental procedures, we have been able to measure the fractal dimension of the fundamental mode of an unstable resonator. The price that we pay is that we take a step back; we will concentrate our attention on an unstable resonator with an aperture that is effectively 1D, namely square. The experimental results presented here can be compared directly with calculations using the model presented of Section 2.6.1, while still being consistent with the results of reference [30]. Moreover, we will show that the value of the Fourier dimension is quite insensitive to the exact method to extract that value from the data, and that it is in excellent agreement with the theoretical predictions.

We begin this chapter by summarizing some of the key insights that we have acquired from the work described so far.

- An important degree of freedom in the study of unstable-resonator physics is the shape of the intracavity aperture. For instance, when the intracavity aperture is shaped as a slit or a circle the structure of the pattern is basically one-dimensional, while for a rectangular aperture it is *effectively* one-dimensional, i.e., it is 2D but separable. In these

three cases it is possible to make a 1D analysis of the pattern. For all other polygonal shapes the pattern is fundamentally two-dimensional and it is not clear whether a 1D analysis as used in Section 4.4 is actually appropriate.

For this reason it appears to be quite advantageous to use a square-shaped aperture. Additionally, with a square-shaped aperture one can take care that the full 2D intensity pattern exactly fits on the ICCD. In this way the troublesome edge effects discussed in Section 5.4 can be completely avoided.

- At the time that the fractal pattern becomes fully developed light has become very weak in the experiment. It forces us to record hundreds of thousands of images, notwithstanding the fact that the semiconductor injection laser has tens of milliWatts of output power. When all these images are added up the dominant feature of the resulting pattern as recorded by the intensified CCD camera is a rather featureless blob (see Section 4.3.1), representing the pattern of the light injected into the cavity. The presence of this blob complicates the analysis of the fractal pattern. It is therefore important to avoid its appearance; one way to achieve this, is by limiting our study to resonators with the lowest possible magnification that is compatible with the Virtual Source Theory ($M \approx 1.4$).
- The need to suppress the injection-laser afterglow becomes less stringent when the cavity magnification and, consequently the round-trip loss, are taken not too large. With less strict requirements on the afterglow it becomes possible to remove the monochromator from the path of the injected beam, thereby increasing the power of the latter by a considerable amount.
- Signal to noise is of paramount importance in the experiment but it is difficult to arrive at a realistic estimate of a minimum value of the signal-to-noise (S/N) ratio. Rather, we will use a pragmatic approach and require the S/N ratio of the image to be, at least, 15 in all experiments and see how that will work out.

6.2. Experimental setup

The core of the experimental setup is formed by the unstable-resonator cavity, see Fig. 6.1. In the present case this is a plano-convex cavity (mirror separation $L = 390$ mm) confined by one flat (radius of curvature $R_1 = \infty$) and one convex mirror (radius of curvature $R_2 = -10$ m). Using Eq. (2.11) one finds the magnification of the cavity to be $M = 1.48$. Inside the cavity a 6×6 mm sized aperture is positioned at less than 1 cm from the convex flat mirror. We inject this cavity with laser light, from a laser diode, at a wavelength $\lambda \approx 785$ nm. Operating in this way the cavity is characterized by the parameters listed in table 6.1.

The ICCD array is placed directly behind the output mirror with no optics in between. By doing so we avoid observing the circular fringe patterns that plagued the experiments described in Chapter 4. The distance between the aperture and the ICCD array is so short (< 1 cm) that the recorded image represents the near field of the square aperture¹. The size of

¹The Fresnel number ($N_F = a^2/\lambda L$) of this aperture-plane configuration yields a value of around 4600

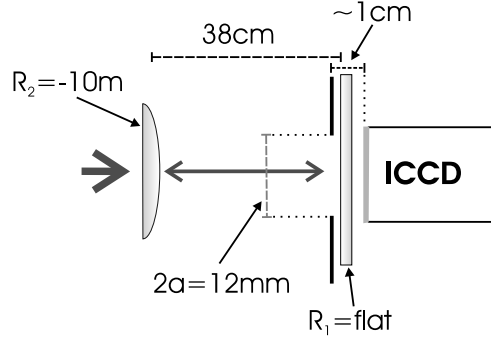


Figure 6.1: Sketch of the critical parts of the experimental setup.

| | | |
|--|-------------------|--------|
| Round-trip time | | 2.6 ns |
| Magnification | M | 1.48 |
| Collimated Fresnel number (see Eq. (2.33)) | N_{coll} | 56.7 |
| Effective Fresnel number (see Eq. (2.34)) | N_{eff} | 22.8 |
| Number of virtual sources (see Eq. (2.59)) | N | 22 |

Table 6.1: Cavity parameters

the latter is such that the cavity output pattern slightly overfills the ICCD array, in this form the aperture effects discussed in Section 5.4 are negligible.

6.3. 2D analysis of the intracavity intensity patterns

Before embarking on the analysis of the experimental data we will briefly review what to expect. One of the main advantages of using a square (or rectangular) aperture inside an unstable resonator is that the resulting intensity distribution $I(x, y)$ can be factorized, i.e.

$$I(x, y) = I(x) \cdot I(y). \quad (6.1)$$

Consequently, each row of the image contains the *same* information, namely $I(x)$, with a strength given by $I(y_0)$. Here y_0 labels the row. It is therefore allowed to add up all the rows to arrive at the contraction

$$\mathcal{J}(x) = \sum_{y_0} I(y_0) I(x). \quad (6.2)$$

Similarly, each column of the image contains identical information, namely $I(y)$, with a strength given by $I(x_0)$, x_0 labelling the column. Also here one can define a contraction

$$\mathcal{J}(y) = \sum_{x_0} I(x_0) I(y). \quad (6.3)$$

The power spectrum $P^2(k_x, k_y)$ of the (1×1) D intensity distribution $I(x, y)$ can also be factorized,

$$P^2(k_x, k_y) = P^2(k_x) \cdot P^2(k_y), \quad (6.4)$$

where $P^2(k_x)$ and $P^2(k_y)$ represent the power spectra of $I(x)$ and $I(y)$, respectively. Up to a numerical constant, $P^2(k_x)$ and $P^2(k_y)$ are equal to the power spectra of $\mathcal{I}(x)$ and $\mathcal{I}(y)$, respectively. If the aperture is truly a square and is well aligned to the cavity axis one expects that the intensity distribution $I(x, y)$ has the symmetry properties of a square. For instance, this implies that $I(x) = I(y)$ so that $P^2(k_x) = P^2(k_y)$ also.

The results of a calculation using the virtual source theory outlined in Chapter 2 for the resonator/square-aperture combination under discussion are displayed in Fig. 6.2. In order to make this a useful exercise we have “quantized” the intensity profile by assuming that the spatially averaged signal corresponds to 400 photons per pixel (which is a realistic value). Each intensity value $I(x, y)$ is then converted into a photon number value $N(x, y)$ with corresponding noise. The shot-noise value $\Delta N(x, y)$ at a particular pixel (x, y) is randomly chosen from a Poissonian distribution with mean value $\sqrt{N(x, y)}$.

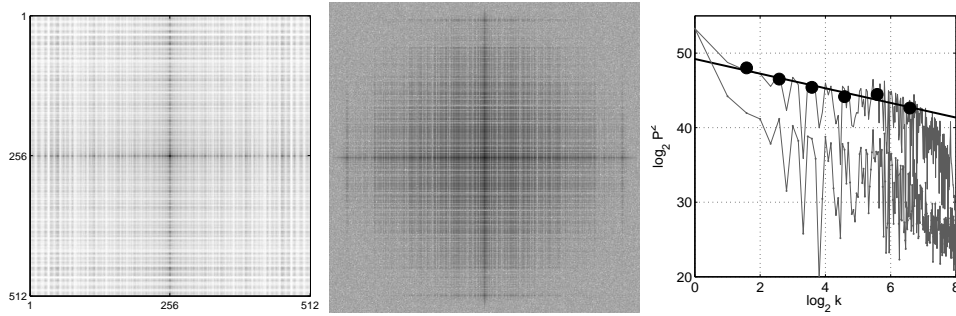


Figure 6.2: Pattern, including shot noise, of the fundamental mode of the plano-convex unstable resonator of Fig. 6.1 as calculated using virtual source theory; the average intensity corresponds to 400 photons per pixel. From left to right are shown the intensity pattern, the spatial power spectrum of the intensity, and two cuts through the spatial power-spectrum. k is given in units of 512 pixels divided by the sample size.

The frame at the left shows the intensity distribution $I(x, y)$, the frame in the middle, the 2D power spectrum $P^2(k_x, k_y)$, while the frame at the right shows the result of analyzing specific cuts through the power spectrum in the spirit of Chapter 4. Both the intensity distribution (left frame) and the power spectrum (middle frame) show a high degree of symmetry, the strongest signals appearing when either $x = 0$, $y = 0$, $k_x = 0$, or $k_y = 0$. The middle frame clearly shows how the presence of noise affects the corner of the 2D power spectrum. This is made more clear in the frame at the right where the top curve shows cuts through the power spectrum along either the k_x or k_y axes (the curves are exactly on top of each other and thus indistinguishable), while the lower curve shows a cut along one of the diagonals of the power-spectrum image. Clearly, the signal level along such a diagonal is much reduced and therefore less attractive for further analysis. With the values of the cavity parameters as listed in Table 6.1 one finds that the edge waves have a maximum spatial frequency of $\approx 120 \text{ pixel}^{-1}$, nicely corresponding to the cutoff seen in the right frame of Fig. 6.2.

The full circles indicate the band-averaged power spectrum, as discussed in Chapter 4, while the solid line shows a fit of a straight line (within a log-log plot) to the band-average values. This straight line has a slope $\beta = -0.98 \pm 0.09$, yielding a fractal dimension for the 2D-pattern equal to $D_{F,2D} = 3.02 \pm 0.05$, in excellent agreement with the theoretical predictions.

6.4. Experimental results

When the injection laser has just been switched off the ICCD records predominantly the light that has just been injected into the cavity. Figure 6.3 shows a record (150 accumulations) of the injected beam, together with its power spectrum and some cuts through the latter. The

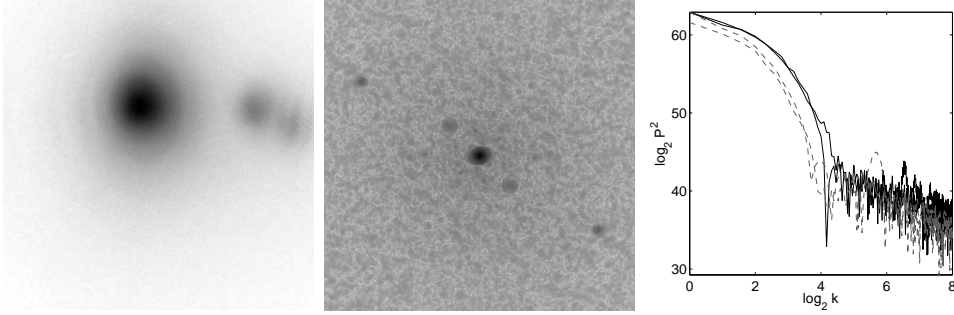


Figure 6.3: The pattern of the light transpiring through the output coupler just after the injection laser has been turned off. From left to right: the spatial intensity distribution $I(x,y)$, its power spectrum $P^2(k_x, k_y)$, and some cuts through the power spectrum. The solid lines represent the cuts $P^2(k_x, 0)$ and $P^2(0, k_y)$, while the dashed lines show the result for diagonal cuts.

intensity distribution shows a bright localized feature representing the injected beam and two much weaker features, due to reflections from the camera's surface. The power spectrum is characterized by a sharp peak around the origin and a few much weaker features that represent unintentional interference fringes. The cuts through the power spectrum show that the central peak extends to k -values of ≈ 16 (i.e., to spatial periods larger than 32 pixels).

Ten round trips later the signal level is orders of magnitude lower due to magnification and mirror-transmission loss. The intensity pattern (see the left frame of Fig. 6.4) obtained by recording 350,000 frames, is dominated by a localized feature at the same position as that in Fig. 6.3. As discussed in Chapter 4 this feature is not part of the intensity distribution escaping from the cavity. Rather, it represents a weak accumulated signal that has been generated by the ICCD itself in response to the intense illumination of the intensifier before the laser is switched off.

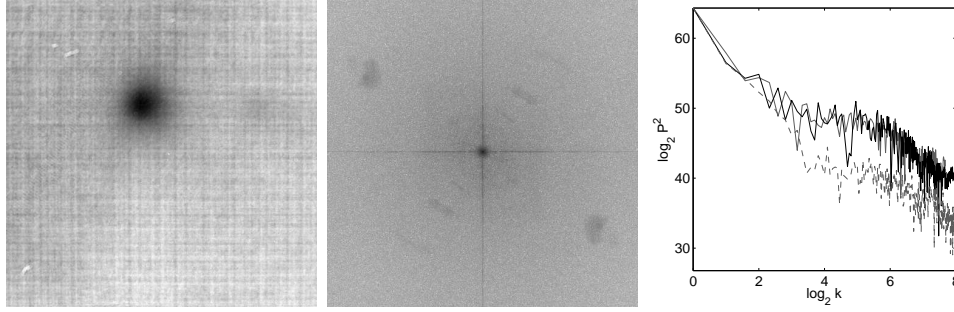


Figure 6.4: The pattern of the light transpiring through the output coupler ten round trips into the decay. From left to right: the spatial intensity distribution $I(x,y)$, its power spectrum $P^2(k_x, k_y)$ plotted logarithmically, and a series of cuts through the power spectrum. The solid lines represent the cuts $P^2(k_x, 0)$ and $P^2(0, k_y)$, while the dashed lines show the result for diagonal cuts.

6.5. Data analysis

In Sections 4.4.1 and 4.4.2, a variety of methods were introduced to determine the Fourier dimension of a fractal pattern. Here we will apply all of these methods to the experimental data obtained for the plano-convex cavity of Fig. 6.1, in particular the data of Fig. 6.4.

6.5.1. The full 2D data

To analyze the full 2D data shown in the left frame of Fig. 6.4 we calculate the power spectrum of the full data, the result being shown in the middle frame of the figure. Because of the separability of the power spectrum (see Eq. (6.4)) it suffices to analyze the cross sections along the k_x and k_y axes, i.e. $P^2(k_x, 0)$ and $P^2(0, k_y)$. We expect the fractal dimensions D_F obtained by analyzing these two cross sections to be equal, and to be simply related to the fractal dimension of the 2D data $D_{F,2D}$ by:

$$D_{F,2D} = D_F + 1. \quad (6.5)$$

In the analysis of these cross sections we have to take into account that the maximum spatial frequency of the pattern is expected to lie at $|k| \approx 128$. At the same time, because of the artefact in the center of the power spectrum associated with the strong "ghost signal" seen in the left frame of Fig. 6.4 it is mistaken to associate spatial frequencies $|k| < 8$ with the diffraction pattern. Unfortunately, the analysis of the power spectrum should therefore be limited to spatial frequencies $8 < |k| < 128$. Figure 6.5 shows the results along the positive k_x -axis (left frame) and along the positive k_y -axis (right frame). The average over bands of logarithmically constant length are indicated by the squares; the latter are fitted to a linear function, represented by the thick solid line. From its slope one can calculate the Fourier dimension, $D_{(1 \times 1)F,x} = 1.8 \pm 0.15$ and $D_{(1 \times 1)F,y} = 1.85 \pm 0.09$.

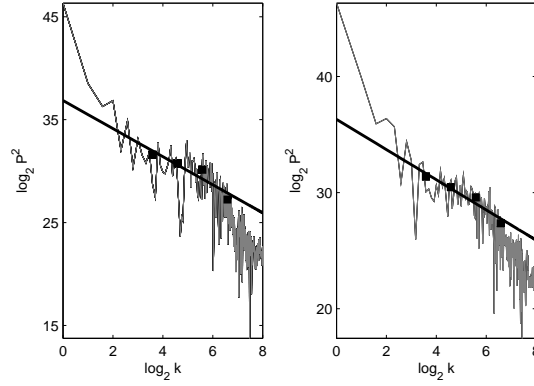


Figure 6.5: Cross sections along the horizontal (left frame) and vertical (right frame) axes of the 2D power spectrum of the intensity distribution 10 round trips into the decay of the injected signal, together with the values of the band average, indicated by squares, and a straight line, fitted to the band averages.

6.5.2. Regional average of intensity over 1D cuts

Here we want to apply one of the methods for analysis that was applied in Chapter 4 to the experimental data obtained with a hexagonal aperture. This method consists of selecting part of the full image, calculate an average over the selected region and analyze that average. In the preset case, where the intracavity aperture is a square we select rectangular parts of the image¹ (see Fig. 6.6) and determine the regional averages as:

$$\mathcal{J}(x) = \sum_{y_1}^{y_2} I(x, y),$$

$$\mathcal{J}(y) = \sum_{x_1}^{x_2} I(x, y).$$

We then calculate the power spectra of these regional averages, determine the averages over bands of logarithmically constant length, fit the resulting values to a straight line and then calculate the Fourier fractal dimension. For the power spectra shown in Fig. 6.6, which have their origin in the same intensity pattern as the power spectra of Fig. 6.5, this yields $D_{F, <x>} = 1.85 \pm 0.15$ and $D_{F, <y>} = 1.90 \pm 0.13$.

6.5.3. Fractal dimension of individual cuts; statistics

In Chapter 4 we applied yet another method of analysis to our data. The essential step here is to select a large number of cuts from the intensity pattern, i.e., extract the intensity functions $I(x, y_0)$ where x is the running variable, and $I(x_0, y)$ with y the running variable. Subsequently, one calculates the power spectra associated with each intensity function $I(x, y_0)$

¹ Such rectangular parts are chosen such that they exclude the 'blob' of the image.

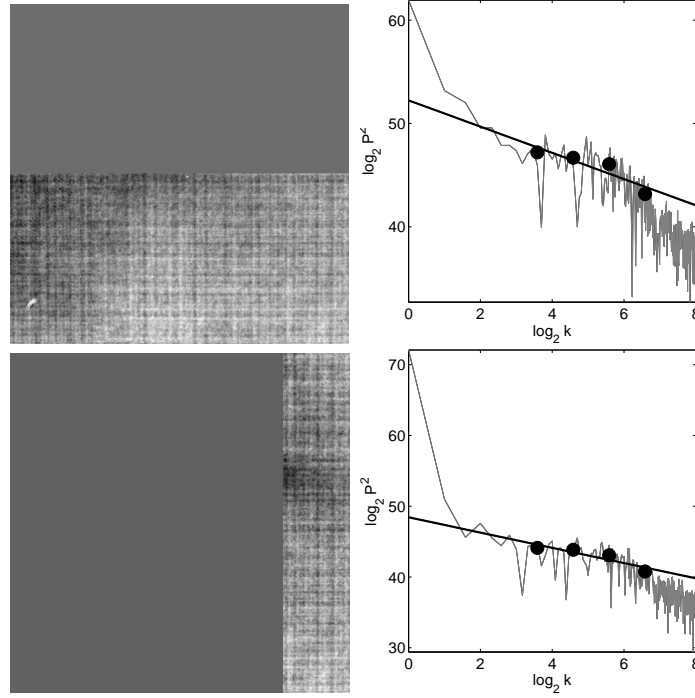


Figure 6.6: Selected parts of the intensity pattern 10 round trips into the decay for analysis by regional averaging are shown in the frames at left, the top one selected to calculate $\mathcal{J}(x)$, and the bottom one to determine $\mathcal{J}(y)$. The frames at right show the corresponding power spectra, including the band-average values and the straight line fit to the band averages.

and $I(x_0, y)$ and determines the Fourier fractal dimension from these power spectra in the standard way. This yields a distribution of values for the fractal dimension from which one can derive an average value for horizontal cuts through the intensity pattern and an average value for vertical cuts. Figure 6.7 shows the results, using the same cuts as used in the regional averages (see previous section). We find $\langle D_{F,x} \rangle = 2.05 \pm 0.09$ and $\langle D_{F,y} \rangle = 2.10 \pm 0.09$.

6.6. Stability of the fractal dimension

Luckily, the various methods discussed above to extract the Fourier fractal dimension of a single pattern cluster around single values, which are: $\langle D_{F,x} \rangle = 1.95$, and $\langle D_{F,y} \rangle = 2.0$. This is not really surprising since all of these methods involve averaging in some way, either over (parts of) the intensity distribution or over (parts of) the power spectra. However, they weight the intensity distribution or power spectrum in a slightly different way, giving rise to small fluctuations in the value of the Fourier fractal dimension.

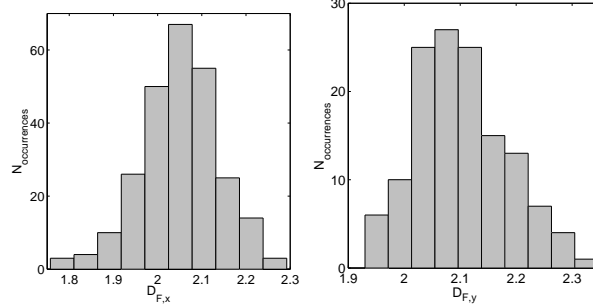


Figure 6.7: Histograms of the values of the Fourier fractal dimension obtained by extracting the fractal dimension from individual cuts through the intensity pattern. The left frame shows the result for horizontal cuts; the vertical cuts appear in the right frame.

Apart from the fact that the various methods of analysis applied by us to a single measured pattern basically yield a single value for the Fourier fractal dimension, that value is also close to the theoretical prediction. It is, however, dangerous to jump to the conclusion that we have confirmed the theory because we have analyzed a single pattern only. The program of the present section is to show that our value of the Fourier fractal dimension is quite robust.

6.6.1. Varying the number of exposures

One of the issues that beset the measurements of Chapter 4 and that we addressed numerically in Chapter 5 is the question of the signal to noise. The experimental handle we have on this quantity is the number of exposures used to measure the intensity distribution. Figure 6.8

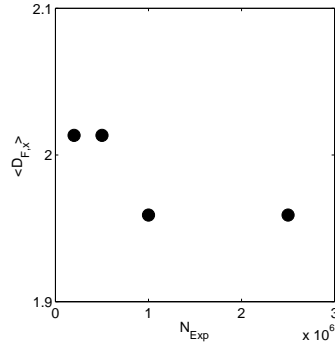


Figure 6.8: The value of the Fourier fractal dimension as a function of the number N of accumulated images 10 round trips into the decay of the intracavity intensity distribution. A set of 256 horizontal cuts through the intensity distribution were analyzed.

shows the value of the Fourier fractal dimension obtained by the method of Section 6.5.3 as a function of the number of accumulated ICCD camera shots acquired 10 round trips after

switching off the injection laser. On the basis of the measured intensity distribution we estimate the signal to noise of the image containing the largest number of accumulations as ≈ 29 . The value of the fractal dimension is based on statistics involving a set of 256 horizontal cuts through the intensity distribution. The figure shows clearly that the fractal dimension is insensitive to the number of exposures in the range studied.

6.6.2. Varying the injection conditions

It is also important to clarify whether the fractal dimension depends on the specific arrangement of the experiment. To answer that question in its full breadth would force us

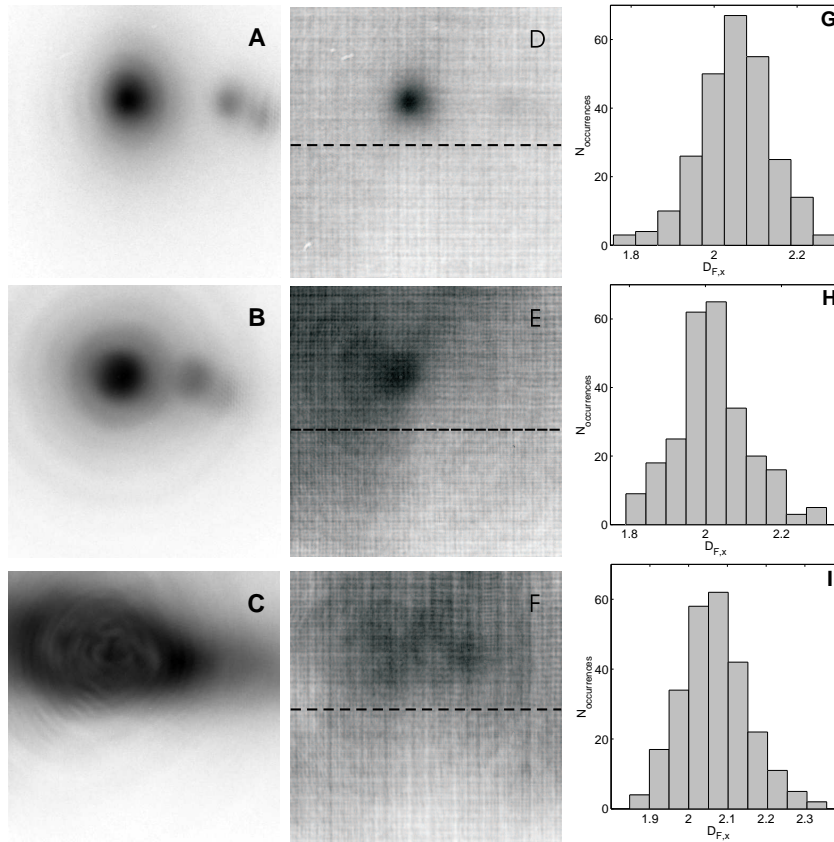


Figure 6.9: Results for three different modes of injecting the laser light into the cavity. Frames a-c represent the measured intensity distribution at the very start of the intra-cavity decay, while frames d-f display the intensity pattern as measured 11 round trips into the decay. The brightest feature in these frames is a “ghost image” of the injected beam which has been already discussed in the context of Fig. 6.3. Finally, frames g-i show the histogram of values of the fractal dimension evaluated for all horizontal cuts below the dashed lines in frames d-f.

to build a variety of unstable-resonator cavities and investigate the fractal characteristics of the pattern upon cavity ring down.

This is hardly a realistic route so we have studied whether the fractal dimension of the intensity pattern upon ring down of the cavity of Fig. 6.1 depends on the details of the injection conditions. Specifically, we have varied the diameter of an aperture that is positioned in the injection path¹. The results are shown in Fig. 6.9. The left columns shows the intensity patterns observed just after the injection laser is switched off, while the middle column portrays the patterns 11 round trips into the decay. The fractal dimension is obtained by the method of Section 6.5.3 using all cuts below the dotted lines in frames d-f. The statistics of the fractal dimension evaluated from each cut is shown in the column at right for the three different injection conditions. From top to bottom we find $\langle D_{F,x} \rangle = 2.05 \pm 0.05$, $\langle D_{F,x} \rangle = 2.01 \pm 0.03$, and $\langle D_{F,x} \rangle = 2.05 \pm 0.05$. This is in perfect agreement with the theoretical prediction.

6.6.3. Does the value of the fractal dimension converge?

As discussed in many places in this thesis, the idea of using cavity ring down in our experiments is that, after a sufficiently large number of round trips, the intracavity intensity distribution equals that of the fundamental mode of the resonator. Earlier in the decay the intensity distribution is the result of a superposition of cavity eigenmodes, each having their own fractal dimension, and it is unclear, nor relevant, whether these intensity distributions are true fractals and, if so, what their fractal dimension is. It is, however, always possible to systematically apply our technique of analysis to measured intensity distributions and extract the “fractal” dimension D of the resulting pattern. If all is well, D will converge as a function of the number of round trips through the cavity, to the value $\langle D_{F,x} \rangle$.

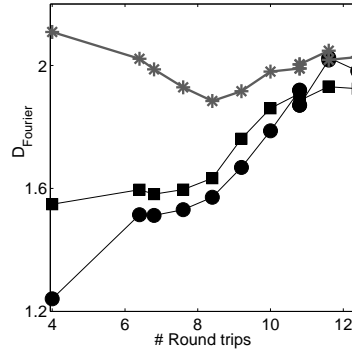


Figure 6.10: Convergence of the value of the fractal dimension of the intracavity intensity distribution as a function of the number of round trips through the cavity. Three methods of analysis were used to arrive at the indicated data; that of Section 6.5.1, indicated by circles, that of Section 6.5.2, indicated by squares and that of Section 6.5.3, indicated by asterisks.

¹The diameters of the aperture were, for the top row $\approx 0.1\text{mm}$, for the middle row $\approx 0.3\text{mm}$, and for the lower row 25mm

Figure 6.10 shows our experimental results for the case that a narrow well-collimated beam is incident on the cavity (see Fig. 6.9b). Here we have applied three different methods of analysis. The circles give the value for the full 2D data (see Section 6.5.1), i.e., $D_{(1 \times 1)F,x}$; the squares the value for the regional intensity averages (see Section 6.5.2), i.e., $D_{F,<x>}$, while the points indicated by an asterisk represent the average over a histogram of fractal dimensions (see Section 6.5.3), i.e., $<D_{F,x}>$. While the values of D obtained by these three methods are quite different early into the decay, reflecting the fact that the fundamental mode has not fully developed and that they probe this in different ways, they all converge later into the decay to a common value D_F , namely $D_F = 1.95 \pm 0.1$. We have obtained equivalent results for other injection conditions.

6.7. Conclusions

In this chapter we have proved that the fundamental mode of a plano-convex resonator bounded by an square aperture is a fractal. We have measured the Fourier dimension of the resulting intensity profile along the directions perpendicular to the aperture's edges, finding it to be equal to 1.95 ± 0.1 . We therefore conclude that the Fractal dimension of the 2D intensity profile is equal to 2.95 ± 0.1 , in agreement with the theoretical prediction¹ $D_F = 2$ and $D_{F,2D} = 3$, respectively.

¹See references [29, 30], or Sec. 2.6.2

Epilogue: Open questions

The experimental work described in this thesis confirms the prediction of the article by Berry *et al* [29], that the Fourier fractal dimension of the lowest order mode of a 1D unstable resonator is equal to 2 (3 for the modes of an unstable resonator with square aperture). However, we have not been able to prove Berry's prediction, formulated in a complementary article [30], that the Fourier fractal dimension of the fundamental mode of a resonator bounded by a polygonal aperture, is independent of the aperture shape, and has a value of 3. The problem here lies not in the experimental technique of recording the data with sufficiently large signal to noise. Rather, it is the technique used to characterize the recorded images that is problematic.

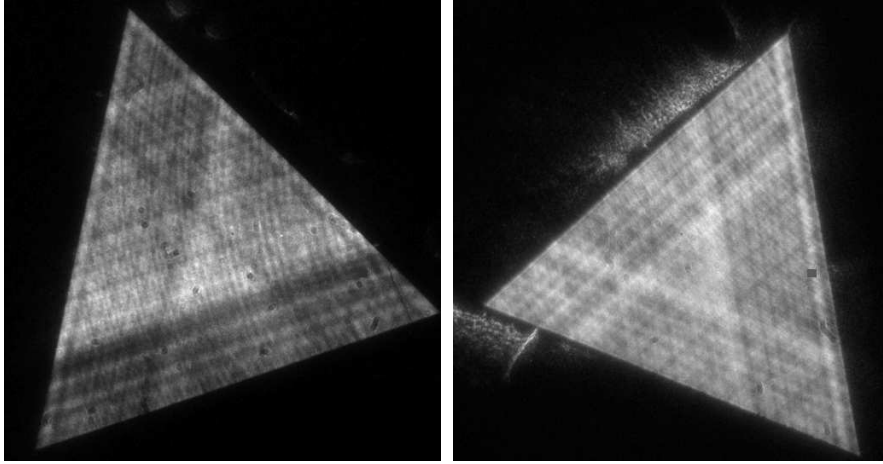


Figure 1: Two experimental intensity profiles obtained with a triangular confining aperture. These mode profiles are taken from the results presented in Chapter 4.

Figure 1 shows, for instance, experimental recordings of the eigenmode pattern of two different unstable resonators containing a triangular intracavity aperture. These patterns strongly suggest that the eigenmodes have a fractal character, but the question is how to prove that beyond reasonable doubt, and find the fractal dimension?

From a theoretical point of view the Fourier dimension is the natural choice to quantify the scaling properties of these modes. However, one encounters problems when trying to

determine the Fourier dimension from the experimental images since the edges of the aperture appear prominently in these images, and affect the Fourier dimension. While there are methods to reduce the signature of the aperture edges on the Fourier method, it is a tricky adventure to embark on.

The main questions that this thesis leaves open are therefore: i) What is the best way to analyze the fractal images that contain the confining aperture? and ii) what is the relation between the fractal dimension obtained by that method and the Fourier dimension?

Leiden, August 2005

Appendix A

Asymptotic expansion of an unstable resonator

In this appendix we will develop the asymptotic approximation to the Huygens-Fresnel propagator of an unstable resonator, as used in virtual-source theory. The purpose of this is to complement the discussion in section 2.6. Our point of departure is the Huygens-Fresnel integral for an unstable resonator [32]:

$$\xi U(x_{\text{out}}) = \sqrt{\frac{it}{\pi}} \int_{-1}^1 e^{-it(x_{\text{in}} - \frac{x_{\text{out}}}{M})^2} U(x_{\text{in}}) dx_{\text{in}}. \quad (\text{A.1})$$

with $t = \pi M N_{\text{coll}}$, $\xi = \gamma/\beta$, and $\beta = \frac{r_1 r_2 e^{-\frac{i4\pi L}{\lambda}}}{\sqrt{M}}$ the loss of the geometric-optics resonator. Here we follow the heuristic, but general treatment presented in chapter 8 of reference [47] rather than the rigorous treatment by Horwitz [32]. This choice is motivated because the former approach is mathematically simpler and yields the same results as the rigorous approach.

We start by segmenting the integration domain in three sections:

$$\begin{aligned} \int_{-1}^1 e^{-it(x_{\text{in}} - \frac{x_{\text{out}}}{M})^2} U(x_{\text{in}}) dx_{\text{in}} &= \int_{-1}^{-1+\varepsilon} e^{-it(x_{\text{in}} - \frac{x_{\text{out}}}{M})^2} U(x_{\text{in}}) dx_{\text{in}} \\ &+ \int_{-1+\varepsilon}^{1-\varepsilon} e^{-it(x_{\text{in}} - \frac{x_{\text{out}}}{M})^2} U(x_{\text{in}}) dx_{\text{in}} \\ &+ \int_{1-\varepsilon}^1 e^{-it(x_{\text{in}} - \frac{x_{\text{out}}}{M})^2} U(x_{\text{in}}) dx_{\text{in}} \end{aligned} \quad (\text{A.2})$$

where ε is an infinitesimally small positive number. When the magnification M is sufficiently large the first and third integrals give rise to the end-point contributions $\varkappa(\pm 1, x)$, while the second integral yields the stationary-phase contribution $F(x_s)$.

The contribution of the endpoints can be obtained easily. Following Stamnes [47] (section

8.1.3) we integrate by parts, yielding (here we only show the result for the first integral):

$$\begin{aligned}
 \kappa(-1, x_{\text{out}}) &= \int_{-1}^{-1+\varepsilon} e^{-it(x_{\text{in}} - \frac{x_{\text{out}}}{M})^2} U(x_{\text{in}}) dx_{\text{in}} \\
 &\approx \frac{1}{-2it} \frac{U(x_{\text{in}}) e^{-it(x_{\text{in}} - \frac{x_{\text{out}}}{M})^2}}{(x_{\text{in}} - \frac{x_{\text{out}}}{M})} \Big|_{-1}^{-1+\varepsilon} \\
 &\quad + \frac{e^{-it(x_{\text{in}} - \frac{x_{\text{out}}}{M})^2}}{-2it(x_{\text{in}} - \frac{x_{\text{out}}}{M})} \frac{1}{4it(x_{\text{in}} - \frac{x_{\text{out}}}{M})^2} \left[2U(x_{\text{in}}) - 2U'(x_{\text{in}}) \left(x_{\text{in}} - \frac{x_{\text{out}}}{M} \right) \right] \Big|_{-1}^{-1+\varepsilon} \\
 &\quad + \Theta(t^{-3}).
 \end{aligned} \tag{A.3}$$

Next, following the same reference, we assume that the contribution to this integral from the point $-1 + \varepsilon$ cancels the contribution from the same point to the second integral in Eq.(A.2) evaluated at the same point¹. As a result of this assumption the end-point contributions are obtained by replacing $x_{\text{in}} = \pm 1$ in Eq.(A.3).

The stationary point contributions are obtained by applying the techniques of Section (2.5.1), yielding:

$$\begin{aligned}
 F_s(x_{\text{out}}) &= \int_{-1+\varepsilon}^{1-\varepsilon} e^{-it(x_{\text{in}} - \frac{x_{\text{out}}}{M})^2} U(x_{\text{in}}) dx_{\text{in}} \\
 &\approx \sqrt{\frac{\pi}{it}} U(x_{\text{out}}/M) + \frac{1}{4} \sqrt{\frac{\pi}{(it)^3}} U''(x_{\text{out}}/M),
 \end{aligned} \tag{A.4}$$

We see in Eq. (A.4), apart from the purely geometrical propagator (the term $U(x/M)$), the contribution of a term depending of the second derivative of the field.

¹According to Stamnes [47] the appearance of this artificial boundary is a pitfall of the present approach. This problem does not appear in more rigorous theories like that of reference [32].

Grouping all terms, and replacing in Eq. (A.1), we obtain the following asymptotic expansion [32]:

$$\begin{aligned}
 \xi U(x) &\approx \sqrt{\frac{it}{\pi}} [F(x) + \varkappa(-1, x_{\text{out}}) + \varkappa(1, x_{\text{out}})] \\
 &= U(x/M) \\
 &\quad - \frac{1}{2\sqrt{i\pi t}} \left[\frac{e^{-it(1+x/M)^2}}{1+x/M} U(-1) + \frac{e^{-it(1-x/M)^2}}{1-x/M} U(1) \right] \\
 &\quad + \frac{1}{4it} U''(x/M) \\
 &\quad + \frac{1}{4\sqrt{\pi(it)^3}} \frac{e^{-it(1+x/M)^2}}{1+x/M} \left[\frac{U(-1)}{(1+x/M)^2} + \frac{U'(-1)}{1+x/M} \right] \\
 &\quad + \frac{1}{4\sqrt{\pi(it)^3}} \frac{e^{-it(1-x/M)^2}}{1-x/M} \left[\frac{U(1)}{(1-x/M)^2} + \frac{U'(1)}{1-x/M} \right] \\
 &\quad + \Theta(t^{-2})
 \end{aligned} \tag{A.5}$$

It is just as difficult to find the solutions of Eq. (A.5) as is to find the solutions of the complete Huygens-Fresnel integral. In order to discover whether additional simplifications are possible, we can study the transformation that Eq. (A.5) induces on a field profile that is iteratively applied at its input; this is equivalent to launching a field profile inside a resonator and studying its decay.

We start by injecting a plane wave $E_0(x) = 1$, after one round-trip we obtain:

$$\begin{aligned}
 E_1(x) &= \beta \left(1 - \frac{1}{2\sqrt{i\pi t}} \left[E_0(1) \frac{e^{-it(1-x/M)^2}}{1-x/M} + E_0(-1) \frac{e^{-it(1+x/M)^2}}{1+x/M} \right] \right. \\
 &\quad \left. + \frac{1}{4\sqrt{\pi(it)^3}} \left[E_0(1) \frac{e^{-it(1-x/M)^2}}{(1-x/M)^3} + E_0(-1) \frac{e^{-it(1+x/M)^2}}{(1+x/M)^3} \right] \right),
 \end{aligned} \tag{A.6}$$

A quick look at table A.1 shows that the terms of order $t^{-3/2}$ are completely negligible for resonators with a parameter t larger than 50. Therefore, the field E_1 that will be the input for the next iteration is given by:

$$E_1(x) = \beta \left(1 - \frac{1}{2\sqrt{i\pi t}} \left[E_0(1) \frac{e^{-it(1-x/M)^2}}{1-x/M} + E_0(-1) \frac{e^{-it(1+x/M)^2}}{1+x/M} \right] \right). \tag{A.7}$$

This is nothing more than a plane-wave that interferes with an edge-wave radiating from the point $x = \pm 1$.

| t | $c_1 = \frac{1}{2\sqrt{i\pi t}}$ | $c_2 = \frac{1}{4t}$ | c_1/c_2 | $c_3 = \frac{1}{4\pi^{1/2}(t)^{3/2}}$ |
|-------|----------------------------------|----------------------|-----------|---------------------------------------|
| 10 | 0.09 | 0.025 | 3.5 | 0.004 |
| 50 | 0.04 | 0.005 | 7.9 | 4×10^{-4} |
| 100 | 0.03 | 2.5×10^{-3} | 11.3 | 1.4×10^{-4} |
| 500 | 0.01 | 5×10^{-4} | 25.23 | 1×10^{-5} |
| 1000 | 0.009 | 2.5×10^{-4} | 35.68 | 4×10^{-6} |
| 10000 | 0.003 | 2.5×10^{-5} | 112.8 | 1×10^{-7} |

Table A.1: Values of the coefficients in Eq. (A.5) for resonators of different sizes, as parametrized by t .

We eliminate the factor β since it only affects the normalization of the function E_1 . When we circulate this field once again through the cavity we obtain:

$$\begin{aligned}
 E_2(x) \propto & 1 - \frac{1}{2\sqrt{i\pi t}} \left[E_0(1) \frac{e^{-it(1-x/M^2)^2}}{1-x/M^2} + E_0(-1) \frac{e^{-it(1+x/M^2)^2}}{1+x/M^2} \right] \\
 & - \frac{1}{2\sqrt{i\pi t}} \left[E_1(1) \frac{e^{-it(1-x/M)^2}}{1-x/M} + E_1(-1) \frac{e^{-it(1+x/M)^2}}{1+x/M} \right] \\
 & + \frac{1}{4it} E_1''(x/M).
 \end{aligned} \tag{A.8}$$

The appearance of the last term represents a serious problem since it gives rise to a term proportional to t^2 . The power of this term is higher than the combined powers of the terms in the denominator ($t^{3/2}$) implying that it will be the dominant term in the series approximation. Unfortunately, the author does not know of rigorous treatment that justifies the elimination of this term. Nevertheless, we have good reasons to believe that it can be excluded from the series approximation, at least in the regime where our interest lies (large values of t):

- We know that in the limit $\lambda \rightarrow 0$ (i.e. $t \rightarrow \infty$) this term must be zero. This is so since it corresponds to the regime where geometric optics provides a perfect description of the properties of light, and the propagator predicted by that theory has the form (Eq. 2.44):

$$U(x) = \beta U(x/M),$$

where this term has completely disappeared.

- We know that when the resonator has finite size but is nevertheless big, i.e., t is finite but large, physical optics must provide only a small correction to the eigenvalue predicted by geometric optics. This correction must become smaller as the resonator's size becomes bigger. The term at hand clearly contradicts this behavior.
- A theory that excludes this term provides excellent predictions for the excess-noise behavior of unstable-resonator lasers, even for resonators with a small value of t . See reference [4].

In view of the previous discussion, we conclude the eigenmodes of unstable resonators satisfy the equations:

$$\xi U(x) = U(x/M) - \frac{U(1)}{2\sqrt{i\pi t}} \left[\frac{e^{-it(1+x/M)^2}}{1+x/M} + \frac{e^{-it(1-x/M)^2}}{1-x/M} \right], \quad (\text{A.9})$$

for the even modes, and:

$$\xi U(x) = U(x/M) - \frac{U(1)}{2\sqrt{i\pi t}} \left[\frac{e^{-it(1+x/M)^2}}{1+x/M} - \frac{e^{-it(1-x/M)^2}}{1-x/M} \right], \quad (\text{A.10})$$

for the odd ones.

Appendix B

Approximating the eigenvalue of the fundamental mode of a wave-optics unstable-resonator.

In Section 2.6.2 we studied the structure of the modes of unstable resonators, according to the solutions provided by the Virtual Source Theory. We derived a relation (Eq.(2.69)) between the eigenvalue of a given mode, and its box-dimension. Here we are interested to find an estimate of the eigenvalue of the fundamental mode of an unstable-resonator. Such an eigenvalue is a solution of the equation (2.64):

$$\xi^{N+1} - [1 + D_1] \xi^N + \sum_{m=0}^{N-1} [D_{N-m} - D_{N-m+1}] \xi^m = 0. \quad (\text{B.1})$$

with $D_n = D_n(1)$ given by:

$$D_n = \frac{1}{2\sqrt{i\pi t}} \left[\frac{e^{-it(1-1/M^n)^2}}{1 - 1/M^n} + \frac{e^{-it(1+1/M^n)^2}}{1 + 1/M^n} \right] \quad (\text{B.2})$$

The method of Newton-Raphson [89] is the departing point of our calculation. Such a method prescribes that the roots of a function can be calculated iteratively by means of the recursion relation:

$$\xi^{(i+1)} = \xi^{(i)} - \frac{H(\xi^{(i)})}{H'(\xi^{(i)})} \quad (\text{B.3})$$

where $\xi^{(i)}$ represents the value of the root after the i -th iteration, H is the function whose roots we are trying to find (Eq.(B.1)), and H' its derivative. This iterative method provides a rapidly converging algorithm to find the roots of a function. However, both the speed of this convergence and the specific root to which it converges, depend of an intelligent choice of the input $\xi^{(0)}$.

For the particular case of the fundamental mode of an unstable resonator, the eigenvalue provided by the geometric optics approximation ($\xi = 1$) represents the natural choice of $\xi_0^{(0)}$. The reason is that, for relatively large resonators, as those that interests us, we expect that wave-optical correction to the geometric-optics result will be small. Taking:

$$\begin{aligned} H(\xi) &= \xi^{N+1} - (1 + D_1)\xi^N + \sum_{m=0}^{N-1} (D_{N-m} - D_{N-m+1})\xi^m \\ H'(\xi) &= (N+1)\xi^N - N(1 + D_1)\xi^{N-1} + \sum_{m=1}^{N-1} (D_{N-m} - D_{N-m+1})m\xi^{m-1}, \end{aligned} \quad (\text{B.4})$$

and replacing $\xi = 1$, we obtain:

$$\begin{aligned} H(1) &= D_1 + \sum_{m=0}^{N-1} (D_{N-m} - D_{N-m+1}) \\ H'(1) &= 1 - ND_1 + \sum_{m=1}^{N-1} m(D_{N-m} - D_{N-m+1}) \\ &= 1 - \sum_{m=1}^{N-1} D_m. \end{aligned} \quad (\text{B.5})$$

For the first iteration we replace Eq.(B.5) in Eq.(B.3), obtaining:

$$\xi_0^{(1)} = 1 - \frac{D_1 + \sum_{m=0}^{N-1} (D_{N-m} - D_{N-m+1})}{1 - \sum_{m=1}^{N-1} D_m}. \quad (\text{B.6})$$

By taking:

$$X_n = \sqrt{\pi t} D_n = \frac{M^{2n}}{M^{2n} - 1} \left[\cos\left(\frac{2t}{M^n}\right) + \frac{i}{M^n} \sin\left(\frac{2t}{M^n}\right) \right] e^{-it\left(1 - \frac{1}{M^{2n}}\right)}, \quad (\text{B.7})$$

Equation (B.8) transforms in:

$$\xi_0^{(1)} = 1 - \frac{X_1 + \sum_{m=0}^{N-1} (X_{N-m} - X_{N-m+1})}{\sqrt{\pi t} - \sum_{m=1}^{N-1} X_m}. \quad (\text{B.8})$$

This is the expression we are looking for. Since both the term in the numerator and the sum in the denominator corresponds to a sum of N terms of order 1, and N is basically given by $\log_M t \ll \sqrt{t}$, we can conclude that the order of magnitude of the correction is basically given by the square root term. A look at table A.1 shows that after this first iteration we are talking of a correction of around 3%, for resonators with $t \approx 100$. This is rather small, and therefore we can stop iterating.

We can still provide bounds to the eigenvalue as a function of the parameter t . This is done simply by recalling our discussion above to find that:

$$-N < X_1 + \sum_{m=0}^{N-1} (X_{N-m} - X_{N-m+1}) < N \quad (\text{B.9})$$

where we assume that each term in the sum contributes with a random component of order one. Similarly:

$$1 - N < \sum_{m=1}^{N-1} X_m < N - 1, \quad (\text{B.10})$$

and therefore, taking $N \approx \log_M(250t)$, we obtain:

$$1 - \frac{\log_M(250t)}{\sqrt{\pi t} - \log_M(250t)} < \xi_0^{(1)} < 1 + \frac{\log_M(250t)}{\sqrt{\pi t} - \log_M(250t)} \quad (\text{B.11})$$

B Approximating the eigenvalue of the fundamental mode of a wave-optics unstable-resonator.

Appendix C

Algorithm to determine the relative intensity of a sequence of images

As was mentioned during the discussion in section 3.7.2, the study of the afterglow of a given light source by means of an ICCD camera requires techniques to separate, in each image, illuminated pixels from non-illuminated ones. This is normally done by comparing the gray-level of each pixel against a threshold value T : those pixels with a signal level bigger than T are classified as illuminated, and the rest are classified as not illuminated¹. The central problem is how to determine a good value of T for each bitmap of the decay sequence.

We start by observing that there is not a unique way to define such a threshold. In some situations this quantity can be seen as the point of optimal separation of the two populations, or in other words: the point where the accumulated probability of classifying a pixel that belong to one population as belonging to the other population, is minimized. This definition requires the experimenter to introduce specific assumptions over the shape and functional dependency of the probability distributions of the populations under analysis, therefore it can not be applied to analyze the typical data-sets obtained during our experiments, since this distributions are completely unknown, and change as the settings of the optical instruments along the beam path do. The alternative definition of the threshold consist of seeing it as a number that arises from the consistent application of a selection rule, to the populations under analysis. In this way the selection rule somehow expresses something about our knowledge or assumptions about the physical processes underlying the structure of the images under analysis. The key to success when this path is followed consist of finding a rule that somehow fits the phenomenology.

¹This operation is called image segmentation.

As an example let's take a look to fig. C.1. If each one of the populations that we intend to separate has a clearly defined and distinct central tendency, or in other words: if the histogram of the bitmap under analysis presents some resemblance to the "generic" histogram shown in fig. C.1, then the problem of setting a proper threshold can be readily solved by applying the following algorithm, introduced in section 10.3.3 of reference [90]:

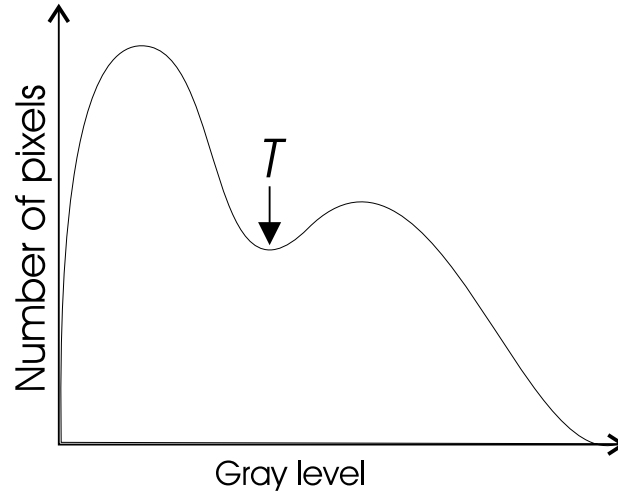


Figure C.1: Histogram of pixels counts for the highest signal-to-noise image shown in

1. Select an initial estimate of T .
2. Segment the image using T . After this operation the image is divided in two groups of pixels, the set **A** of pixels with values bigger than T , and the set **B** of pixels with values smaller than T .
3. The average number of pixels counts \bar{A} and \bar{B} of the pixel populations **A** and **B** is calculated.
4. Compute a new threshold value

$$T = \frac{1}{2} (\bar{A} + \bar{B})$$

5. Repeat steps 2 to 4 until the difference in T between consecutive iterations is smaller than a predefined parameter T_0

In other words, this algorithm uses an initial value of the threshold value to partition the image, then it defines a new average as the mean of average values of the two resulting

populations, and repeats the segmentation procedure until the position of the threshold does not change significantly between iterations.

This algorithm does not make any specific assumption about the specific form of the distributions of both populations, it simply uses the fact that an average always can be found. It is clear that the underlying strategy only works fine in those cases where the average is a good measure of the central tendency of the populations, just as in the histogram shown in fig. C.2.

But: do the typical distributions obtained during our experiment look like Fig. C.1?. Fig. C.2 shows the histograms of two frames obtained during a different moments of a decay sequence. The left side corresponds to a frame with a low signal-to-noise, while the right side is taken from a frame with a very high one. In both cases the tail, corresponding to the population of illuminated pixels, does not have the form of a peak, and therefore it does not make sense to try to characterize it using one of the typical statistical measures of central tendency.

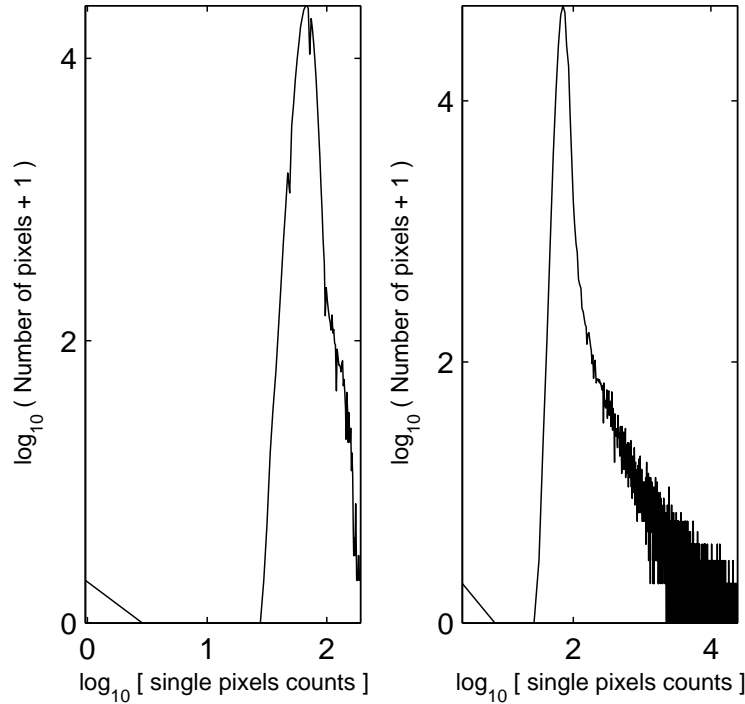


Figure C.2: Histogram of pixels counts for a low signal and a high signal frames of a decay sequence. vertical scale is linear; right plot: vertical scale is logarithmic. Left plot: Low signal. Right Frame: high signal.

We also can observe in fig. C.2 that mean peak, intuitively associated with the background pixels, hardly changes from position and size, as compared with the changes experimented by the tail. This suggests that the behavior of the background population, is hardly affected

by the presence of light, as indeed it must. In our approach, we use this observation in order to define a threshold solely in terms of the background population. The crucial idea is that by finding a set of statistical measures that precisely describe the boundaries of such a set of pixels in a broad variety of "dark" situations, we can use then these statistical measures to define what we mean by background population on "illuminated" frames.

The discussion on section 3.7.2 describes the basis of our analysis. There we studied several sequences of dark shots trying to find a reliable measure of the position of the center peak, and the width of the distribution of pixel values. We found that a characterization of the center peak of background population of each frame k , by means of the median $Z(k)$, was highly stable with regard to changes on the limits of such a population. In addition, we found that for a typical sequence of dark shots, the absolute mean dispersion $D_{abs}(k)$ provided a more reliable estimate of the width of curve than other statistical measures, such as the standard deviation. This meaning that the histogram of the difference between the maximum of each frame, and its median, measured in units of the $D_{abs}(k)$ of that frame, normally was narrower than the corresponding histogram measured in units of another statistical dispersion.

Based on this information we proceed to define our background threshold as all the image pixels whose signal is smaller than the median of the background population plus eight times the absolute mean dispersion of such a population. The values of this quantities are determined by starting from a "well chosen" threshold value that is used to segments the image, and the new threshold is calculated from the resulting populations. This self-consistent loop is repeated until the difference between two consecutive threshold value is smaller than certain prescribed value.

Our algorithm has then the following form:

1. Define an initial threshold T .
2. Segment the image using T . After this operation the image is divided in two groups of pixels, the set **A** of pixels with values bigger than T , and the set **B** of pixels with values smaller than T .
3. Compute the median M_{ed} and absolute mean dispersion D_{abs} of the population of non-illuminated pixels **B**.
4. Define a new threshold value as:

$$T = M_{ed} + 8D_{abs}$$

5. Repeat operation 2 to 4 until the threshold does not change significantly between consecutive iterations.

This is the algorithm that we have used in Section 3.7.2.

Bibliography

- [1] A. L. Schawlow and C. H. Townes, ‘Infrared and optical masers’, *Phys. Rev.* **112**, 1940 (1958).
- [2] K. Petterman, ‘Coupled-mode theory of unstable resonators’, *IEEE J. Quantum Electron.* **QE-15**, 566 (1979).
- [3] Y. J. Cheng, C. G. Fanning, and A. E. Siegman, ‘Experimental observation of a large excess quantum noise factor in the linewidth of a laser oscillator having nonorthogonal modes’, *Phys. Rev. Lett.* **77**, 627 (1996).
- [4] M. A. van Eijkelenborg, A. M. Lidberg, M. S. Thijssen, and J. P. Woerdman, ‘Resonance of quantum noise in an unstable cavity laser’, *Phys. Rev. Lett.* **77**, 4314 (1996).
- [5] A. E. Siegman, *Lasers* (Oxford University Press, Oxford, 1986).
- [6] H. A. Haus, *Waves and fields in optoelectronics* (Prentice Hall, Englewood Cliffs, 1984).
- [7] ‘Paraxia’, Sciopt Enterprises, 7189 Wooded Lake Dr., San Jose, CA 95120
- [8] G. P. Karman and J. P. Woerdman, ‘Fractal structure of eigenmodes of unstable-cavity lasers’, *Opt. Lett.* **23**, 1909 (1998).
- [9] B. Mandelbrot, *The fractal geometry of nature* (W. H. Freeman, San Francisco, 1982).
- [10] K. Falconer, *Fractal geometry : mathematical foundations and applications*, 2nd. Ed. (Wiley, Chichester, 2003).
- [11] D. Sornette, *Critical phenomena in natural sciences : chaos, fractals, self-organization and disorder: concepts and tools* (Springer, Berlin, 2000).
- [12] J. Feder, *Fractals* (Plenum Press, New York, 1988).
- [13] H. M. Hastin and G. Sugihara, *Fractals, a user’s guide for the natural sciences* (Oxford University Press, Oxford, 1993).
- [14] H. Lauwerier, *Fractals, images of chaos* (Penguin Books, 1991).
- [15] M. Barnsley, *Fractals everywhere* (Academic Press, Boston, 1988), first edition.
- [16] M. J. Turner, J. M. Blackledge, and P. R. Andrews, *Fractal geometry in digital imaging* (Academic Press, London, 1998).
- [17] J. L. Locher, C. H. A. Broos, M. C. Escher, G. W. Locher, and H. S. M. Coxeter, *De werelden van M. C. Escher* (Meulenhoff, 1971).
- [18] G. I. Barenblatt, *Scaling, self-similarity, and intermediate asymptotics* (Cambridge University Press, Cambridge, UK, 1996).
- [19] H. H. Hardy and R. A. Beier, *Fractals in reservoir engineering* (World Scientific, 1994).
- [20] M. V. Berry and Z. V. Lewis, ‘On the Weierstrass-Mandelbrot fractal function’, *Proc. Roy. Soc.* **A370**, 459 (1980).

Bibliography

- [21] M. A. Zaks, 'Influence of noise on dynamics with fractal fourier spectra', *Physica A* **310**, 285 (2002).
- [22] F. Pallikari, 'A study of the fractal character in electronic noise processes', *Chaos, Solitons and Fractals* **12**, 1499 (2001).
- [23] J. C. Russ, *Fractal surfaces* (Plenum Press, New York, 1994).
- [24] J. C. Russ, *The image processing handbook* (CRC Press, Boca Raton, FL, 2002), fourth edition.
- [25] G. P. Karman, G. S. McDonald, G. H. C. New, and J. P. Woerdman, 'Laser optics: fractal modes in unstable resonators', *Nature* **402**, 138 (1999).
- [26] W. H. Southwell, 'Virtual-source theory of unstable resonator modes', *Opt. Lett.* **6**, 487 (1981).
- [27] W. H. Southwell, 'Unstable-resonator-mode derivation using virtual-source theory', *J. Opt. Soc. Am. A* **3**, 1885 (1986).
- [28] G. S. McDonald, G. P. Karman, G. H. C. New, and J. P. Woerdman, 'Kaleidoscope laser', *J. Opt. Soc. Am. B* **17**, 524 (2000).
- [29] M. V. Berry, C. Storm, and W. van Saarloos, 'Theory of unstable laser modes: edge waves and fractality', *Opt. Commun.* **197**, 393 (2001).
- [30] M. V. Berry, 'Fractal modes of unstable lasers with polygonal and circular mirrors', *Opt. Commun.* **200**, 321 (2001).
- [31] M. A. Yates and G. H. C. New, 'Fractal dimension of unstable resonator modes', *Opt. Commun.* **208**, 377 (2002).
- [32] P. Horwitz, 'Asymptotic theory of unstable resonator modes', *J. Opt. Soc. Am.* **63**, 1528 (1973).
- [33] A. E. Siegman, 'Unstable optical resonators for laser applications', *Proc. IEEE* **53**, 277 (1965).
- [34] H. Goldstein, *Classical mechanics* (Addison-Wesley, Reading, MA, 1980), second edition.
- [35] R. B. Guenther and J. W. Lee, *Partial differential equations of mathematical physics and integral equations* (Dover, Mineola, NY, 1996).
- [36] E. L. O'Neill, *Introduction to statistical optics* (Dover, Mineola, NY, 1992).
- [37] D. Bohm, *Quantum theory* (Dover, Mineola, NY, 1989).
- [38] A. E. Siegman, 'Orthogonality properties of optical resonator eigenmodes', *Opt. Commun.* **31**, 369 (1979).
- [39] A. Kostenbauder, Y. Sun, and A. E. Siegman, 'Eigenmode expansions using biorthogonal functions: complex-valued Hermite-Gaussians', *J. Opt. Soc. Am. A* **14**, 1780 (1997).
- [40] J. J. Sakurai, *Quantum mechanics* (Addison-Wesley, Oxford, 1986).
- [41] R. K. Luneburg, *Mathematical theory of optics* (University of California Press, Berkeley and Los Angeles, 1964).
- [42] M. Born and E. Wolf, *Principles of optics* (Cambridge University Press, Cambridge, 1999), seventh edition.
- [43] W. F. Krupke and W. R. Sooy, 'Properties of an unstable confocal resonator CO₂ laser system', *IEEE J. Quantum Electron.* **QE-5**, 575 (1969).
- [44] W. K. Kahn, 'Unstable optical resonator', *Appl. Opt.* **5**, 407 (1966).

- [45] E. Olivier, D. Chauvat, A. L. Floch, and F. Bretenaker, 'Temporal behavior of an unstable optical cavity', *Opt. Lett.* **24**, 22 (1999).
- [46] A. E. Siegman, 'Excess spontaneous emission in non-hermitean optical systems. i. laser amplifiers', *Phys. Rev. A* **39**, 1253 (1989).
- [47] J. J. Stamnes, *Waves in focal regions: propagation, diffraction and focusing of light, sound and water waves* (Hilger, Bristol, 1986).
- [48] W. H. Southwell, 'Validity of the Fresnel approximation in the near field', *J. Opt. Soc. Am.* **71**, 7 (1981).
- [49] J. W. Goodman, *Introduction to Fourier optics* (McGraw Hill, Boston, 1988), second edition.
- [50] A. G. Fox and T. Li, 'Resonant modes in a maser interferometer', *Bell. Sys. Tech. J.* **40**, 453 (1961).
- [51] A. E. Siegman and R. Arrathoon, 'Modes in unstable optical resonators and lens waveguides', *IEEE J. Quantum Electron.* **QE-3**, 156 (1967).
- [52] I. S. Gradshteyn and I. M. Ryzhik, *Table of integrals, series and products* (Academic Press, New York, 1965), fourth edition.
- [53] M. Lax, G. P. Agrawal, and W. H. Louisell, 'Continuous Fourier-transform spline solutions of unstable resonator-field distribution', *Opt. Lett.* **4**, 303 (1979).
- [54] M. E. Rogers and J. H. Erkkila, 'Resonator mode analysis using linear prolate functions', *Appl. Opt.* **22**, 1992 (1983).
- [55] L. Chen and L. B. Felsen, 'Coupled-mode theory of unstable resonators', *IEEE J. Quantum Electron.* **QE-9**, 1102 (1973).
- [56] L. A. Weinstein, *Open resonators and open waveguides* (Golem Press, 1969).
- [57] P. Horwitz, 'Modes in misaligned unstable resonators', *Appl. Opt.* **15**, 167 (1976).
- [58] W. H. Southwell, 'Asymptotic solution of the Huygens-Fresnel integral in circular coordinates', *Opt. Lett.* **3**, 100 (1978).
- [59] R. R. Butts and P. V. Avizonis, 'Asymptotic analysis of unstable laser resonators with circular mirrors', *J. Opt. Soc. Am.* **68**, 1072 (1978).
- [60] Y. Q. Li and C. C. Sung, 'Extended asymptotic theory of unstable resonator modes', *Appl. Opt.* **29**, 4462 (1990).
- [61] L. Mandel and E. Wolf, *Optical coherence and quantum optics* (Cambridge University Press, Cambridge, 1986).
- [62] W. Schleich, *Quantum optics in phase space* (Springer, Berlin, 1999).
- [63] Y. A. Anan'ev and V. E. Sherstobitov, 'Influence of the edge effects on the properties of unstable resonators', *Sov. J. Quantum Electron.* **1**, 263 (1971).
- [64] M. V. Berry, 'Mode degeneracies and the petermann excess-noise factor for unstable lasers', *J. Mod. Opt.* **50**, 63 (2003).
- [65] J. Courtial, 'Fractal multiple reduction imaging lasers', *Opt. Commun.* **174**, 235 (2000).
- [66] J. Courtial, 'Fractal generation using optical feedback with incoherent gain', *Opt. Commun.* **190**, 123 (2001).
- [67] J. Courtial and M. Padgett, 'Monitor-outside-a-monitor effect and self-similar fractal structure in the eigenmodes of unstable optical resonators', *Phys. Rev. Lett.* **85**, 5320 (2000).
- [68] J. Courtial, 'Classic-fractal eigenmodes of unstable canonical resonators', *Opt. Commun.* **223**, 17 (2003).

Bibliography

- [69] J. Courtial, J. Leach, and M. Padgett, 'Image processing: fractals in pixelated video feedback', *Nature* **414**, 864 (2001).
- [70] G. T. Moore and R. J. McCarthy, 'Theory of modes in a loaded strip confocal unstable resonator', *J. Opt. Soc. Am.* **67**, 228 (1977).
- [71] J. J. Scherer, J. B. Paul, A. O'Keefe, and R. J. Saykally, 'Cavity ringdown laser absorption spectroscopy: history, development, and application to pulsed laser molecular beams', *Chem. Rev.* **97**, 25 (1997).
- [72] J. W. Hahn, Y. S. Yoo, J. Y. Lee, J. W. Kim, and H. Le, 'Cavity ring-down spectroscopy with a continuous-wave laser: calculation of coupling efficiency and a new spectrometer design', *Appl. Opt.* **38**, 1859 (1999).
- [73] D. Romanini, A. A. Kachanov, N. Sadeghi, and F. Stoeckel, 'CW cavity ring down spectroscopy', *Chem. Phys. Lett.* **264**, 316 (1997).
- [74] D. Romanini, A. A. Kachanov, and F. Stoeckel, 'Diode laser cavity ring down spectroscopy', *Chem. Phys. Lett.* **270**, 538 (1997).
- [75] K. I. Zemskov, A. A. Isaev, M. A. Kazaryan, G. G. Petrash, and S. G. Rautian, 'Use of unstable resonators in achieving the diffraction divergence of the radiation emitted from high-gain pulsed gas lasers', *Sov. J. Quantum Electron.* **4**, 474 (1974).
- [76] A. A. Isaev, M. A. Kazaryan, G. G. Petrash, and S. G. Rautian, 'Converging beams in unstable telescopic resonators', *Sov. J. Quantum Electron.* **4**, 761 (1974).
- [77] Y. A. Anan'ev, 'Establishment of oscillations in unstable resonators', *Sov. J. Quantum Electron.* **5**, 615 (1975).
- [78] R. M. S. Knops, *Quantum optics with a cold Helium beam*, Ph.D. thesis, Technical University of Eindhoven (1998).
- [79] F. Druon, F. Balembois, P. Georges, and A. Brun, 'High-repetition-rate 300-ps pulsed ultraviolet source with a passively Q-switched microchip laser and a multipass amplifier', *Opt. Lett.* **24**, 499 (1999).
- [80] K. Petermann, *Laser diode modulation and noise* (Kluwer Academic Publishers, Dordrecht, 1988).
- [81] G. Shtengel, D. Ackerman, and P. Morton, 'True carrier lifetime measurements of semiconductor lasers', *Electron. Lett.* **31**, 1747 (1995).
- [82] N. M. Frober, A. M. Johnson, K. W. Goossen, J. E. Cunningham, M. B. Santos, W. Y. Jan, and T. H. Wood, 'Picosecond carrier escape by resonant tunneling in pseudomorphic InGaAs/GaAsP quantum well modulators', *Appl. Phys. Lett.* **64**, 1705 (1994).
- [83] J. S. Massa, G. S. Buller, and A. C. Walker, 'Time-resolved photoluminescence studies of cross-well transport in biased GaAs/AlGaAs multiple quantum well *p-i-n* structure', *J. Appl. Phys.* **82**, 712 (1997).
- [84] G. W. 'tHooft, 'Private communication', .
- [85] G. H. C. New, M. A. Yates, J. P. Woerdman, and G. S. McDonald, 'Diffractive origin of fractal resonator modes', *Opt. Commun.* **193**, 261 (2001).
- [86] B. Frieden, *Probability, statistical optics, and data testing* (Springer, Berlin, 1983).
- [87] J. W. Goodman, *Statistical optics* (Wiley-Interscience, New York, 1985).
- [88] S. E. Moran, B. L. Ulich, W. P. Elkins, R. L. Stritmatter, and M. J. DeWeert, 'Intensified CCD (ICCD) dynamic range and noise performance', in 'Ultrahigh and High-Speed Photography and Image-Based Motion Measurement', volume 3173 (SPIE, 1997).

- [89] W. H. Press, S. A. Teukolski, W. T. Vetterling, and B. P. Flannery, *Numerical recipes in C* (Cambridge University Press, Cambridge, 1992), second edition.
- [90] R. C. Gonzales and R. E. Woods, *Digital image processing* (Prentice Hall, Upper Saddle River, NJ, 2002), second edition.
- [91] R. Blumell, I. H. Davidson, W. P. Reinhardt, H. Lin, and M. Sharnoff, ‘Quasilinear ridge structures in water surface waves’, *Phys. Rev. A* **45**, 2641 (1992).

Bibliography

Samenvatting

De titel van dit proefschrift is: "Experimental demonstration of the fractal nature of the modes of unstable resonators". Een directe vertaling van deze titel in het Nederlands is niet eenvoudig te geven; je kunt zeggen dat ik geprobeerd hebt om aan te tonen dat de resonantiepatronen van een instabiele resonator een fractaal karakter hebben. Dit klinkt nogal moeilijk, maar dat is slechts schijn. In deze samenvatting zal ik, zonder in technische details te treden, het achterliggende idee van mijn onderzoek toelichten.

Resonatoren en resonanties

Volgens het woordenboek is een resonator iets dat resoneert. Als voorbeelden worden de klankkast van een muziekinstrument (akoestische resonantie) en de metalen trillholte in de magnetron oven (electromagnetische resonantie) gegeven. Je kunt ook denken aan de laser in je DVD speler (licht resonantie) of aan de slinger van een ouderwetse klok (mechanische resonantie). Bewust of onbewust worden resonatoren dus toegepast in tal van gebruiksvorwerpen uit ons dagelijks leven. In dit onderzoek beperken wij ons tot optische resonatoren, resonatoren waarin licht resoneert, zoals in een laser. Onze conclusies gelden echter voor iedere soort resonator die dezelfde geometrie heeft.

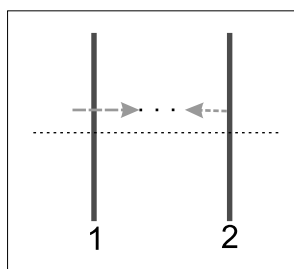


Figure 1: Een zogenaamde vlakke-spiegel resonator: een typische stralengang is weergegeven in de figuur.

Samenvatting

In zijn meest eenvoudige vorm bestaat een optische resonator uit twee vlakke spiegels die recht tegenover elkaar staan, zoals in Fig. 1. Licht dat loodrecht op één van de vlakke spiegels invalt, kaatst via dezelfde weg terug naar de plek waar het vandaan kwam. In het geval dat de twee spiegels tegenover elkaar staan, kaatst het licht heen en weer en is dus gevangen tussen de twee spiegels, zoals is getekend in Fig. 1. Belangrijk hierbij is dat dit alleen lukt bij een

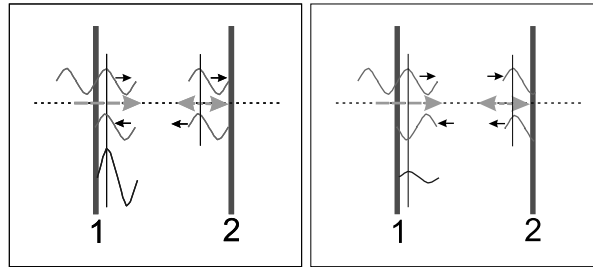


Figure 2: *Condities voor resonantie (linker kant) en antiresonantie (rechter kant) in een vlakke-spiegel resonator. Als er een geheel aantal golflengtes binnen het traject van de straal passen, hebben wij een resonantie te pakken.*

beperkt, maar groot, aantal waarden van de golflengte van de golf. Als aan deze voorwaarde is voldaan is de golf in resonantie met de resonator (Figuur 2).

Resonantie patronen en resonanties

Het tweede concept dat ik wil bespreken is het resonantiepatroon. Dat is de ruimtelijke vorm van een in een resonator resonerende golf. deze vorm verandert niet bij reflectie aan de wanden van de resonator. We zien in figuur 3 de resonantiepatronen van watergolven in twee verschillende resonatoren.

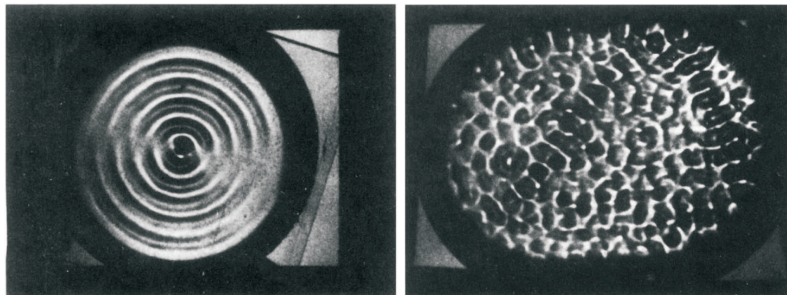


Figure 3: *Mechanische resonantiepatronen. Deze figuren ontstaan als een bak water die bovenop een "overhead projector" staat aan het trillen word gebracht. Links is de bak cilindrisch, rechts heeft de bak de vorm van een stadion. [91]*

Optische resonatoren hebben ook resonantiepatronen. Als we licht, bijvoorbeeld een laserstraal, in een resonator introduceren en het traject van het voor die resonator karak-

teristieke resonantiepatroon laten volgen, zal de laserstraal dit traject blijven volgen zolang het reflectievermogen van de spiegels dit toelaat.

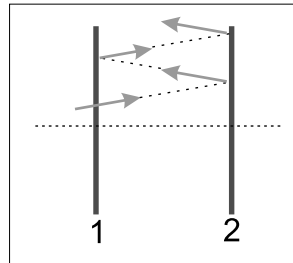


Figure 4: *Vlakke-spiegel resonatoren zijn in de praktijk moeilijk te gebruiken. Ze zijn te gevoelig voor kleine imperfecties.*

De vlakke-spiegel resonator van Fig. 1 is zeer gevoelig voor zelfs maar de geringste imperfectie van de spiegels, of van de hoek waaronder de lichtstraal op de spiegels invalt. Dit is geïllustreerd in Fig.4. Derhalve is deze resonator in de praktijk lastig te gebruiken. Het wordt veel makkelijker als we gebruik maken van gekromde (holle of bolle) spiegels. Dan ontstaan twee varianten: stabiele en instabiele resonatoren.

Stabiele resonatoren

Als we licht laten invallen op een optische resonator die is opgebouwd uit twee holle spiegels die voldoende dicht bij elkaar staan, blijft de lichtstraal gevangen tussen de twee spiegels (Fig.5). Het resonantiepatroon is hier nauwelijks gevoelig voor imperfecties in de spiegels of in de orientatie van de lichtbron. Daardoor is deze geometrie beter bruikbaar als resonator dan die met vlakke spiegels. We spreken nu van "stabiele" resonatoren.

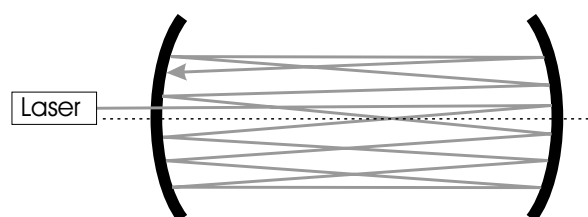


Figure 5: *Een stabiele resonator met daarin getekend het pad dat een in de resonator geïnjecteerde bundel aflegt.*

Hoe zien de resonantiepatronen in dit geval er uit? Voor stabiele resonatoren hebben ze de vorm van een gesloten pad; daardoor volgt de gereflecteerde lichtstraal telkens hetzelfde traject (Fig.6).

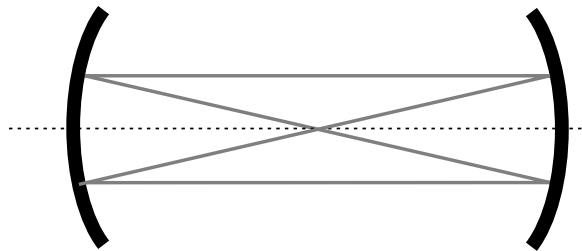


Figure 6: Een stabiele resonator en het pad van een van zijn resonantiepatronen. Dit is een gesloten pad.

Instabiele resonatoren

In het bovenstaande voorbeeld gebruikten we holle spiegels. Wat gebeurt er als wij bolle spiegels gebruiken? Een eenvoudige schets (zie Fig.7) laat zien dat een in de resonator aanwezig lichtstraal altijd, na enige keren kaatsen aan de spiegels, zal ontsnappen. Vanwege die eigenschap heet zo'n resonator instabiel. Instabiele resonatoren kunnen ook gemaakt worden

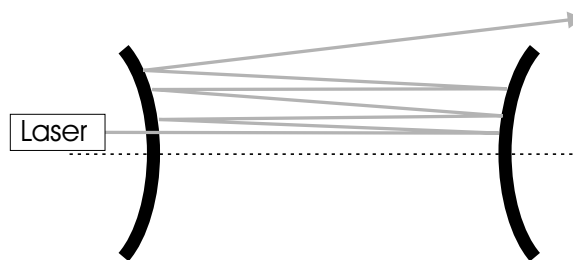


Figure 7: Een instabiele resonator, en een typische uiteenlopende straal traject.

met holle spiegels. In dat geval moeten we de twee spiegels voldoende ver uit elkaar plaatsen, zodat de lichtstralen uit de resonator kunnen ontsnappen.

Binnen een instabiele resonator vormt het traject van de lichtstraal nooit een gesloten circuit. Kan een instabiele resonator wel resoneren? Wel degelijk, maar de resonantiepatronen zijn volstrekt anders dan die van stabiele resonatoren; ze zijn namelijk fractalen.

Om beter te begrijpen wat we bedoelen als we dat zeggen, helpt het om te kijken naar Fig.8. Hier zien we een resonator bestaande uit twee holle spiegels, met verschillende brandpunts afstanden f_1 en f_2 , die een gemeenschappelijk brandpunt hebben. Wij kunnen bovendien ook het pad bekijken die een lichtstraal door de resonator volgt. Een lichtstraal, die zijn pad door de resonator begint op een afstand a van de as van die resonator en dan aan een van de spiegels kaast, komt terug op een afstand $\frac{f_2}{f_1}a$ van de as; de twee rechthoekige driehoeken in figuur 8 helpen dit duidelijk te maken en tonen a en $\frac{f_2}{f_1}a = Ma$; hier is M de vergrotingsfactor van die resonator. Na twee rondgangen door de resonator komt de lichtstraal terug op een afstand M^2a van de as; na drie rondgangen is de afstand tot de as M^3a . Dit proces gaat net zolang door tot de lichtstraal uiteindelijk ontsnapt.

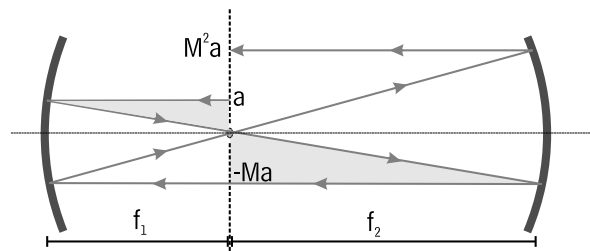


Figure 8: Het straal traject van de resonantiepatroon van een confocaal instabiele resonator.

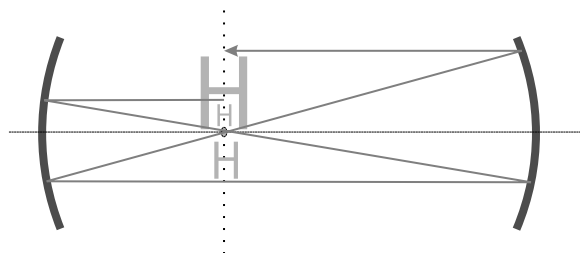


Figure 9: Wanneer we een willekeurig lichtpatroon in de resonator introduceren, en we kijken binnen de resonator, zien we een beeld dat opgebouwd is uit vergrote kopiën van het originele patroon.

De vergrotingsfactor M is het belangrijkste getal waarmee we een instabiele resonator karakteriseren; het is ook de sleutel tot het begrijpen van de aard van de resonantiepatronen. Figuur 9 laat zien wat er gebeurt als we een willekeurig patroon introduceren in een instabiele resonator, bijv. met behulp van een dia. Het beeld dat we zien bestaat uit meerdere kopieën van het origineel, maar elke kopie is een vergrote versie van de vorige kopie. Dus, als dit patroon een resonantiepatroon is, zien we steeds hetzelfde patroon wanneer we op het patroon inzoomen. Een bekend voorbeeld hiervan is het z.g. Droste effect, van de ouderwetse Droste cacao blikken. Patronen die deze eigenschap hebben zijn in de wiskunde uitgebreid bestudeerd en staan bekend als fractalen.

Fractalen

Vanuit morfologisch oogpunt is een fractaal een mathematisch object dat is samengesteld uit verkleinde (of vergrootte) kopieën van zichzelf. Figuur 8 laat een typisch voorbeeld hiervan zien, het Sierpinski tapijt.

In dit geval bestaat het fractale object (figuur 10 links) uit een kernmotief (zoals te zien aan de rechter kant van figuur 10) dat op verschillende schalen herhaald wordt. Er is een eenvoudige relatie die de verschillende schalen met elkaar verbindt. Zo zijn er vierkanten met ribbe a , vierkanten met ribbe $a/3$ en vierkanten met ribbe $a/9$. In de definitie van math-

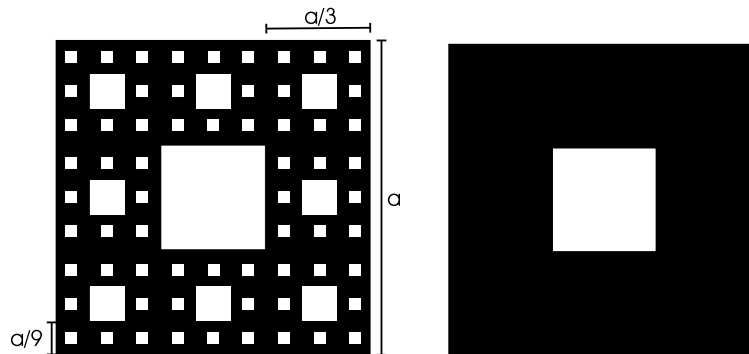


Figure 10: Het Serpienski tapijt (links), en zijn kernmotief (rechts).

ematische fractalen spelen zulke relaties vaak een belangrijke rol.

Dit is echter niet het geval bij fractalen die in de natuur voorkomen. Een typisch voorbeeld hiervan is een kustlijn; als je de lengte van de kustlijn van b.v. Chili probeert te meten blijkt die lengte af te hangen van je meetstok. Hoe kleiner de meetstok hoe langer de kustlijn. Zo een resultaat, dat de uitkomst van een "meting" afhankelijk is van de lengte van de meetstok, dus afhankelijk van de schaal (1:1000, 1:10000, 1:1000000, $1:10^6$,...) is typerend voor een fractaal object.

De onderlinge relatie tussen de lengte van de kustlijn van een fractaal en de lengte van de meetstok legt de zogenaamd fractale dimensie D vast. Fractalen met een hoge waarde van zijn fractale dimensie zijn "wilder" dan fractalen met een lage waarde. Een andere voorbeeld: neem een vel A4 papier. Dat heeft een oppervlakt van $29.7 \times 21 \text{ cm}^2$. De schaduw van dat vel er vlak onder, bij belichting door de zon, meet ook $29.7 \times 21 \text{ cm}^2$. Als wij het vel kreukelen, op een manier dat er geen stukken papier over elkaar heen vouwen, dan wordt het oppervlak van de schaduw kleiner dan het oppervlak van het vel. Hoe fijner de schaal van het kreukelen, des te kleiner wordt de schaduw. Het vel papier is een fractal object geworden.

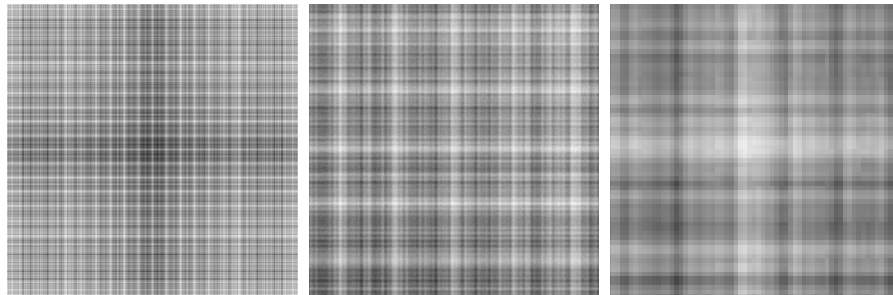


Figure 11: Het (gerekend) resonantiepatroon van een instabiele resonator. Van links na rechts, zoom $1\times$, $4\times$, en $16\times$

Terug naar de instabiele resonator. Figuur 11 laat de resultaten van een berekening zien van het resonantiepatroon van een instabiele resonator met vierkante spiegels. Op verschil-

lende schalen komt het kernmotief steeds weer terug. Er is ook veel meer structuur dan in het Sierpinski tapijt; we verwachten dus een hogere fractale dimensie. De theoretisch voorspelde waarde is 3; en meer zou het nooit kunnen worden. De bevestiging van deze voorspelling vormt onze experimentele uitdaging.

Het experiment

Ons experiment is gebaseerd op de "Cavity ring-down" techniek. Dit klinkt heel wetenschappelijk maar is iets heel gewoons. Dit is de optische variant van een akoustisch effect dat we dagelijks zouden kunnen beleven. Als we tegen een wijnglas tikken horen we aanvankelijk een tik die overgaat in een zuivere toon. Dit komt door onze tik, die slaat n.l. veel resonanties van het glas tegelijk aan. Echter de verschillende resonanties dempen niet allemaal even snel en er is er één die het langzaamst dempt. Na enige tijd hoor je die dus in zijn eentje langzaam uitsterven.

Het optisch equivalent van dit effect staat geschetst in Figuur 12. Het wijnglas is vervangen door een optische resonator, de tik door een lichtpuls, en ons oor door een lichtdetector.

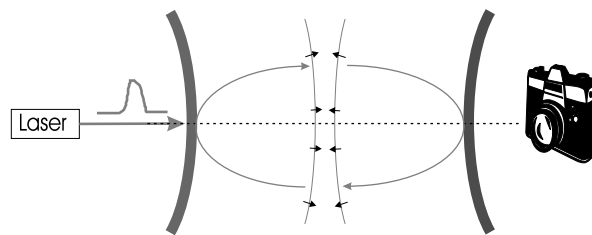


Figure 12: Een cavity ring-down experiment. Een puls van licht uit een laser wordt geïnjecteerd binnen de instabiele resonator. We gebruiken een ultrasnel, hypergevoelige camera om te kijken naar de evolutie van deze licht pulse.

In mijn experiment gaat het niet zozeer om het dempen van de lichtsterkte, maar in het te voorschijn brengen van het resonantiepatroon van de langstlevende resonantie; om dat patroon vast te leggen gebruiken wij een camera. Dit klinkt vrij eenvoudig maar is het niet. Dat komt doordat alles vliegensvlug moet gebeuren. Licht loopt n.l. razendsnel en het experiment is in een paar nanoseconden voorbij. De camera moet dan ook "foto's" kunnen nemen met een sluitertijd van enkele nanoseconden, d.w.z., ongeveer een miljoen keer korter dan bij een traditionele camera.

Dit alles heeft ook alleen maar zin als de lichtpuls ook op zo een korte tijdschaal uitgeschakeld wordt. Dat krijg je ook niet kado. Het is ons toch gelukt zoals te zien in figuur 13.

Samenvatting

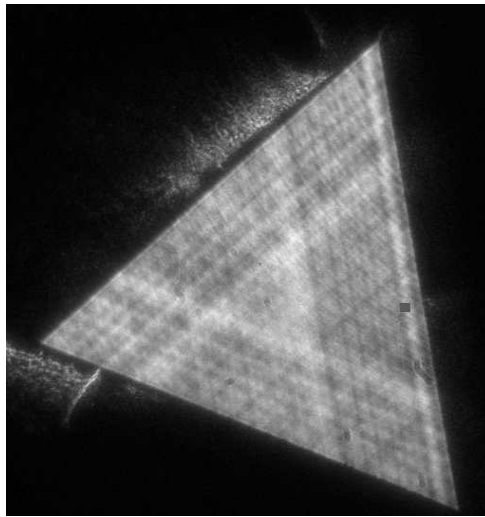


Figure 13: *Het resonantiepatroon (experimenteel) van een instabiele resonator.*

Curriculum vitæ

Javier Augusto Loaiza Rivas

I was born the 15th of October of 1973 in Zarzal, Valle, Colombia, and completed my secondary school at the Gimnasio Norte del Valle, in 1990. After some hesitation I choose to study physics at the Universidad Nacional de Colombia, in Bogota. During this time I became involved in many activities, such as being member of the faculty council, collaborating in the organization of activities for the promotion of science, the faculty's microfootball tournament, and a national meeting of students of physics. I also ran my own internet services company. Finally, I graduated in 1998 after completing my graduation work at the Nuclear Physics Group, in the field of gamma-ray spectroscopy.

Subsequently I assumed a full-time job as IT contractor at ICFES (the Colombian Institute for the Promotion of Higher Education), where I had been a part-time worker since 1995. During this time I also collaborated on a research project that resulted in the construction of the first supercomputer Linux cluster at the National Observatory, and on the edition of the electronic version of *Momento*, the journal of the Department of Physics of my home university.

In 1999 I took part in a school over synchrotron radiation physics at the ICTP in Trieste, Italy. I then moved to Enschede, the Netherlands, to pursue a master's degree in Engineering Physics. I did my graduation work at the LDG devices group; this work consisted of the modeling of the optical coupling between cylindrical microresonators and straight waveguides.

In 2000 I joined the Quantum Optics Group at the University of Leiden. The theory and results of my PhD project are the subject of this thesis.

Curriculum vitae

Nawoord

This thesis would not be complete without giving thanks to everyone who helped me during my five years in Leiden.

Primero que todo debo agradecer a mi familia, tanto materna como paterna. No solamente ustedes me trajeron al mundo, dandome un universo al cual siempre perteneceré, sino que, y esto es mucho más importante, ustedes me han amado sin consideración ni duda algunas, no importa cuan loco, extraño, distante, perdido, desconsiderado, egoista, ebrio, brutal, o enamorado yo haya sido o estado. Puedo a veces parecer distante y no atento, pero creanme: en mi corazon no lo soy. Los amo mucho a todos.

This work couldn't have been completed without the dedication and professionalism of the instrumentmakers and of the experts in electronics and computers. Here I would especially like to mention Koos Benning, Ewie de Kuiper for all the metal work, Rene Overgaww for all the wonderful electronic gadgets, and Arno van Amersfort for running our computer network. Our very diligent secretaries, Anneke Aschoff, Henriette Van Leeuwen, and Danielle van Raaij made sure that the rest of us could concentrate on our research. Desafortunadamente Anneke murió durante el ultimo año de mi doctorado. Que Dios la tenga en su diestra.

The multiple discussions with the other member of the group, Andrea, Dirk, Cyriaque, Sergio, Marnix, Steven, Jos, Yngve, Sumant, Hayk, Erwin, Thijs, Peter, Nikolay, Graciana and Eduard helped me to better understand many of the constructions that are the at the foundations of modern optics; I also frequently laughed in their company. I am especially grateful to my office mate, Jorrit, for 5 years of cohabitation in our small office. Through many conversations about physics, society, women, and life I came to love your splendid self.

I am in deep debt with the many friends who have entertained me outside of the laboratory. Your names are too many to be included here, but you know who you are. Thank you!. Denis, Djamel, Ana, and Lenny: I have great memories of our year together. To my dearest Aurelien, Gulhan, Janneke, Edgar, Juan Diego, Debora, David, Martha and Clara: You are the best!. No puedo finalizar este documento sin antes pensar, desde lo más profundo, en Cécile. Animo!, termina esa tesis cuanto antes.

Finally, I would like to praise the wisdom of the sagacious reader. He knows who he is.